Computational Electrohydrodynamics for Fabricating Polymer Microstructures

Catherine Elizabeth Henzell Tonry

Centre for Numerical Modelling and Process Analysis

Department of Mathematical Sciences

University of Greenwich

A thesis submitted in partial fulfilment of the

requirements of the University of Greenwich

for the Degree of Doctor of Philosophy

November 2015

DECLARATION

I certify that this work has not been accepted in substance for any degree, and is not concurrently being submitted for any degree other than that of Doctor of Philosophy being studied at the University of Greenwich. I also declare that this work is the result of my own investigations except where otherwise identified by references and that I have not plagiarised the work of others.

.....

Catherine Tonry (Ph.D. Student)

Date:

.....

Professor Mayur Patel (Supervisor)

Date:

.....

Professor Christopher Bailey (Supervisor)

Date:

ACKNOWLEDGEMENTS

I would first like to thank my supervisors, Prof. Mayur Patel and Prof. Christopher Bailey for their support during the three years of my Ph.D. study.

In addition I would like to thank the EPSRC and the University of Greenwich who funded the work presented within.

I would also like to thank Prof.Marc Desmuliez from Herriot Watt University and Prof. Weixing Yu from the Chinese Key State Laboratory of Applied Optics for their assistance in understanding the experimental techniques which are modelled here.

Finally I would thank my colleague Dr. Andrew Kao for the discussions about the work presented here which led to a greater understanding of the topic.

ABSTRACT

The aim of the work presented in this thesis is the development of two computational models of two processes that can be used to shape molten polymers on a micro-scale, namely Electrohydrodynamic Induced Patterning (EHDIP) and Electric Field Assisted Capillarity (EFAC). These related processes both use the dielectric forces at the interface between a polymer and another dielectric such as air. When the molten polymers are placed in a shaped electric field the imbalance in these dielectric forces causes the polymer to flow in a controlled way creating shapes in the polymer melt, this is the basis for the EHDIP process. The shaped electric field is controlled by the morphology of the top mask which acts as an electrode. This process is further extended by introducing a heavily wetted surface on the top mask which results in capillary forces that cause the polymer melt to coat the top mask creating a fully enclosed shape. This process can be used to create enclosed micro-channels or micro-capsules. Thus results and discussion presented herein highlight several possible application routes for industrial manufacturing. The process is discussed here for microstructures of 1 μm to 200 μm in size. The range at which the processes work is not fully understood, however the EHDIP process has been shown to work at a nanoscale producing structures around 100 nm in size.

From a comprehensive literature review, the underlying theory and mechanisms of this process were identified and the governing equations derived. Computational models were developed based on the underlying physics. These models were initially developed in PHYSICA version 3g and later they were implemented into COMSOL Multiphysics as the latter proved to be more stable. The results from the computational models were compared to the limited experimental data available.

The results from the computational models show that the mask shape was found to have the largest effect on the final structure of the shaped polymer. Due to capillary forces the shape of the microstructure at the top mask mimics the shape of the mask. In the lower section of the enclosed microstructure there is a force balance between surface tension, dielectric forces and internal pressure, giving a rounded morphology. Furthermore, by wetting the lower mask, flat bottomed structures can be produced. By both shaping and wetting the lower mask the shape of the microstructure can be even further modified. However, sharp cornered masks are unsuitable for this process. The effects of other key parameters such as air gap, contact angle, polymer permittivity and applied voltage were investigated through a sensitivity analysis.

Changing the permittivity is shown to have an effect on the final microstructure. The change is small; however the permittivity does affect the speed of the process. The contact angle between the top mask and the polymer modifies the thickness of the polymer at the top of the structures. Increasing the contact angle causes a decrease in polymer thickness

due to a reduction in the capillary force. The depth of the structures can be altered by changing the air gap; hence a larger air gap gives a deeper structure. The initial polymer thickness has no effect on the top of the structure but determines the thickness, shape and curvature of the lower part of the structure.

The applied voltage controls the electrostatic forces and hence the speed of the process. For a low voltage the electrostatic forces are not strong enough to initiate the process and an enclosed microstructure does not form. If the voltage is too high, the structure forms quickly and bubbles can be entrapped at the top mask.

With the correct mask shapes the processes can produce a wide variety of microstructures. These would have a wide range of applications either in the communications sector as fibre-optical wave-uides or in the biomedical sector as microstructures used in BioMEMS. Further development of the process is required to ensure that the process can be controlled. The models presented here are initial investigations of this but further experimental work is required along with the expansion of the model into three-dimensions.

CONTENTS

FIGURES

TABLES

NOMENCLATURE

Abbreviations

Bio-MEMS	Biological MicroElectroMechanical Systems
CFD	Computational Fluid Dynamics
EFAC	Electric Field Assisted Capillarity
EHDIP	Electrohydrodynamic Induced Patterning
LISA	Lithographically Induced Self Assembly
LISC	Litographically Induced Self Construction
UV	Ultra Violet

Constants

ϵ_0	permittivity of free space = 8.854 187 817... $\times 10^{-12}$ F/m

Greek Symbols

α	phase field constant
$\boldsymbol{\varsigma}$	displacement vector
$\boldsymbol{\xi}$	arbitrary infinitesimal displacement
χ	polymer thickness
$\dot{\gamma}$	magnitude of deformation

γ	surface tension coefficient
κ	curvature
λ	length scale of volume element $\tilde{V}_o$
μ	dynamic viscosity
ν	kinematic viscosity
Ω	potential energy
Φ	non-dimensional conjoining pressure
ϕ	free surface variable
ψ	phase field helper variable
ρ	density
σ	surface tension
θ	contact angle

Roman Symbols

$\bar{u}$	average velocity
$\boldsymbol{B}$	magnetic field
$\boldsymbol{D}$	electric displacement field
$\boldsymbol{E}$	electric field
$\boldsymbol{F}$	external body force
$\boldsymbol{H}$	magnetizing field
$\boldsymbol{m}$	surface tangent
$\boldsymbol{P}$	polarisation density
$\boldsymbol{r}$	position vector

$\boldsymbol{s}$	unit normal to closed contour C
$\boldsymbol{S}$	viscoelastic stress tensor
$\boldsymbol{T}$	stress tensor
$\boldsymbol{u}$	velocity
$\hat{\boldsymbol{n}}$	unit normal
$\hat{V}$	volume
$\tilde{F}$	force per unit area
$\tilde{V}$	control volume
C	closed contour
d	distance from interface
dl	line element
f	body force
g	acceleration due to gravity
h	distance from the surface
H_s	Heaviside function
K	kinetic energy
M	mobiltiy
p	pressure
R	molecular dimension
U	cohesive energy
V	voltage
X	non-dimensional spatial x coordinate

x	x component of displacement
Y	non-dimensional spatial y coordinate
y	y component of displacement
z	z component of displacement
Re	Reynold's number
Wi	Weisenberg number

Subscripts

$\boldsymbol{A}_1$	stretching tensor
$\boldsymbol{j}_f$	free current
$\boldsymbol{J}_m$	mass flux
ϵ_r	relativity permittivity
ϵ_{air}	permittivity of air
ϵ_{poly}	permittivity of polymer
ϵ_{st}	capillary width
γ_1	mobility
λ_{st}	magnitude of mixing energy
ω_c	chemical potential
Ω_{free}	free energy per unit volume
Ω_{int}	interaction potential
Ω_{mix}	mixing energy
ρ_f	free charge density
ρ_{air}	density of air

ρ_{poly}	density of polymer
$\tilde{V}_o$	volume element
C_p	polymer concentration
f_0	total free energy
H_{nd}	non-dimensional interface thickness
H_{sm}	smoothed Heaviside function
L_c	characteristic length scale
L_{rg}	Lagrangian
n_k	k^{th} component of normal to surface
p_i	intermolecular pressure
p_{el}	electrostatic pressure
p_{free}	pressure due to free energy
p_{tot}	total pressure
S_u	arbitrary surface
T_e	temperature
T_{nd}	non-dimensional time
V_o	volume
z_d	distance from lower surface

Chapter 1

INTRODUCTION

1.1 Thesis Overview

This thesis describes a computational model of two different but related processes. The first of these processes is known as Electrodynamic Induced Patterning, for which the shortening EHDIP will be used, the second is known as Electric Field Assisted Capillarity, or EFAC for short. These processes are defined bellow. The reasons that these processes are important it that although they are currently only carried out on a small scale in a lab they both show promise as techniques for the fabrication of polymer microstructures. Polymer microstructures have a wide range of potential uses mainly in the field of Biological MicroElectroMechanical Systems (Bio-MEMS) where they can be used as microchannels and microcapsules. In addition the techniques have the potential to be used in the manufacture of fibre-optical wave-guides.

Both of the processes described herein use shaped electrodes in order to shape the electric fields. These electrodes are referred to as masks in the majority of this work.

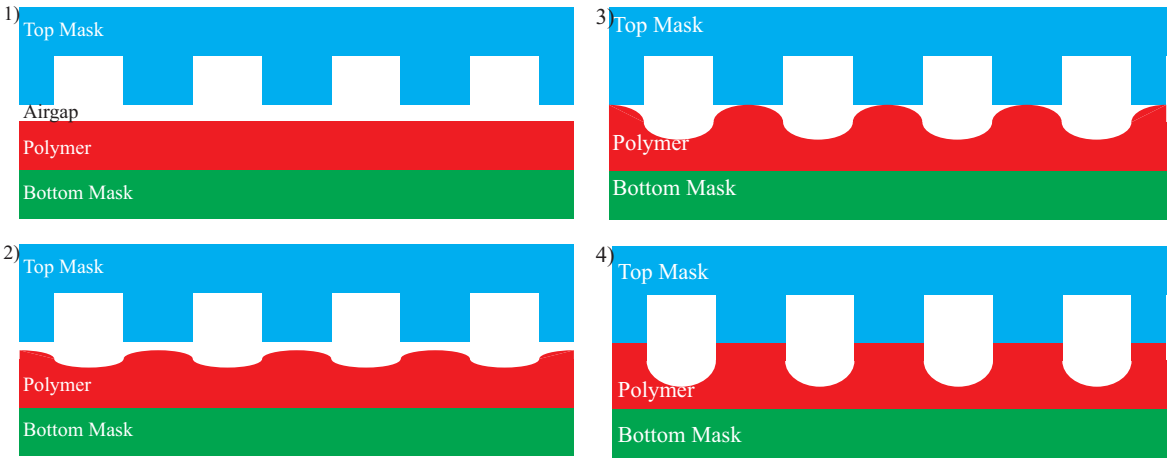

Figure 1.1: Diagram showing the EHDIP process.

1.2 Electrohydrodynamic Induced Patterning

Electrohydrodynamic induced patterning is a process that uses electric fields in order to shape molten polymers using the electrostatic and dielectric forces induced at the interface. It was discovered by looking at the effect of electrohydrodynamic instabilities in the surface of polymers at a sub micron scale. At this scale under uniform electric fields instabilities are created in the surface of a polymer as the entire surface is attracted to the electrode. Based on this, work was undertaken to look at the effect of shaping the top electrode or mask in order to shape the electric field. This created a difference in the electric field and so the electrostatic and dielectric forces at the interface between the polymer and the air. This meant that the polymer grew upwards in the shape of the top mask. Thus the polymer formed a pattern that was the same as the top mask. This was an exciting prospect as it gave a potential new method for the fabrication of polymer microstructures. Therefore further work was done looking at the process.

Figure (1.1) shows a schematic of this process. It starts (1) with two electrodes,

in the diagram denoted as top and bottom masks. The top mask is shaped, the bottom flat. The polymer is spin coated onto the lower surface producing a flat surface of polymer. The polymer should then be heated to just above its glass transition temperature, alternatively a UV (Ultra Violet) or temperature curable polymer may be used so it will already be semi-molten. In between this spun coated polymer and the top mask an air gap is left. Once the electric field is applied the top of the polymer is attracted to the top mask, this causes the polymer to begin to grow upwards in the regions where the mask is lower (2). Eventually the polymer reaches the top mask (3) this stops it from moving upwards and so it begins to spread along the top. Finally it completes the process and forms structures in the same pattern as the top mask (4). Surface tension dictates that the polymer structures formed have a curved bottom as this has the lowest surface energy.

1.3 Electric Field Assisted Capillarity

Electric Field Assisted Capillarity is an extension of the EHDIP process, it was discovered by accident when an EHDIP experiment was left running too long and it was noticed that the polymer had coated the top mask. On further investigation it was reasoned that this was due to a capillary force due to a small contact angle between the polymer and the top mask. This was investigated further and it was shown that enclosed micro-structures were able to be manufactured using this process.

Figure (1.2) demonstrates this process. As can be seen the process starts in a similar way to the EHDIP process, the polymer melt is spun coated onto the bottom mask and the shaped top mask is suspended above it with a small air gap (1). The polymer is attracted by the high regions of the electric field due to the electrostatic

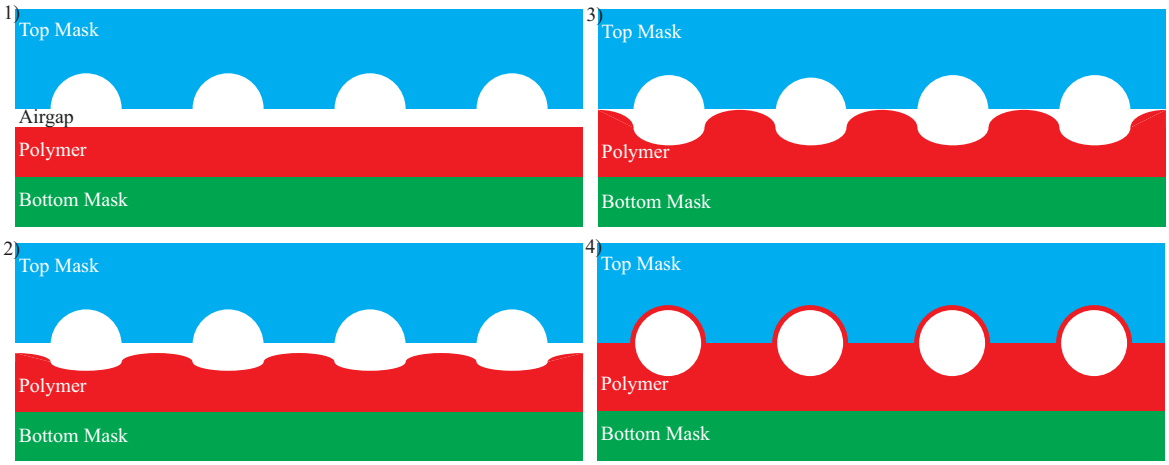

Figure 1.2: Diagram of the EFAC Process.

and dielectric forces and so begins to flow upwards under the protrusion of the top mask (2). After a period of time the polymer reaches the top mask (3), this is where the process differs from EHDIP as the small contact angle on the top mask means the polymer experiences a large capillary force and coats the top mask (4).

1.4 Aim and Objectives

The aim of the work presented here has evolved during the project as new aspects of the work were discovered. Initially the aim of this work was to develop a model of the EHDIP process in order to both inform the theory behind how the process works but also to inform development of the process into a manufacturing technique. However during the early stages of the project the EFAC process came to the attention of the author and her supervisors and so it was decided to include this in the modelling as it involved minor modifications to the original model. This meant that the ultimate aim of this project is to develop models for the EHDIP and EFAC techniques to assist in the usage of these techniques in the fabrication of polymer microstructures. To

achieve this aim four objectives were defined.

- The **first** objective was to perform a thorough literature review of the two processes and from this literature review gain an understanding of the state of the art and to develop the theory behind the processes. Chapters 2 and 3 fulfil this objective.
- The **second** objective was to develop computational models of the EHDIP process based on the theory developed in the first objective and to validate this model where possible. Chapters 4 and 5 fulfil this objective.
- The **third** objective was to develop further computational models of the EFAC process incorporating the contact angles on the top surface and to validate this model where possible. Chapters 4 and 5 fulfil this objective.
- The **fourth** objective was to use the computational models to perform sensitivity analysis on the EFAC process to observe how altering different variables effect the process. Chapter 6 fulfils this objective.

In addition to these objectives during the project potential extensions to the EHDIP and EFAC process were considered based on not only shaping the top mask but also the bottom mask, these extensions are also described in this document.

1.5 Chapter Summary

This document is split into seven chapters, this initial chapter gives an overview of the EHDIP and EFAC process and defines the projects aims and objectives.

The second chapter is the literature review and considers the current state of the art in experimental, theoretical and numerical work for EHDIP, EFAC and related processes. It also discusses the potential applications of polymer microstructures. This chapter is concerned with the first objective.

The third chapter discusses the theory behind the processes and develops from the theories discussed in the literature review. This chapter discusses the work to meet the first objective.

The fourth chapter outlines the development of the computational models for both the EHDIP and the EFAC process and how they were implemented. This chapter considers models developed to meet the second and third objectives.

The fifth chapter presents the results obtained from the computational models, it demonstrates results from the models developed in fulfilment of the second and third objectives of this work. In addition it also demonstrates the additional work done on expanding the EHDIP and EFAC processes by shaping the bottom mask.

The sixth chapter concerns the use of the model in running sensitivity analysis to inform the potential uses of the processes as manufacturing techniques. This chapter is in fulfilment of the fourth aim.

The seventh and final chapter summarises the other chapters and also discusses potential further extensions to the work presented here and as such demonstrates how the work has fulfilled the aims of the project.

1.6 Publications and Contributions to Research

The research presented in this document has contributed to 4 journal papers and 4 conference papers they are listed below. An additional invited paper is currently being

written based on the 2015 Eurosime conference paper.

Journal Papers

1. H. Chen, W. Yu, S. Cargill, M. K. Patel, C. Bailey, C. Tonry, M. P. Y. Desmulliez, **Self-encapsulated hollow microstructures formed by electric field-assisted capillarity**, *Microfluidics and Nanofluidics*, 13(1):75-82, 2012

2. Tonry, Catherine; K. Patel, Mayur; Bailey, Christopher; P.Y. Desmuliez, Marc; Cargill, Scott; Yu, Weixing, **A Method for the Micro-encapsulation of Dielectric Fluids in Joined Polymer Shells**, *Current Organic Chemistry*, 17(1):65-71, 2013

3. H. Li, W. Yu,L. Zhang, Z. Liu, K. E. Brown, E. Abraham, S. Cargill, C. Tonry, M. K. Patel, C. Bailey,M. P. Y. Desmulliez, **Simulation and modelling of sub-30 nm polymeric channels fabricated by electrostatic induced lithography**, *RSC Advances*, 23:11839-11845, 2013

4. G Liu, W Yu, H Li, J Gao, D Flynn, R W Kay, S Cargill, C Tonry, M K Patel, C Bailey and M P Y Desmulliez, **Microstructure formation in a thick polymer by electrostatic-induced lithography**, *Journal of Micromechanics and Microengineering*, 23:035018, 2013

Conference Papers

1. Tonry, C.; Patel, M. ; Bailey, C. ; Desmuliez, M.P.Y. ; Cargill, S. ; Yu, W., **Modelling of the Electric Field Assisted Capillarity Effect used for the fabrication of hollow polymer microstructures**, *Thermal, Mechanical and*

Multi-Physics Simulation and Experiments in Microelectronics and Microsystems (EuroSimE), 2012 13th International Conference on, IEEE, 2012

2. Catherine E. H. Tonry, Mayur K. Patel, Chris Bailey, and Marc P. Y. Desmuliez, **A Model of Electric Field Assisted Capillarity for the Fabrication of Hollow Microstructures**, *COMSOL 2012, Milan*, 2012

3. Tonry, C.E.H., Patel, M.K., Bailey, C., Desmuliez, M.P.Y. and Yu, W., **Micro-scale modelling challenges in electric field assisted capillarity**, *Proceedings. 12th International Symposium on Distributed Computing and Applications to Business, Engineering & Science. DCABES 2013*, 2013

4. C. Tonry, M. Patel, M. Desmuliez, W. Yu and C. Bailey, **Computational Electrohydrodynamics in the Fabrication of Hollow Polymer Microstructures**, *Thermal, Mechanical and Multi-Physics Simulation and Experiments in Microelectronics and Microsystems (EuroSimE), 2015 16th International Conference on*, IEEE, 2015

In addition to the published research the research presented here has contributed to the research on this topic in further ways

- Firstly this research has developed the understanding behind the theory of how the processes work.

- This research includes the first known computational models for both processes at a micro-scale.

- The results from the research have contributed to the understanding of the processes and how the different variables can be altered to change the process.

- The results presented here have made suggestions of how further experiments could be performed.
- The use of shaped masks at the top and the bottom has been added as a suggestion, this allows far more complex microstructures to be produced.

Chapter 2

LITERATURE REVIEW

2.1 Introduction

This thesis looks at two different but related methods for the fabrication of polymer microstructures, ElectroHydroDynamic Induced Patterning (EHDIP) and Electric Field Assisted Capillarity (EFAC). As summarised in the previous chapter they both use dielectric forces for the initial part of the process with EFAC adding in capillary force in order to produce enclosed structures.

2.2 Experimental Studies

The effect of electrostatic fields on thin polymers have been studied extensively since 1992 [1], where the effect of electrostatic films on the flow of polymers was studied, these studied showed instabilities in the surface of the films. Later Lithographically Induced Self-Assembly (LISA) was first described by Chou and Zhuang [2]. A process of inducing the growth of so called self-assembled columns in a thin polymer film is

described. The process involves placing a smooth thin homopolymer film between two substrates, one of which has a mask, the polymer is then heated uniformly to above the glass transition temperature and a series of hexagonal columns are formed. The results showed that though the columns were essentially randomly spaced under the mask they were generally a similar distance apart from each other. Also observed was that these hexagonal columns had flat tops, presumably due to contacting the top mask. When a triangular mask was used the pillars formed a regular triangular array of columns.

Lithographically Induced Self-Construction (LISC) was also first observed by Chou *et al.* [3]. The process is similar to that of LISA but instead of columns larger structures are formed. The basic process is more or less the same with the exception that the surface tension difference between the polymer and the mask needs to be reduced. When this difference is low enough the initial columns will spread and merge together.

Shortly after this Schäffer *et al.* [4], described a related process observed with the same initial set up but applying a potential difference between the top and bottom plates. Similar cases to both LISA and LISC with both patterned and unpatterned top masks were discussed.

Deshpande *et al.* [5–7] have looked at several aspects of this process. The first paper looking at the growth of the individual columns with a square unpatterned top mask. By filming the structures as they were growing, this demonstrated that the structures started forming around the edge of the plate and then grew and filled in the middle later forming a semi regular grid of columns. The second paper considers the effect of replacing the air with a liquid in this case oil, it is showed that the use of oil caused the columns to become less ordered. This they surmised is likely to be caused

by the change in the surface energy between the two fluids. The third paper considers the formation of concentric rings by using a top mask with a small circle in the centre. This forms ripples in the polymer which are then attracted to the top mask and grow forming the concentric rings.

Lin *et al.* [8–10] also have looked into this process mostly looking at liquid/liquid interface it is shown that the length scale of the instabilities is reduced with a liquid/liquid interface when compared to a liquid/air interface. This was shown to be due to a reduction in the interfacial surface tension.

Salac *et al.* [11] looked at the effect of placing the electric field parallel to the fluid surface rather than perpendicular. It was demonstrated that this produced instabilities in the film surface, but they were not regularly spaced, unlike those observed in LISA.

Further work has been preformed in using this process to form channels in the polymer [12–14]. Yang *et al.* [12] consider the use of this technique to replicate a top mask making channels of approx 400 nm in height and 10 μm wide, it is also stated that nanoscale fabrication using this technique is feasible. Hin *et al.* [13] considered applying the technique to waveguides for fibre optic devices. Structures 50 μm in height from an initial film thickness of 10 μm were produced. Pattader *et al.* [14] consider complex structures formed by spatiotemporal variation in the electric field.

The patterns provided by uniform electric field were also further consdiered by other authors [15–24]. Additionally further work looking at the LISC process on small scales has been published [25–32].

Work on the EHDIP process which is LISC applied at a larger scale has been published bu Liu *et al.* [33].

Some work has been done looking at the process applied to materials other than polymers [34; 35]. Gill *et al.* [34] used molten gold and show the assembly of pillars

under an electric field, though they are not as regular as those observed with a polymer. Brown *et al.* [35] however applied the process to oil in order to create a programmable optical interface.

Lyuksyutov *et al.* [36] have looked into using an AFM tip rather than a top mask to shape the polymer. The advantage of this is that a pre defined mask is not required to produce the patterning, however the patterns produced seem to be less defined. Xie *et al.* [37] also looked at this process.

At the start of this work the author could not find any papers published on the EFAC process, work had been done on using capillary force to shape polymers [38–41]. This work combined with the work on EHDIP results in the EFAC process, there have since been two papers looking at the early experimental work, in addition to the modelling work outlined in this thesis [42; 43].

2.3 Theoretical Studies

One of the first papers looking at the theory behind LISA was by Z. Suo and J. Liang [44]. It is discussed that the process is caused by instabilities in the interface between two insulating fluids, or between an insulating and a conducting fluid. It is further discussed how these instabilities occur by looking at them in terms of the energetics of the system. As the materials are both fluid they can flow and so change configuration to reduce the energy of the system. This energy is the combination of the interfacial energy and the electrostatic free energy. By using the simple case of two perfectly dielectric fluids it is shown that any columnar distribution of the fluid has a lower electrostatic free energy than a laminar configuration. It is surmised that this therefore drives the fluid flow from a lamellar to a columnar configuration, at the cost

of some interfacial energy. It is conjectured that this does not then explain the uniform "island sizes" observed. These are considered to be caused by a slight conduction in at least one of the fluids. Thus the dielectrics need to be assumed to be imperfect or "leaky" dielectrics with mobile charges. These charges are then moved by the electric field collecting at either the top or the bottom of the columns. This then is shown to be the reason for the regular sizing and spacing of the columns.

Several papers have looked at a stability analysis of the process [45–51]. Results from these analyses generally show that the growth rate of the system is proportional to the Deborah number of the polymer, the Deborah number is a dimensionless quantity related to the materials ability to flow obtained by dividing the stress relaxation time of a material by the time-scale of the observations. These papers also look at the relationship between the growth rate and the wavenumber of the column distribution. Koulova-Nenova *et al.* [50] also look at the relationship between the electrical Rayleigh number and the wavenumber.

Further theoretical studies of the LISA and LISC processes have been undertaken [26; 52–60]

2.4 Numerical Studies

There have been several attempts to simulate this process numerically, Kim and Lu [61] produced a coupled model of diffusion, viscous flow, surface energy and dielectric effect. These are solved using a diffuse interface framework to model the surface. A semi-implicit Fourier spectral method and a preconditioned bi-conjugate gradient method is used to solve the equations numerically. This model considers the kinematics, for

which the flow flux is defined in terms of the material concentration

$$\frac{\partial C_p}{\partial t} + \nabla \cdot \boldsymbol{J}_m = 0, \tag{2.1}$$

where C_p is the concentration and $\boldsymbol{J}_m$ the mass flux.

The energetics are defined as as the Gibbs free energy in terms of the phase configuration and the electric field distribution

$$G = \int_{\hat{V}} \left\{ f(C_p) + \frac{1}{2} h \left| \nabla C_p \right|^2 - \frac{1}{2} \epsilon_0 \epsilon_r (C_p) \left| \nabla V \right|^2 \right\} d\hat{V}, \tag{2.2}$$

where ϵ_0 is the permittivity of free space, ϵ_r the relative permittivity and V the electric potential.

For the kinetics a convective Cahn-Hilliard equation and a modified Navier-Stokes equation are obtained

$$\frac{\partial C_p}{\partial t} + \boldsymbol{u} \cdot \nabla C_p = \nabla \cdot \left(M \nabla \mu_c \right), \tag{2.3}$$

$$\rho \left(\frac{\partial \boldsymbol{u}}{\partial t} + \boldsymbol{v} \cdot \nabla \boldsymbol{u} \right) = -\nabla p + \nabla \cdot \left(\nu \nabla \boldsymbol{u} \right) + \omega_c \nabla C_p, \tag{2.4}$$

where ω_c is the chemical potential, $\boldsymbol{u}$ the velocity, M the mobility and ν the kinematic viscosity.

These equations were then normalised and solved using a semi-implicit Fourier spectral method. To do this the Cahn-Hilliard equation (2.3) is seperated into linear and non-linear parts then solving the linear parts implicitly and the non-linear parts explicitly. Then the semi-backward differentiation formula for the time integration is used to ensure stability.

Using this model the evolution of several different cases is simulated. Starting with

the case of an unshaped top mask using a voltage density comparable to experimental data. These simulations showed the growth of the columns starting with small amplitude ripples in the surface which begin to grow, achieving relatively uniform pillars by the end of the simulation. Increasing the voltage across the two plates increased the growth rate and reduced the size and spacing of the columns. After an unshaped top plate a case with a shaped top plate looking at the patterns formed is attempted. With a small film thickness this produced columns but only under the areas where the mask was embossed. Increasing the film thickness with an unpatterned top plate does not effect the size of the columns produced. However it does cause them to be closer together and to grow quicker than a thinner film. A thicker film with a shaped top mask which produced a copy of the top mask in the film is demonstrated. Finally investigations of the effect of changing the surface energy, this showed that increasing the surface energy reduced the growth rate and size of the columns.

Verma *et al.* have published two papers looking at simulating the process [62; 63]. Both used essentially the same model but used it to investigate different aspects of the process. Using the long-wave approximation of the Navier-Stokes equation given by

$$3\mu\frac{\partial\chi}{\partial t} - \nabla\cdot\left[\chi^3\nabla p_{tot}\right] = 0, \tag{2.5}$$

where p_{tot} is the total pressure and χ the thickness of the polymer

For the pressure an expression, at the free interface $z = \chi(x, y, t)$, is used for the normal stress condition. This relates the pressure to the curvature, the intermolecular pressure and the Maxwell stress tensor

$$p_{tot} = p_0 - \gamma\nabla^2\chi + p_i + \frac{\epsilon_0\left[\epsilon_{poly}\left(\frac{\partial V_p}{\partial z}\right)^2 - \epsilon_{air}\left(\frac{\partial V_a}{\partial z}\right)^2\right]}{2}, \tag{2.6}$$

where p_0 is a reference pressure, p_i is the intermolecular pressure and ϵ_{poly} and ϵ_{air} the relative permittivities in the polymer and the air respectively. It is assumed that the fluid was a perfect dielectric so the charge is concentrated at the interface between the liquid and the air. By using the long wave limit it can be assumed that the electric potential (V) is constant in the x, y plane and only changes in the z direction giving

$$\frac{\partial^2 V_p}{\partial z^2} = 0; \frac{\partial^2 V_a}{\partial z^2} = 0, \tag{2.7}$$

Solving (2.7) with appropriate boundary conditions gives

$$V_p = V_b \left\{ 1 + \frac{z}{\epsilon_{poly} d - h\left(\epsilon_{poly} - 1\right)} \right\}, \tag{2.8}$$

$$V_a = V_b \epsilon_{poly} \left\{ \frac{z - d}{\epsilon_{poly} d - h\left(\epsilon_{poly} - 1\right)} \right\}, \tag{2.9}$$

where d is the distance from the fluid-fluid interface. Substituting (2.8) and (2.9) into (2.6)

$$p_{tot} = p_0 - \gamma \nabla^2 h + p_i + p_{el}, \tag{2.10}$$

where the electrostatic pressure p_{el} is

$$p_{el} = -0.5 \epsilon_0 \epsilon_{poly} \left(\epsilon_{poly} - 1\right) E_{poly}^2, \tag{2.11}$$

and

$$E_p = \frac{V_b}{\epsilon_{poly} d - \left(\epsilon_p - 1\right) h}, \tag{2.12}$$

substitution back into (2.5) gives

$$3\mu \frac{\partial h}{\partial t} - \nabla \cdot \left[h^3 \nabla \Omega_{int} \right] + \nabla \cdot \left[h^3 \nabla \left(\gamma \nabla^2 h \right) \right] = 0, \tag{2.13}$$

where Ω_{int} is the total interaction potential consisting of the electric potential the van de Waals potential and a short-range Born repulsion. The van de Waals force and Born repulsion can be represented as

$$\Omega_{vdW} + \Omega_{Br} = \frac{A}{6\pi h^3} + \frac{6B_{c1}}{(d-h)^7}. \tag{2.14}$$

Using linear stability analysis the time-scale of the growth of the instabilities is obtained by

$$t_r = \frac{1}{\omega_m} \ln\left(\frac{h_0}{\epsilon}\right) = 12\mu\gamma \left[h_0^3 \left((\phi_h)_0\right)^2\right]^{-1} \ln\left(\frac{h_0}{\epsilon}\right). \tag{2.15}$$

Normalising the time and length scales gives the equation

$$\frac{\partial H_{nd}}{\partial T_{nd}} + \nabla \cdot \left[H_{nd}^3 \nabla \left(\nabla^2 H_{nd}\right)\right] - \nabla \cdot \left[H_{nd}^3 \nabla \Phi\right] = 0. \tag{2.16}$$

where $H(X, Y, T)$ is the non-dimensional thickness of the interface, T_{nd} the non-dimensional time, X and Y the non-dimensional spatial coordinates and Φ the non-dimensional conjoining pressure.

This equation is solved using the central difference scheme with the Everett method interpolation. Periodic boundary conditions were applied at the edges of the domain, and an initial random disturbance of a small amplitude was used to simulate the instabilities. The results from the simulations showed the evolution of the expected columns from an initial random distribution, with thicker films causing these columns to join together when they reached the top plate. With a circular protrusion in the centre of the top plate the columns formed into concentric circles, these joining to

form circles when there is enough polymer so it does not fully deplete. With a ridged top mask the ridges were duplicated in the film. A top mask consisting of an array of bumps caused the columns to just grow beneath those bumps. Craster *et al.* [64] also developed a model using the same techniques.

These models all consider the behavioured of the instabilities of the polymer at the nano-scale, however this thesis considers the process on a micro-scale where different physics are dominant.

2.5 Applications

There are several possible applications for the EHDIP process, one of the main ones being investigated at the moment is its use in fabricating channels for microfluidic devices [65]. The primary use for microfluidic devices currently are in the biomedical fields, uses for such devices are well documented in the literature [66–72].

It also has potential applications in the manufacture of wave-guides [13] as it can be used to shape the suitable materials. It has the added advantage that it is erasable in that when the polymer is heated again to above its glass transition temperature it should go back to its original shape and may be reused [44].

Alternative methods for the construction of microchannels and wave-guides include chemical etching, sacrificial layers and substrate swelling; these both rely on controlled chemical reactions in order to remove material to leave channels behind or to swell polymers [73–75]. Other comping methods usually rely on embossing to impact print the channels into the polymer [18; 76–78]. There have also been many review papers looking at the advantages and disadvantages of competing channel fabrication techniques and their applications [79–85].

As EFAC is still in its early stages the full range of applications have not been developed though it has a potential use for the EFAC method is that of producing microcapsules for bio-medical applications. These microcapsules could be used to encapsulate fluids. Competing methods for the encapsulation of fluids in either cellulose nitrate or polyamide membranes [86], or suspension in alginate gels [86], collagen, chitosan or agarose [87].

Examples of uses of joined microcapsules which can be produced by the EFAC process include the use of microcapsules to enclose drug molecules [88–91] these can then be made sensitive to heat or ultrasound [92] in order to release the drugs when they reach the correct location in a body, or gradually over time. Another potential application for microcapsules produced by EFAC is that of a bio-artificial pancreas [93], by using a permeable polymer along with the EFAC technique capsules could be produced containing insulin producing cell islets, with the partial permeable polymer protecting the islets from the bodies immune system thus reducing the chance of rejection of the cells.

Further applications of the technology include the fabrication of micro-lens arrays for use in LED lenses [78]. These types of lenses are used for LED lighting which is currently a growth area.

2.6 Summary

Both EFAC and EHDIP are currently only performed at a laboratory scale and neither is currently fully understood in terms of the forces involved in the processes. The theoretical work on similar processes is mostly focused on the instabilities created in the surfaces of the polymer. This becomes unimportant when moved to the larger micro-

scale, which is where most experiments; theoretical studies; and models are considered. There also only a few papers that have been published which consider the addition of the capillary force to the process. This has the potential to make the fabrication of enclosed structures a simpler process than any current technology. The applications for such enclosed microstructures are wide ranging from biomedical devices that require microchannels, microcapsules and combinations of the two, to optical communications devices which require microscale wave-guides to act as switching devices.

Chapter 3

THEORY

3.1 Introduction

There are two primary driving forces in the EHDIP and EFAC processes: dielectric forces and surface tension. These forces are both concentrated around the polymer/air interface. The dielectric forces are due to a gathering of charge at the polymer/air interface due to the change in permittivity. The surface tension forces are caused by an imbalance of van de Waals forces between the two interfaces due to different distributions of molecules.

3.2 Electrostatics and Dielectric Forces

The primary materials involved in both the EHDIP and EFAC process are dielectrics. It can therefore be assumed that there is zero free charge in the bulk of the materials. With no free charge there can be assumed to be no electric current in the fluids. Hence no interaction with magnetic fields and so electrostatics equations may be used. In

addition with no free charge in the bulk of the fluid any electrostatic forces will be dielectric forces which are concentrated at the interface between the two fluids.

3.2.1 Maxwell's Equations in Dielectrics

Maxwell's Equations are defined as

$$\nabla \cdot \boldsymbol{D} = \rho_f, \tag{3.1}$$

$$\nabla \cdot \boldsymbol{B} = 0, \tag{3.2}$$

$$\nabla \times \boldsymbol{E} = -\frac{\partial \boldsymbol{B}}{\partial t}, \tag{3.3}$$

$$\nabla \times \boldsymbol{H} = \boldsymbol{j}_f + \frac{\partial \boldsymbol{D}}{\partial t}, \tag{3.4}$$

where $\boldsymbol{D}$ is the electric displacement field, ρ_f the free charge density, $\boldsymbol{B}$ the magnetic field, $\boldsymbol{E}$ the electric field, $\boldsymbol{H}$ the magnetizing field and $\boldsymbol{j}_f$ the free current.

As the free charge density (ρ_f) can be considered to be zero in the bulk a dielectric (3.1) may be rewritten as

$$\nabla \cdot \boldsymbol{D} = 0, \tag{3.5}$$

(3.5) can then be used to describe the electric displacement field, the electric displacement field is defined as $\boldsymbol{D} = \epsilon_0 \epsilon_r \boldsymbol{E}$ and the electric field is defined as $\boldsymbol{E} = \nabla V$ therefore (3.5) can be rewritten as

$$\nabla \cdot \nabla \epsilon_0 \epsilon_r V = 0. \tag{3.6}$$

The magnetic field can be neglected, $\boldsymbol{B} = 0$ therefore $\partial \boldsymbol{B}/\partial t = 0$ and (3.3) may be

rewritten

$$\nabla \times \boldsymbol{E} = 0. \tag{3.7}$$

By definition $\boldsymbol{E} = \nabla V$ for dielectrics and this equation gives the identity

$$\nabla \times (\nabla V) \equiv 0. \tag{3.8}$$

Thus the governing equation that needs to be solved to obtain the voltage profile and therefore the electric field in dielectrics is (3.6).

3.2.2 Dielectric Forces

At the interface of the material there will be electrostatic forces due to the surface charge, there will be also dielectric forces due to changes in material properties. Landau [94] derived an equation for these forces on a fluid dielectric in an electric field. However Landau's derivation was in Gaussian units so the equation is re-derived here in SI units.

Starting with the law of conservation of momentum, the force acting on a volume $d\hat{V}$ is the change in momentum per unit time. The change in momentum must then be equal to the momentum passing through its surface per unit time. Denoting this change in momentum by the stress tensor $-T_{ik}$ then

$$\int f_i d\hat{V} = \oint T_{ik} df_k, \tag{3.9}$$

where T_{ik} is the ik^{th} element of the stress tensor, f_i the i^{th} component of the body force and f_k the k^{th} component of the body force.

It can be shown that $T_{ik} df_k = T_{ik} n_k df$ is the ith component of the force on a surface element, where n_k is the unit normal. It can also be shown that the total torque of a

given volume can be reduced to a surface integral. The surface integral in (3.9) can be transferred to a volume integral, obtaining

$$\int f_i d\hat{V} = \int (\partial T_{ik}/\partial x_k) dV_o, \tag{3.10}$$

where V_o is an arbitrary volume and x_k is the k^{th} component of displacement. Since the volume is arbitrary this can be reduced to

$$f_i = \left(\frac{\partial T_{ijk}}{\partial x_k} \right), \tag{3.11}$$

which is the formula for a body force in terms of a stress tensor. To calculate the stress tensor small regions of the surface need to be considered, they can be regarded as planes and the properties can be regarded as uniform. By considering a plane-parallel layer of material, in a uniform electric field, this can be assumed to be like a parallel plate capacitor. When one of the plates is translated over an arbitrary infinitesimal displacement $\boldsymbol{\xi}$ and assuming the potential of the conductor remains unchanged and that the deformation is homogeneous then the translation is isothermal.

A force $-T_{ik}n_k$ is then exerted on a unit area of the surface and so work is done of $-T_{ik}n_k\boldsymbol{\xi}_i$. This is assumed to be an isothermal deformation and is equal to the decrease in $\int \tilde{F} dV_o$, which is $h\tilde{F}$ per unit surface area. This gives

$$T_{ik}\boldsymbol{\xi}_i n_k = \delta \left(h\tilde{F} \right) = h\delta\tilde{F} + \tilde{F}\delta h, \tag{3.12}$$

where n_k is the component of the normal to the surface, $\tilde{F}$ the force per unit area and h the distance from the surface. h and n_k are shown in figure (3.1)

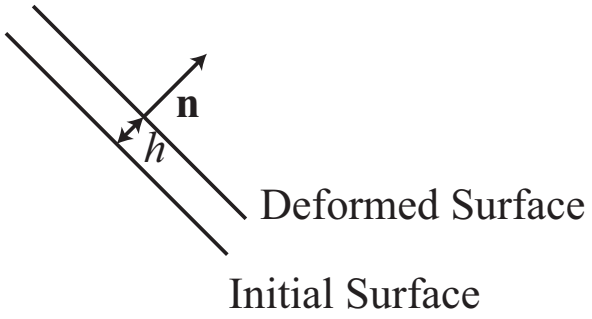

Figure 3.1: Diagram of an arbitrary deformation in direction $\boldsymbol{n}$.

The thermodynamic quantities of a fluid depend only on its density; deformations which do not change the density do not effect the thermodynamic state. Therefore we can write that for isothermal variation $\delta\tilde{F}$ in a fluid:

$$\delta\tilde{F} = \left(\frac{\partial\tilde{F}}{\partial\boldsymbol{E}}\right)_{T_e,\rho} \cdot \delta\boldsymbol{E} + \left(\frac{\partial\tilde{F}}{\partial\rho}\right)_{\boldsymbol{E},t} \delta\rho = -\epsilon_0 \boldsymbol{D} \cdot \delta\boldsymbol{E} + \left(\frac{\partial\tilde{F}}{\partial\rho}\right)_{\boldsymbol{E},t} \delta\rho, \tag{3.13}$$

where T_e is the temperature.

The change in density of the layer can be related to its change in thickness as $\delta\rho = -\rho\delta h/h$. This allows the calculation of the variation of the field. At a given point, with a position vector $\boldsymbol{r}$ there will be material which was originally at position $\boldsymbol{r} - \boldsymbol{u}$, where $\boldsymbol{u}$ represents the particle displacement vector. Due to the conditions stated, each particle carries its potential with it. Therefore the change in the potential at a given point is represented by

$$\delta V = V\left(\boldsymbol{r} - \boldsymbol{\varsigma}\right) - V\left(\boldsymbol{r}\right) = -\boldsymbol{\varsigma} \cdot \nabla V = \boldsymbol{\varsigma} \cdot \boldsymbol{E}, \tag{3.14}$$

where $\boldsymbol{r}$ is the position vector and $\boldsymbol{\varsigma}$ the displacement vector As the deformation is

homogeneous

$$\boldsymbol{\varsigma} = \frac{z_d \boldsymbol{\xi}}{h}, \tag{3.15}$$

where z_d is the distance from the lower surface. The variation of the field is therefore

$$\delta \boldsymbol{E} = -\frac{\boldsymbol{n}\left(\boldsymbol{E}\cdot\boldsymbol{\xi}\right)}{h}. \tag{3.16}$$

Substituting (3.16) into (3.13) and noting that $\delta h = \xi_z = \xi \cdot \boldsymbol{n}$, gives

$$T_{ik}\xi_i n_k = \epsilon_0 \left(\boldsymbol{n}\cdot\boldsymbol{D}\right)\left(\boldsymbol{\xi}\cdot\boldsymbol{E}\right) - \boldsymbol{\xi}\cdot\boldsymbol{n}\rho\frac{\partial \tilde{F}}{\partial \rho} + \boldsymbol{\xi}\cdot\boldsymbol{n}\tilde{F} \tag{3.17}$$

$$= \left(\epsilon_0 E_i D_k - \rho\frac{\partial \tilde{F}}{\partial \rho}\delta_{ik} + \tilde{F}\delta_{ik}\right)\xi_i n_k, \tag{3.18}$$

giving the expression for the stress tensor

$$\sigma_{ik} = \left[\tilde{F} - \rho\left(\frac{\partial \tilde{F}}{\partial \rho}\right)_{\boldsymbol{E},t}\right]\delta_{ik} + \epsilon_0 E_i D_k. \tag{3.19}$$

By assuming an isotropic media, $\boldsymbol{E}$ and $\boldsymbol{D}$ can be considered to be parallel. Then $E_i D_k = E_k D_i$ and so the stress tensor is symmetrical. In isotropic media the linear relation $\boldsymbol{D} = \epsilon_r \boldsymbol{E}$ must be satisfied giving

$$\tilde{F} = \Omega_{free}\left(\rho, T\right) - \frac{\epsilon_0 \epsilon_r E^2}{2}, \tag{3.20}$$

c

where Ω_{free} is the free energy per unit volume in the absence of the electric field. The pressure is known to be the derivative of the free energy per unit mass for a given

volume

$$-p_{free} = \Omega_{free} - \rho \left(\frac{\partial F_0}{\partial \rho} \right)_T = \left[\frac{\partial}{\partial \frac{1}{\rho}} \left(\frac{F_0}{\rho} \right) \right]_T . \tag{3.21}$$

Therefore the pressure due to the free energy in the absence of the field $p_{free} = p_{free}(\rho, T)$ can be substituted into (3.19) and (3.20) giving

$$T_{ik} = -p_{free}\left(\rho, T\right) \delta_{ik} - \frac{\epsilon_0 E^2}{2} \left[\epsilon_r - \rho \left(\frac{\partial \epsilon}{\partial \rho} \right)_T \right] \delta_{ik} + \epsilon_0 \epsilon_r E_i E_k. \tag{3.22}$$

In a vacuum (3.22) reduces down to the Maxwell Stress tensor for the electric field

When stationary, the forces exerted on the surface of separation of two adjoining dielectric media must be equal and opposite so $T_{ik} n_k = -T'_{ik} n'_k$, as they are opposing normals $n_k = -n'_k$ leads to

$$T_{ik} n_k = T'_{ik} n_k. \tag{3.23}$$

At the boundary of two isotropic media the tangential forces must also be equal. From (3.19) into (3.23) becomes $\boldsymbol{E}_t \boldsymbol{D}_n = \boldsymbol{E}'_t \boldsymbol{D}'_n$ showing that $\boldsymbol{E}_t$ and $\boldsymbol{D}_n$ must be continuous at the boundary.

The condition on the normal forces is however a non-trivial condition on the pressure difference between the two media. If we consider a boundary between a liquid and air where in air it can be assumed $\epsilon_r = 1$. By using the quantities associated with the atmosphere and using (3.22) gives

$$-P_0\left(\rho, T\right) + \frac{\epsilon_0}{2} E^2 \rho \left(\frac{\partial \epsilon_r}{\partial \rho} \right)_{T_e} + \frac{\epsilon_r \epsilon_0}{2} \left(E_n^2 - E_t^2 \right) = -P_{atm} + \frac{\epsilon_0}{2} \left(E_n'^2 - E_t'^2 \right). \tag{3.24}$$

Using the boundary conditions $\boldsymbol{E}_t = \boldsymbol{E}'_t, \boldsymbol{D}n = \epsilon_r \boldsymbol{E}_n = \boldsymbol{D}'_n = \boldsymbol{E}'_n$, (3.24) can be rewritten as

$$P_0(\rho, T) - P_a tm = \frac{\epsilon_0}{2} E^2 \rho \left(\frac{\partial \epsilon_r}{\partial \rho}\right)_T - \frac{\epsilon_0 (\epsilon_r - 1)}{2} \left(\epsilon_0 \epsilon_r E_n^2 + E_t^2\right). \tag{3.25}$$

To determine the body forces acting on the dielectric, (3.11) is substituted into the derivative of (3.22) with respect to x giving

$$f_i = \frac{\partial}{\partial x_i}\left[-P_0 + \frac{\epsilon_0}{2}\rho\left(\frac{\partial \epsilon_r}{\partial \rho}\right)_T\right] - \frac{\epsilon_0}{2} E^2 \frac{\partial \epsilon_r}{\partial x_i} + \epsilon_0 \left[-\frac{1}{2}\epsilon_r \frac{\partial}{\partial x_i} E^2 + \frac{\partial}{\partial x_k}(E_i D_k)\right], \tag{3.26}$$

then using $\nabla \cdot \boldsymbol{D} \equiv \frac{\partial \boldsymbol{D}_k}{\partial x_k} = 0$ the previous equation may be reduced to

$$-\epsilon_r E_k \frac{\partial E_k}{\partial x_i} + D_k \frac{\partial E_i}{\partial x_k} = -D_k \left(\frac{\partial E_k}{\partial x_i} + \frac{\partial E_i}{\partial x_k}\right), \tag{3.27}$$

which is zero as $\nabla \times \boldsymbol{E} = 0$. 3.25 becomes

$$\boldsymbol{f} = -\nabla P_0(\rho, T) + \frac{1}{2}\nabla\left[E^2 \rho \left(\frac{\partial \epsilon}{\partial \rho}\right)_T\right] - \frac{1}{2}\boldsymbol{E}^2 \nabla \epsilon. \tag{3.28}$$

If there is extraneous free charge in the fluid with a charge density ρ_f, (3.28) becomes

$$\boldsymbol{f} = \rho_f \boldsymbol{E} - \nabla P_0(\rho, T) + \frac{1}{2}\nabla\left[E^2 \rho \left(\frac{\partial \epsilon}{\partial \rho}\right)_T\right] - \frac{1}{2}\boldsymbol{E}^2 \nabla \epsilon, \tag{3.29}$$

which is the expression for the dielectric and electrostatic forces at the interface. In this case P_0 can be considered to be part of the Navier-Stokes equation and there is assumed to be zero free charge in the bulk of the fluid. This means that (3.29) can so

be reduced to

$$\boldsymbol{f} = \frac{1}{2}\nabla\left[E^2\rho\left(\frac{\partial\epsilon}{\partial\rho}\right)_T\right] - \frac{1}{2}\boldsymbol{E}^2\nabla\epsilon. \tag{3.30}$$

3.3 Surface Tension and Capillary Force

3.3.1 Surface Tension

Surface tension is a result of the mutual attraction of molecules in liquids. In the bulk of a fluid these cohesive forces are equal in every direction, which results in a zero net force. However near the surface of a liquid there are no corresponding molecules on the other side of the interface, this results in a net force and the molecules are pulled inwards. This in turn pulls all surfaces of the fluid inwards, resulting in an internal pressure which balances this force. If each molecule in the bulk of a fluid has a cohesive energy of U then at a flat surface each molecule at the surface will instead have a cohesive energy of $\frac{U}{2}$, thus the energy it has lost is also $\frac{U}{2}$. The surface tension coefficient γ is defined as the energy lost per unit area so in terms of the molecular dimension R the surface tension is $\gamma\ U/(2R^2)$. Therefore the surface tension of a material increases as its molecular attraction decreases. Dimensionally surface tension is a surface force, or an interfacial energy per unit area. Between two different immiscible fluids (miscible fluids mix and so there is no surface tension) there is obviously differing attractions of the molecules. Thus the interfacial tension is reduced due to these opposing forces compared to that of a surface.

The pressure due to the surface tension tends to be an isotropic force per area which acts through the whole bulk fluid. This means that a small surface element dS_u

will experience a total force of $p(x)dS$ due to the local pressure $p(x)$. If the surface S_u is a closed surface and the pressure is uniform, the total pressure force acting on S_u will be zero so the fluid will remain static. As in all fluids the gradient of the pressure is equal to the resultant body forces within the fluid. As it is a surface pressure the surface tension has the units of force per unit length. So if we consider for simplicity a flat interface between two fluids. A line element of this surface dl will experience a total surface tension force of γdl owing to the local surface tension $\sigma(x)$. If the surface is a closed loop, the net surface tension will be zero and so the fluid will remain stationary. If there are gradients in the surface tension however there will be a net force perpendicular to the surface which will therefore distort it and drive flow.

The governing equations of surface tension for fluids start with the Navier-Stokes equations

$$\rho\left(\frac{\partial \boldsymbol{u}}{\partial t} + \boldsymbol{u}\cdot\nabla\boldsymbol{u}\right) = -\nabla p + \boldsymbol{F} + \mu\nabla^2\boldsymbol{u}, \tag{3.31}$$

$$\nabla\cdot\boldsymbol{u} = 0. \tag{3.32}$$

These equations in 3D represent 4 equations and 4 unknowns (the pressure and the three velocity components). $\boldsymbol{F}$ represents any external body force acting on the fluid. Surface tension only acts at the surface of a fluid, and so in this case it does not appear in the Navier-Stokes equations (though when using a free surface method this is not the case and will be discussed further in the numerics section) it is instead incorporated into the boundary conditions. These boundary conditions can be derived by considering the stresses at the interface between two immiscible fluids.

The normal and tangential stress boundary conditions need to be derived at the

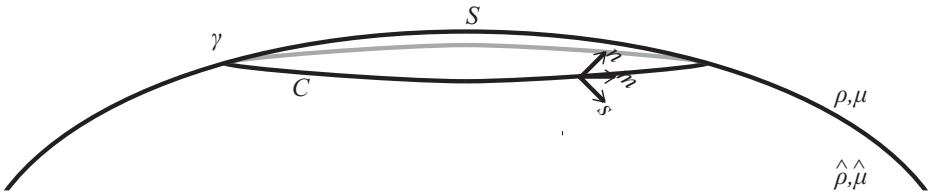

Figure 3.2: Surface (S) bounded by a contour (C) on an interface between two fluids, $\boldsymbol{n}$ is the unit outward normal to the surface and $\boldsymbol{m}$ a tangent, $\boldsymbol{s}$ is the unit normal to C and so a tangent to S.

interface between two fluids, characterised by the surface tension coefficient γ. In order to derive these we first consider a surface S which is bounded by a closed contour C, see figure (3.2). There is therefore a force per unit length of magnitude γ in the $\boldsymbol{s}$-direction for every point along the contour C, this will act to flatten the surface. Looking at the force balance on a volume $\tilde{V}$ enclosed by the interfacial surface gives

$$\int_{\tilde{V}} \rho \frac{D\boldsymbol{u}}{Dt} d\tilde{V} = \int_{\tilde{V}} \boldsymbol{f} d\tilde{V} + \int_{S} \left[T_s(\boldsymbol{n}) + \hat{T}_s(\hat{\boldsymbol{n}}) \right] dS + \int_{C} \gamma s dl, \tag{3.33}$$

where dl represents a length increment along C and $T_s(\boldsymbol{n}) = \boldsymbol{n} \cdot \boldsymbol{T}$ represents the stress vector, this is the force per unit area on the interface exerted by the upper fluid. The stress tensor $\boldsymbol{T}$ is defined by the local fluid pressure and velocity field as

$$\boldsymbol{T} = -p\boldsymbol{I} + \mu \left[\nabla \boldsymbol{u} + (\nabla \boldsymbol{u})^T \right]. \tag{3.34}$$

The stress exerted on the lower fluid is therefore

$$\hat{T}_s(\hat{\boldsymbol{n}}) = \hat{\boldsymbol{n}} \cdot \hat{\boldsymbol{T}}, \tag{3.35}$$

where

$$\hat{\boldsymbol{T}} = -\hat{p}\boldsymbol{I} + \mu \left[\nabla \hat{\boldsymbol{u}} + (\nabla \hat{\boldsymbol{u}})^T \right]. \tag{3.36}$$

The individual terms of (3.33) have various physical interpretations. The LHS is the internal force associated with the acceleration of a fluid within the volume V. The first term on the RHS is the body forces acting on the fluid enclosed by $\tilde{V}$. The second term on the RHS is the sum of the hydrodynamic forces exerted by the two fluids and the final term is the surface tension force along the contour C.

If we define the typical length scale of the volume element $\tilde{V}_o$ as λ then the acceleration and body forces will scale as λ^3 and the surface forces will scale as λ^2. As $\lambda \longrightarrow 0$ the surface forces must balance giving

$$\int_S \left[t_s(\boldsymbol{n}) + \hat{t}_s(\hat{\boldsymbol{n}}) \right] dS + \int_C \gamma s dl = 0. \tag{3.37}$$

As $\hat{\boldsymbol{n}} = -\boldsymbol{n}$

$$T_s(\boldsymbol{n}) = \boldsymbol{n} \cdot \boldsymbol{T}, \hat{t}(\boldsymbol{n}) = \hat{\boldsymbol{n}} \cdot \hat{\boldsymbol{T}} = -\boldsymbol{n} \cdot \hat{\boldsymbol{T}}. \tag{3.38}$$

Applying stokes theorem to the surface tension term gives

$$\int_C \gamma dl = \int_S \left(\nabla_s \gamma - \gamma \boldsymbol{n} \left(\nabla_s \cdot \boldsymbol{n} \right) \right) dS, \tag{3.39}$$

where the tangential gradient operator ∇_s is defined as

$$\nabla_s = [\boldsymbol{I} - \boldsymbol{n} \cdot \boldsymbol{n}] \cdot \nabla = \nabla - \boldsymbol{n} \frac{\partial}{\partial n}, \tag{3.40}$$

using (3.40) and as both σ and $\boldsymbol{n}$ are only defined at the fluid-fluid interface. The surface force balance is given by

$$\int_S \left[\boldsymbol{n} \cdot \boldsymbol{T} - \boldsymbol{n} \cdot \hat{\boldsymbol{T}} \right] dS = \int_S \left(\gamma \boldsymbol{n} \left(\nabla_s \cdot \boldsymbol{n} \right) - \nabla_s \gamma \right) dS, \tag{3.41}$$

as the surface element is of an arbitrary nature this integrand must vanish identically, so we obtain the interfacial stress balance as

$$\boldsymbol{n} \cdot \boldsymbol{T} - \boldsymbol{n} \cdot \hat{\boldsymbol{T}} = \gamma \boldsymbol{n} \left(\nabla_s \cdot \boldsymbol{n} \right) - \nabla_s \gamma. \tag{3.42}$$

The terms of this equation again have different physical interpretation. $\boldsymbol{n} \cdot \boldsymbol{T}$ and $\boldsymbol{n} \cdot \hat{\boldsymbol{T}}$ represent the forces exerted by each fluid on each other. $\gamma \boldsymbol{n} \left(\nabla_s \cdot \boldsymbol{n} \right)$ is the normal curvature force per unit area and $\nabla_s \gamma$ is the tangential stress due to gradients in the surface tension. At the interface both the normal and tangential stresses must be balanced.

Consider a case where one of the fluid's surface tension is negligible compared to the other such as a liquid-air interface. This gives the following equations for the normal and tangential stress at the interface

$$\boldsymbol{n} \cdot \boldsymbol{T} \cdot \boldsymbol{n} = \gamma \left(\nabla_s \cdot \boldsymbol{n} \right), \tag{3.43}$$

$$\boldsymbol{n} \cdot \boldsymbol{T} \cdot \boldsymbol{t} = \nabla_s \gamma \cdot \boldsymbol{t}. \tag{3.44}$$

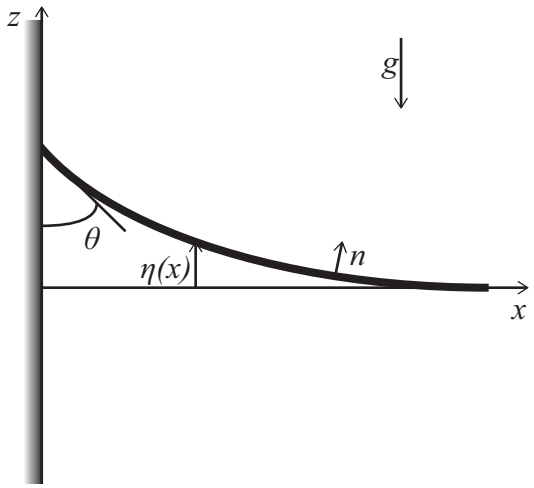

Figure 3.3: Planar meniscus at an air-water interface.

(3.43) and (3.44) therefore represent the boundary conditions for a liquid air interface. This shows that the surface tension depends on the curvature of a surface. The curvature is defined as the degree to which a curve deviates from a straight line, or a curved surface deviates from a plane

3.3.2 Contact Angle

Surface tension arises due to the imbalance in the attractive forces between particles at a fluid-fluid interface. When a third surface, such as a solid surface is introduced a different force is applied to both fluids at the intersection of the fluid-fluid interface and the solid surface. This results in an altering of the resultant surface tension at this intersection. The balance of these forces causes the fluid-fluid interface not to contact the surface at a right angle, which would be the case if there were no surface tension forces. Instead the tangent to the interface will be at an angle, the angle between the tangent to the surface and the tangent to the fluid interface is known as the contact angle.

The contact angle of a fluid can be observed by looking at the meniscus of a air-water interface in a glass. This is a static problem as the fluid does not move in this case, so the forces must balance. Figure (3.3) shows a diagram of this meniscus where θ is the contact angle $\eta(x)$ a function representing the surface shape and $\boldsymbol{n}$ the normal to the surface. In this case only the gravitational ($\rho g z$) and surface tension ($\sigma \nabla \cdot \boldsymbol{n}$) forces apply which must satisfy the Young Laplace equation

$$\rho g z = \gamma \nabla \cdot \boldsymbol{n}. \tag{3.45}$$

Thus the extra force due to the higher fluid must be balanced by the surface tension pressure. The shape of the meniscus is therefore prescribed by the contact angle between the glass and the liquid (θ) and the balance between the hydrostatic and surface tension pressures, equation (3.45). As the density of air compared to water is very small we can make the approximation that $\rho = \rho_w - \rho_a \approx \rho_w$.

For an arbitrary function $f(x, y, z)$ the normal $\boldsymbol{n}$ is defined as $n = \frac{\nabla f}{|\nabla f|}$

In 2D the free-surface can be defined by the expression $z = \eta(x)$ then the arbitrary function can be defined as $f(x, z) = z - \eta(x)$ which vanishes at the surface. The normal to the surface is

$$\boldsymbol{n} = \frac{\nabla f}{|\nabla f|} = \frac{\hat{z} - \eta'(x)x}{(1 + \eta'(x)^2)^{\frac{1}{2}}}. \tag{3.46}$$

An expression for the curvature of the free surface ($\nabla \cdot \hat{n}$) can be derived for Cartesian coordinates by considering a generic surface defined by $z = h(x, y)$. Consider the function $f(x, y, z) = z - h(x, y)$ which vanishes at the surface. The normal to the

surface is defined as

$$\boldsymbol{n} = \frac{\nabla f}{|\nabla f|} = \frac{\hat{z} - h_x\hat{x} - h_y\hat{y}}{\left(1 + h_x^2 + h_y^2\right)^{\frac{1}{2}}}, \tag{3.47}$$

the curvature is the divergence of the normal

$$\nabla \cdot \boldsymbol{n} = \frac{-(h_{xx} + h_{yy} - (h_{xx}h_y^2 + h_{yy}h_x^2) + 2h_x h_y h_{xy}}{\left(1 + h_x^2 + h_y^2\right)^{\frac{3}{2}}}, \tag{3.48}$$

for a two dimensional problem this equation reduces down to

$$\boldsymbol{n} = \frac{\nabla f}{|\nabla f|} = \frac{\hat{z} - h_x\hat{x}}{(1 + h_x^2)^{\frac{1}{2}}}, \tag{3.49}$$

$$\nabla \cdot \boldsymbol{n} = \frac{-h_{xx}}{(1 + h_x^2)^{\frac{3}{2}}}, \tag{3.50}$$

If we assume that the slope of the meniscus remains small then $0 < \eta_x << 1$ so equation (3.50) becomes

$$\nabla \cdot \boldsymbol{n} = \frac{-\eta_{xx}}{(1 + \eta_x^2)^{\frac{3}{2}}} \approx \eta_{xx}, \tag{3.51}$$

substitution into equation (3.45) gives

$$\rho g \eta = \gamma \eta_{xx}. \tag{3.52}$$

As $x \longrightarrow \infty$, $\eta(x) \longrightarrow 0$ the gradient of η at the surface is equal to $-\cot(\theta)$ giving boundary conditions: $\eta(\infty) = 0$ and $\eta_x(0) = -\cot(\theta)$. Solving (3.52) with these

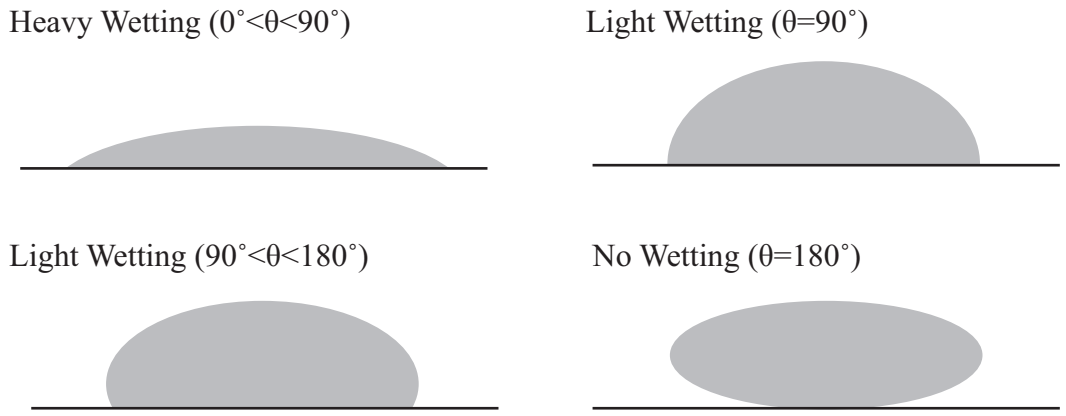

Figure 3.4: Examples of a droplet on surfaces of various wetting.

boundary conditions gives:

$$\eta(x) = l_c \cot(\theta) e^{\frac{-x}{l_c}}, \tag{3.53}$$

where $l_c = \sqrt{\frac{\gamma}{\rho g}}$ is the capillary length. This shows that the meniscus against a solid surface with a contact angle $0° < \theta < 90°$ is an exponential reducing with x.

3.3.3 Wetting and Capillary Force

The same force balance which creates the contact angle against the surface also creates an adhesion or repulsion of the fluid to the surface. This is known as wetting and how wetted a surface is can be described by the contact angle between a surface and a fluid-fluid interface. The contact angle of a surface therefore depends on its wetting some examples can be seen in figure (3.4)

3.4 Viscoelastic Flow

Modelling viscoelastic flow is more complicated than the flow of Newtonian fluids as the viscosity changes with the strain on the fluid. This means that an additional stress tensor is needed to be solved along with the Navier Stokes equations in order to represent this. There are two models in general use for viscoelastic flow, upper convected Maxwell (UCM) and Oldroyd-B models [95]. Here the Oldroyd-B model is considered as this is the most commonly used. The standard Oldroyd-B model is governed by 3 equations [96]

$$\rho \frac{D\boldsymbol{u}}{Dt} = -\nabla p + \nabla \cdot \boldsymbol{S} + \boldsymbol{f}, \tag{3.54}$$

$$\nabla \cdot \boldsymbol{u} = 0, \tag{3.55}$$

$$\boldsymbol{S} + \lambda_1 \boldsymbol{S}^{\nabla} = \eta\left(\dot{\gamma}\right) \boldsymbol{A}_1 + \eta_r \lambda_2 \boldsymbol{A}_1^{\nabla}, \tag{3.56}$$

where $\boldsymbol{u}, p$ and $\boldsymbol{S}$ are the velocity, hydrostatic pressure and the extra stress tensor respectively. $\boldsymbol{f}$ is the body force, $\boldsymbol{A}_1$ the stretching tensor and $\frac{D\boldsymbol{u}}{Dt}$ is the material derivative given by

$$\frac{D\boldsymbol{u}}{Dt} = \frac{\partial \boldsymbol{u}}{\partial t} + \boldsymbol{v} \cdot \nabla \boldsymbol{u}. \tag{3.57}$$

$\boldsymbol{S}^{\nabla}$ is the upper convected time derivative of $\boldsymbol{S}$ and is represented by the identity

$$\boldsymbol{S}^{\nabla} \equiv \frac{\partial}{\partial t}\boldsymbol{S} + \boldsymbol{u} \cdot \nabla \boldsymbol{S} - \left(\nabla \boldsymbol{u}\right)^T \cdot \boldsymbol{S} - \boldsymbol{S} \cdot \left(\nabla \boldsymbol{u}\right), \tag{3.58}$$

and $\dot{\gamma}$ is the magnitude of the rate of deformation given by

$$\dot{\gamma} = \sqrt{\frac{1}{2}\boldsymbol{A}_1 \cdot \boldsymbol{A}_1}. \tag{3.59}$$

The stress tensor can be further defined in terms of its elastic and viscous properties:

$$\boldsymbol{S} = \tau + \eta_s \boldsymbol{A}_1, \eta_s = \beta \eta_r. \tag{3.60}$$

The discretisation of viscoelastic models were initially unstable for high Weisenberg numbers [95], the Weisenberg number, Wi, is a dimensionless number which is the ratio of the relaxation time and the process time. However recent work has increased the stability. Due to the complexities of viscoelastic flow coupled with a free surface model most cases have been 2 dimensional, Tomé *et al.* [97] have looked into a 3D free surface model for viscoelastic flow. They use a marker and cell method on a regular Cartesian mesh with a staggered grid, combined with an Oldroyd-B model for the fluid. The method was generally stable but a fine mesh was required to achieve convergence due to the problems of convergence of the Oldroyd-B model for coarse meshes.

The viscoelastic properties will likely have an effect on the evolution of the surface morphology of the polymer, the main effect will be the speed, and the final polymer shape will be constant irrespective of the viscous forcs. The objectives of this work relate to investigating the final shapes and so for computational simplicity the viscoelastic terms are neglected. However the equations detailed here would allow their addition at a later date.

3.5 Summary

The primary forces controlling the motion of the surface of the polymer are the surface tension and the dielectric forces. These forces are both concentrated around the

interface as they are both caused by the change in material properties at the interface. In addition fluid flow introducing viscous forces.

The dielectric forces arise due to the change in the relative permittivity between the air and the polymer. They are the primary driving force in the initial stages of both processes. The surface tension initially acts to oppose the dielectric forces as a flat surface is a lower energy state. However as the surface morphology changes in EHDIP they act to straighten the sides and curve the bottom of the channels produced. In EFAC due to the additional forces caused by the adhesion to the walls the surface tension becomes dominant and causes the polymer to coat the top of the mask.

Chapter 4

COMPUTATIONAL MODEL AND IMPLEMENTATIONS

4.1 Introduction

As the EFAC and EHDIP process are related process and so the forces involved are the same except for the large capillary forces in the EFAC process. The primary driving force of both methods is the dielectric forces at the interface caused by the electric field. The fundamental difference between the two processes is that in the later stages EFAC process the surface tension force becomes the dominant driving force due to the heavily wetted top mask.

The materials are all assumed to be dielectric so it can also be assumed that there is zero effective current and so magnetic fields may be ignored. There is therefore no transient component to the solution of the electric field and the problem can be considered as a quasi-steady-state electrostatic problem. Combined with the assumption that there is zero free charge in the material bulk reduces the electrostatic problem to

solving Laplace's equation.

As the process is on a micron scale with very large viscosities the Reynold's number can be assumed to be very small (at its largest it is of the order of 10^{-5}) this means that the flow can be assumed to be completely laminar. Thus for solving the flow laminar Navier Stokes may be used.

As there are two fluids to be considered both the air and the polymer a multiphase method is required for the simulation. Due to the rejoining of the fluid in EFAC moving mesh techniques may be discounted as although it is possible to do this with such techniques it requires remeshing so becomes more computationally intensive. Therefore a free surface method was chosen. Specifically a phase-field technique was used in order to track the interface between the molten polymer and the air. The reason for this is that phase field freesurface techniques are more stable at small scales than those of level set or other techniques due to the way the interfacial width and surface tension is calculated, this will be discussed in greater detail later.

4.2 Electrostatics

The primary driving force at the start of the process is due to the electric field applied across the domain. A solution must be obtained for this electric field in order to calculate the interfacial forces. As the two materials that the field passes through can be assumed to have zero free charge in the bulk of the fluid they can be modelled as dielectrics. As discussed in the previous chapter this makes the the solutions simpler. This leaves the Laplace equation to solve for the voltage and the electric field is obtained from the gradient of the voltage. The electrostatics equations do not have a transient dependency. However due to the changing material properties caused by

the evolution of the interface between the polymer and the air the electric field will change over time. However each time step can be considered to be quasi-steady-state and so a series of steady state solutions are used.

4.2.1 Voltage

The voltage is solved by making use of the definition of an electric field ($\boldsymbol{E}$) in terms of the voltage (V)

$$\boldsymbol{E} = -\nabla V, \tag{4.1}$$

combined with the constitutive relationship

$$\boldsymbol{D} = \epsilon_0 \boldsymbol{E} + \boldsymbol{P}, \tag{4.2}$$

and Gauss' Law

$$\nabla \boldsymbol{D} = \rho_f, \tag{4.3}$$

gives a 2nd order partial differential equation for the voltage:

$$-\nabla \cdot (\epsilon_0 \nabla V - \boldsymbol{P}) = \rho_f. \tag{4.4}$$

Under the assumption of zero free charge in the bulk $\rho_f = 0$.

This voltage was then solved by using either a finite volume or finite element technique.

4.2.2 Dielectrics and Electrostatic Forces

The equation for the dielectric and electrostatic forces, which was derived in the previous chapter, produces a volume force. These forces are based on the gradients of variables that are dependent on the free surface variable, namely the permittivity and the density of the materials. These variables are constant within the materials and only change at the interface, thus the gradient only has a value at the interface. Some values of this equation however are known without being derived from the solution (such as $\frac{\partial(\epsilon_r \epsilon_0)}{\partial \rho}$ which as the polymer and air density is assumed to be constant will be $(\epsilon_{poly} - \epsilon_0)/(\rho_{poly} - \rho_{air})$.

For an analytic solution these variables would be applied as a surface force, however as the interface tracking techniques used here treat the two fluids as one continuous fluid with differing material properties there is no boundary to apply a surface force boundary condition to. Therefore the force must be applied at the interface using a different technique. The technique used here is to use a numerical approximation of a Kronecker delta function in order to ensure the force is only acting on the cells which are at the interface between the two materials. A Kronecker delta function is a function that is zero everywhere except at 0 where it is 1.

4.3 Fluid Flow

To solve the flow in the system a Computational Fluid Dynamics (CFD) solver was used in combination with a interface tracking technique. The majority of the work presented here uses a phase-field interface tracking technique as this has the advantage of being more stable when calculating surface tension forces.

4.3.1 Turbulence

The characteristic length scale of the problem is small and the viscosity of the polymer is very high the flow can be assumed to be laminar. This can be shown by using the Reynolds number

$$Re = \frac{\rho \bar{u} L_c}{\mu}, \tag{4.5}$$

where ρ is the density, $\bar{u}$ average velocity, L_c the characteristic length scale and μ the dynamic viscosity. The largest characteristic length scale is 300 μm the density of the polymer is approximately 1000 kg/m^3 and the typical polymer viscosities are between 1 and 3.5 Pa $\cdot$ s. For turbulent flows the velocity would therefore need to be of the order of 1×10^5 m/s, which is unrealistic for this application. This means that a turbulence model is not required.

4.3.2 Navier Stokes

The Navier-Stokes equations are all that is required to model laminar flow of a single fluid. These have been discussed in the theory section. A standard discretisation was used either using the finite element method or finite volume method depending on whether PHYSICA[98] or COMSOL Multiphysics [99] was used. Both software packages use a pressure correction method.

4.3.3 Multiphase Methods

Various methods were initially considered for modelling the free-surface of the fluid-fluid interface. These were a interface tracking technique moving mesh, and two interface capturing techniques level set and phase field techniques.

A moving mesh technique was considered but this was discounted as unsuitable as though it would have worked for EHDIP cases for EFAC where the polymer joins together at the top of the mask it would have been unsuitable as this would require the polymer to intersect where it met in the middle of the top mask. This is computationally intensive in moving mesh techniques as it would require remeshing in order to achieve this joining.

Consequently an alternative interface capturing technique was required on a fixed mesh. Two options for capturing the interface were then considered; a level set method and a phase field method. They both solve for a freesurface variable in order to track the interface. The primary difference between the two is that while level set methods use an artificial function for the interface thickness the phase field method uses a function based on the surface energy between the two fluids. Both methods have their advantages and disadvantages and they will be discussed in detail here.

4.3.3.1 Level Set Method

A level set method [100] is a method which models the interface between two immiscible fluids by using a variable ϕ to represent which fluid is present. In traditional level set methods the variable ϕ is defined to be a signed distance function of the form

$$|\phi(\boldsymbol{x})| = d(\boldsymbol{x}) = \overset{min}{\boldsymbol{x}_I \in I} \left(|\boldsymbol{x} - \boldsymbol{x}_I|\right). \tag{4.6}$$

To apply material properties to the different fluids a Heaviside function giving

$$H_s(\phi) = 0, \phi < 0, \tag{4.7}$$

$$H(\phi) = 1, \phi > 0. \tag{4.8}$$

This function has a discontinuity at the interface. For computational stability a smoothing function is used to smear the Heaviside function, an example of such a smoothing function is

$$H_{sm}(\phi) = \begin{cases} 0 & \phi < -\epsilon, \\ \frac{1}{2} + \frac{\phi}{2\epsilon} + \frac{1}{2\pi}\sin\left(\frac{\pi\phi}{\epsilon}\right) & -\epsilon \leq \phi \leq \epsilon, \\ 1 & \phi > \epsilon. \end{cases} \tag{4.9}$$

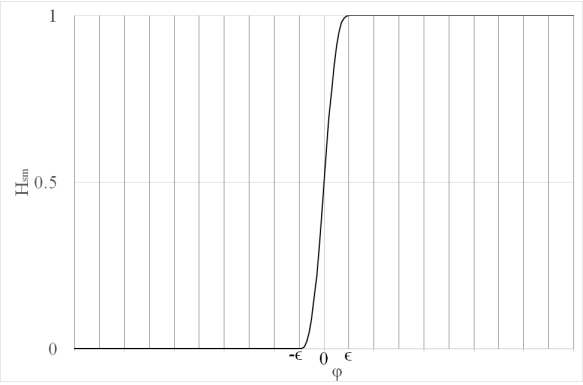

Figure 4.1: A Heaviside function.

a plot of this function can be seen in figure (4.1). However, more recent level set methods make use of a different free surface variable defined as

$$\tilde{\phi}(\boldsymbol{x}) = H_{sm}(\phi(\boldsymbol{x})). \tag{4.10}$$

This incorporates the smoothing Heaviside function so the material properties can be

derived directly from it. The normal and curvature of the interface can be obtained by taking the gradient of ϕ and the gradient of the normal such that

$$\hat{\boldsymbol{n}} = \frac{\nabla\phi}{|\nabla\phi|}, \tag{4.11}$$

$$\kappa = -\nabla \cdot \hat{\boldsymbol{n}} = -\nabla \cdot \frac{\nabla\phi}{|\nabla\phi|}. \tag{4.12}$$

F

The advection of the free surface variable then needs to be calculated so that the surface moves. To do this for incompressible flow the solution of the following differential equation is needed:

$$\phi_t + \nabla \cdot (\phi \boldsymbol{u}) = 0. \tag{4.13}$$

A numerical method can then be used to discretise this equation and obtain an approximate solution. These equations form the basis of solving free surface evolution using the level set method.

4.3.3.2 Phase Field Method

A diffuse interface phase field method is essentially an extension of the level set method, where instead of using an arbitrary artificial smoothing function on the free surface variable ϕ, the surface energy of the two materials is used to derive a function which smooths the interface. The primary reason for this is to increase the stability of surface tension calculations on small scales. Liu *et al.* [33] published this method, however there was an error in the equation published, the following derives the equations from

first principles to obtain the correct equations to solve.

The derivation of the model starts with the Lagrangian ($L_{rg} = K - \Omega$) where K and Ω are the kinetic and potential energies. From the principle least action the action integral ($I = \int_{t_1}^{t_2} L_{rg} dt$) must be stationary to the first order when the "path" of the integral is varied. This leads to a momentum equation, based on the free energies of the system.

For Newtonian fluids the primary free energy is the mixing energy of the system. This mixing energy is due to the diffuse interface giving the interface between the two fluids a small but finite thickness. In order to calculate this we introduce a free surface variable ϕ which has a value between -1 and 1, such that the concentration of each fluid is $(1+\phi)/2)$ and $(1-\phi)/2$. Thus if the mixing energy density ω_{mix} is represented as a Cahn-Hilliard equation

$$\omega_{mix}(\phi, \nabla(\phi)) = \frac{1}{2}\lambda|\nabla\phi|^2 + \omega_0(\phi). \tag{4.14}$$

Assuming that ω_0 is a double well potential

$$f_0 = \frac{\lambda_{st}}{4\epsilon_{st}^2}\left(\phi^2 - 1\right)^2, \tag{4.15}$$

where f_0 is the total free energy. The bulk energy ω_0 is minimised when there is a pure separation of components (i.e. a sharp infinitesimal interface). The first term then is a phillic effect being in its lowest energy state when the fluids are completely mixed. This gives two variables which control the interface, λ_{st} the magnitude of the mixing energy and ϵ_{st} a capillary width which represents the thickness of the interface.

This mixing energy represents the interactions between the two phases and includes the concept of surface tension. It can be shown that the surface tension variable σ can

be written in terms of λ_{st} ϵ_{st}. Consider a one dimensional interface and assume the mixing energy is equal to the traditional surface energy

$$\sigma = \lambda_{st} \int_{-\infty}^{+\infty} \left[\frac{1}{2} \left(\frac{d\phi}{dx} \right)^2 + f_0(\phi) \right] dx. \tag{4.16}$$

Then by assuming that the diffuse interface is at equilibrium, it has zero chemical potential

$$\frac{\delta f_{mix}}{\delta \phi} = \lambda_{st} \left[-\frac{d^2\phi}{dx^2} + f_0'(\phi) \right] = 0. \tag{4.17}$$

Given that $f_0(\pm\infty) = 0$ and that $\frac{d\phi}{dx}\big|_x = \pm\infty = 0$, integrating this equation gives

$$\frac{1}{2} \left(\frac{d\phi}{dx} \right)^2 = f_0(\phi), \tag{4.18}$$

showing that the two terms are equal implying that they have equal contributions to the free energy. (4.18) can be solved using the boundary condition $\phi(0) = 0$, this gives the equilibrium profile for $\phi(x)$

$$\phi(x) = \tanh \left(\frac{x}{\sqrt{2}\epsilon_{st}} \right). \tag{4.19}$$

Substituting (4.19) into (4.16) gives

$$\sigma = \frac{2\sqrt{2}\lambda}{3\epsilon_{st}}. \tag{4.20}$$

The governing equations then can be derived from the least action principle and are quoted in [33] however there is a misprint in that paper so they are redirived here to obtain the correct equation. Using the general Navier Stokes formulation of the

momentum equations given by

$$\nabla \cdot \boldsymbol{u} = 0, \tag{4.21}$$

$$\rho \left(\frac{\partial \boldsymbol{u}}{\partial t} + \boldsymbol{u} \cdot \nabla \boldsymbol{u} \right) = -\nabla p + \nabla \cdot \boldsymbol{T} + f. \tag{4.22}$$

Based on (4.14), assuming the chemical potential can be defined as $\frac{\delta \Omega}{\delta \phi}$ and that the mass flux is proportional to the gradient of the chemical potential, the evolution equation for ϕ can be obtained

$$\frac{\partial \phi}{\partial t} + \boldsymbol{u} \cdot \nabla \phi = \nabla \cdot \left[\gamma_1 \nabla \left(\frac{\delta \Omega}{\delta \phi} \right) \right], \tag{4.23}$$

here γ_1 is the mobility and is assumed to be constant. The right hand side is the diffusion term, using the sharp interface limit the interface is solely driven by advection. Neglecting the bulk free energy and retaining only the mixing energy gives

$$\frac{\partial \phi}{\partial t} + \boldsymbol{u} \cdot \nabla \phi = \gamma_1 \lambda \nabla^2 \left[-\nabla^2 \phi + \frac{\phi(\phi^2 - 1)}{\epsilon_{st}} \right]. \tag{4.24}$$

The boundary conditions are

$$\nabla \left(\frac{\delta \Omega_{mix}}{\delta \phi} \right) \cdot \boldsymbol{n} = 0, \tag{4.25}$$

$$\frac{\partial \omega_{mix}}{\partial \left(\nabla \phi \right)} \cdot \boldsymbol{n} = 0, \tag{4.26}$$

where $\boldsymbol{n}$ is the normal to the boundary. Using (4.16) and (4.17), (4.25) and (4.26)

reduce to

$$\frac{\partial \phi}{\partial m} = 0, \tag{4.27}$$

$$\frac{\partial}{\partial m}\left(\nabla^2 \phi\right) = 0. \tag{4.28}$$

In order to use these methods equation (4.24) is discretised semi-implicitly in time

$$\begin{aligned}&\frac{\phi^{n+1} - \phi^n}{\Delta t} + (\boldsymbol{u} \cdot \nabla \phi)^n \\ &= \gamma_1 \lambda_{st} \nabla^2 \left[\left(-\nabla^2 \phi + \frac{s\phi}{\epsilon_{st}^2} \right)^{n+1} + \left(\frac{\left(\phi^2 - 1 - s\right)\phi}{\epsilon_{st}^2} \right)^n \right],\end{aligned} \tag{4.29}$$

(4.29) can then be rearranged to form two Helmholtz equations, to do this firstly the equation needs to be rearranged to put the $n+1^{th}$ time-step and the n^{th} time-step on opposite sides:

$$\begin{aligned}&\left[-\frac{\phi}{\Delta t} + \boldsymbol{u} \cdot \nabla \phi - \gamma_1 \lambda_{st} \nabla^2 \left(\frac{\left(\phi^2 - 1 - s\right)\phi}{\epsilon_{st}^2} \right) \right]^n \\ &\qquad = \left[-\frac{\phi}{\Delta t} + \gamma_1 \lambda \nabla^2 \left(-\nabla^2 \phi + \frac{s\phi}{\epsilon_{st}^2} \right) \right]^{n+1},\end{aligned} \tag{4.30}$$

where s is a parameter governing how implicit the equation is. Dividing both sides of (4.30) gives

$$\begin{aligned}&\frac{1}{\gamma_1 \lambda} \left[-\frac{\phi}{\Delta t} + \boldsymbol{u} \cdot \nabla \phi - \gamma_1 \lambda_{st} \nabla^2 \left(\frac{\left(\phi^2 - 1 - s\right)\phi}{\epsilon_{st}^2} \right) \right]^n \\ &\qquad = \left[-\frac{\phi}{\gamma_1 \lambda_{st} \Delta t} + \nabla^2 \left(-\nabla^2 \phi + \frac{s\phi}{\epsilon_{st}^2} \right) \right]^{n+1}.\end{aligned} \tag{4.31}$$

Defining a new variable ψ such that

$$-\psi = \left[-\alpha\phi - \nabla^2\phi\right]^{n+1}, \tag{4.32}$$

where α is a constant and rerranging gives

$$\left[-\nabla^2\phi\right]^{n+1} = -\psi + \left[\alpha\phi\right]^{n+1}. \tag{4.33}$$

Substituting $\left[-\nabla^2\phi\right]^{n+1}$ from (4.33) into (4.31) gives

$$\begin{aligned}\frac{1}{\gamma_1\lambda}\left[-\frac{\phi}{\Delta t} + \boldsymbol{u}\cdot\nabla\phi - \gamma_1\lambda_{st}\nabla^2\left(\frac{\left(\phi^2-1-s\right)\phi}{\epsilon_{st}^2}\right)\right]^n \\ = \left[-\frac{\phi}{\gamma_1\lambda_{st}\Delta t} + \nabla^2\left(-\psi + \left(\alpha + \frac{s}{\epsilon_{st}^2}\right)\phi\right)\right]^{n+1}.\end{aligned} \tag{4.34}$$

Separating terms of the ∇^2 on the RHS

$$\begin{aligned}\frac{1}{\gamma_1\lambda}\left[-\frac{\phi}{\Delta t} + \boldsymbol{u}\cdot\nabla\phi - \gamma_1\lambda\nabla^2\left(\frac{\left(\phi^2-1-s\right)\phi}{\epsilon_{st}^2}\right)\right]^n \\ = \left[\frac{\phi}{\gamma_1\lambda_{st}\Delta t} + \left(\alpha + \frac{s}{\epsilon_{st}^2}\right)\nabla^2\phi - \nabla^2\psi\right]^{n+1}.\end{aligned} \tag{4.35}$$

and substituting $\left[-\nabla^2\phi\right]^{n+1}$ again

$$\frac{1}{\gamma_1\lambda}\left[-\frac{\phi}{\Delta t}+\boldsymbol{u}\cdot\nabla\phi-\gamma_1\lambda\nabla^2\left(\frac{\left(\phi^2-1-s\right)\phi}{\epsilon_{st}^2}\right)\right]^n$$
$$=\left[-\frac{\phi}{\gamma_1\lambda_{st}\Delta t}+\left(\alpha+\frac{s}{\epsilon_{st}^2}\right)(\psi-\alpha\phi)-\nabla^2\psi\right]^{n+1}, \tag{4.36}$$

multiplying out brackets of (4.36) gives

$$\frac{1}{\gamma_1\lambda}\left[-\frac{\phi}{\Delta t}+\boldsymbol{u}\cdot\nabla\phi-\gamma_1\lambda\nabla^2\left(\frac{\left(\phi^2-1-s\right)\phi}{\epsilon_{st}^2}\right)\right]^n$$
$$=\left[-\frac{\phi}{\gamma_1\lambda_{st}\Delta t}-\left(\alpha+\frac{s}{\epsilon_{st}^2}\right)\alpha\phi+\left(\alpha+\frac{s}{\epsilon_{st}^2}\right)\psi-\nabla^2\psi\right]^{n+1}, \tag{4.37}$$

and collecting terms in (4.37) gives

$$\frac{1}{\gamma_1\lambda}\left[-\frac{\phi}{\Delta t}+\boldsymbol{u}\cdot\nabla\phi-\gamma_1\lambda\nabla^2\left(\frac{\left(\phi^2-1-s\right)\phi}{\epsilon_{st}^2}\right)\right]^n$$
$$=\left(-\frac{1}{\gamma_1\lambda_{st}\Delta t}-\alpha^2+\frac{\alpha s}{\epsilon_{st}^2}\right)\phi^{n+1}+\left(\alpha+\frac{s}{\epsilon_{st}^2}\right)\psi-\nabla^2\psi. \tag{4.38}$$

α is chosen by setting the first term on the RHS of (4.38) to zero such that

$$\alpha^2-\frac{s}{\epsilon_{st}^2}+\frac{1}{\gamma_1\lambda_{st}\Delta t}=0, \tag{4.39}$$

using the quadratic equation

$$\alpha = \frac{-\frac{s}{\epsilon_{st}^2} \pm \sqrt{\frac{s^2}{\epsilon_{st}^4} - \frac{4}{\gamma_1 \lambda_{st} \Delta t}}}{2} \tag{4.40}$$

$$\Rightarrow \alpha = -\frac{s}{2\epsilon_{st}^2} \left(1 \pm \sqrt{1 - \frac{4\epsilon_{st}^4}{\gamma_1 \lambda_{st} s^2 \Delta t}} \right), \tag{4.41}$$

as $\alpha^2 - \frac{s}{\epsilon_{st}^2} + \frac{1}{\gamma_1 \lambda_{st} \Delta t} = 0$ this can be substituted into equation (4.38)

$$\frac{1}{\gamma_1 \lambda_{st}} \left[-\frac{\phi}{\Delta t} + \boldsymbol{u} \cdot \nabla \phi - \gamma_1 \lambda_{st} \nabla^2 \left(\frac{\left(\phi^2 - 1 - s\right) \phi}{\epsilon_{st}^2} \right) \right]^n = \left(\alpha + \frac{s}{\epsilon_{st}^2} \right) \psi - \nabla^2 \psi. \tag{4.42}$$

Thus the semi-implicit time discretised equations are

$$\frac{1}{\gamma_1 \lambda_{st}} \left[-\frac{\phi}{\Delta t} + \boldsymbol{u} \cdot \nabla \phi - \gamma_1 \lambda_{st} \nabla^2 \left(\frac{\left(\phi^2 - 1 - s\right) \phi}{\epsilon_{st}^2} \right) \right]^n = \left(\alpha + \frac{s}{\epsilon_{st}^2} \right) \psi - \nabla^2 \psi, \tag{4.43}$$

$$\left[-\alpha \phi - \nabla^2 \phi \right]^{n+1} = -\psi. \tag{4.44}$$

There are limits on the variables as for there to be a real α, it is required that $s \geq 2\epsilon_{st}^2 / \sqrt{\gamma_1 \lambda_{st} \Delta t}$.

Both (4.43) and (4.44) are in the form of Helmholtz equations so can be solved using a fast Fourier transform, or by taking them as diffusion equation and using the related spatial discretisations.

	Level Set	Phase Field
Advantages	established method only one equation	surface energy known implicitly viscoelastic flow simpler to implement
Disadvantages	unstable for small scales curvature needs to be calculated	two equations need to be solved

Table 4.1: Summary of the advantages and disadvantages of the level set and phase field interface capturing techniques.

4.3.3.3 Method Selection

The two potential methods, level set and phase field, discussed previously both have advantages and disadvantages for modelling the interface between two immiscible fluids, these are summarised in table (4.1).

The primary advantage of the level set method is that it is a more established method for interface capturing, in addition only one equation needs to be solved to track the interface. The disadvantage is that the surface tension is calculated separately from the interface capturing from the curvature. As the curvature is calculated from the gradient of the free surface variable, in small scale problems this can cause divergence as there are very large curvatures due to the small scales meaning that the mesh density must be very fine. This can cause divergence of the numerical method as the small mesh size mean that errors in the calculation in the curvature tend to create extremely large forces which are not physical but due to numerical error. This then effects the stability of the solution.

The diffuse interface phase field method on the other hand has an expression related to the surface energy in one of the governing equations (4.44). More details on this are

in the next section. The surface energy and the surface tension force can be obtained from this equation. This avoids the problems with divergence caused by the numerical methods being used to calculate the curvature in level set methods. Conversely this does give an extra partial differential equation to solve compared to the level set method, thus increasing the simulation time.

An additional advantage of the diffuse interface phase field method is that it was developed for use in modelling the interface between Newtonian and non-Newtonian fluids. Hence the elastic properties of a viscoelastic fluid can be included in the phase field calculations, this gives a more stable solution for multiphase viscoelastic flow. In the initial model presented here, the viscoelastic flow has been neglected, however the use of a phase field method makes the addition of these forces later a simpler task.

All of these advantages and disadvantages led to the diffuse interface phase field method being selected to model the free surface, the increased stability at small scales and the potential of adding viscoelastic forces later meant that the extra overheads of solving an extra partial differential equation were considered to be acceptable.

4.4 Implementation

Implementing the model started initially by trying to model the EHDIP process using PHYSICA version 3g, which is a multiphysics simulation software developed initially at the University of Greenwich. The early implementation started firstly by adding an electrostatics solver into PHYSICA in order to solve the voltage profile and so obtain the electric field. The two different surface capturing techniques available in PHYSICA, a level set method and a fluid marker method, were then used to simulate the flow of the fluids. However unfortunately this ran into difficulties as the surface

tension calculations for these methods proved to be unstable.

The decision was then made to move into COMSOL Multiphysics 4.0 in order to use the phase field method. This had the advantage that there was already an electrostatics solver and a phase field multiphase flow technique.

4.4.1 PHYSICA *vs.* COMSOL Multiphysics

PHYSICA is a multiphysics solver initially developed at the University of Greenwich. It is primarily a finite volume code and can be used to solve multiphysics problems using finite volume solvers. It is primarily a research code rather than a commercial software package, though commercial licenses of the software are sold. The primary advantages of PHYSICA is that large amounts of the source code can be modified in order to solve different multiphysics problems. The primary disadvantage is that because it is a research code it can be unstable in some situations.

PHYSICA has modules for flow, interface capturing, structural mechanics, magnetohydrodynamics, combustion and several other problems. It does not however have an electrostatics solver which would be needed for this project. It also lacks a phase-field interface capturing technique.

COMSOL is a commercial multiphysics code that is based around a finite element solver. It was initially based on a matlab extension called PDETool which was a matlab based finite element solver for solving PDEs. It has since been rewritten however and is now a stand alone product, with many modules to model various physics, these modules can then be combined to produce multiphysics simulations. COMSOL includes modules for several multiphysics cases including, fluid flow, electrostatics, fluid structure interaction, chemical reaction engineering, plasma physics and structural

mechanics. Here the electrostatics and fluid flow modules were particularly important as they allow the problem presented here to be solved without modification of the code.

Work was initially undertaken in PHYSICA as the author had more experience of this software and as the source code was available more there was potential for more control of the software. However after implementing an electrostatics solver it was found that the level set interface capturing techniques in PHYSICA were unstable when calculating surface tension forces at such a small scale.

It was therefore decided that implementation of the model should be transfered into COMSOL multiphysics which as it has a phase-field interface tracing method which is more stable than the level set method in PHYSICA enabled

4.4.2 Finite Element and Finite Volume Techniques

One of the reasons that PHYSICA was originally selected to implement the computational model was that it is a finite volume solver, whereas COMSOL is a finite element solver. Traditionally finite volume solvers[101] have been used for fluid dynamics problems whereas finite element solvers have not. The primary reason for this is that though finite element solvers can be used to solve fluid dynamics problems, they are generally slower than finite volume solvers to solve the same problem[102]. To understand why this is the case the differences between the two methods needs to be set out.

The finite element method is based on weighted residuals. It uses the weak formulation of a PDE to discretise an equation using a technique such as the Galerkin method. The weak formulation is based on the integral of the residual of a PDE. It is called

the weak formulation as while the strong formulations solution will also be a solution to the weak formulation the converse is not true. Taking the weak formulation the equations can be discretised. The discretisation consists of taking piecewise functions, usually linear functions but polynomial functions can also be used. These functions are defined for each element and are an approximation of the overall linear function produced from the weak formulation. These are known as the basis functions. These functions can then be converted into matrix form in order to form a sparse matrix which can then be solved either by using direct solvers or iterative solvers.

The finite volume technique however is based on surface integrals around a fixed volume cell. The volume integral inside the cell is converted into a surface integral by use of the divergence theorem. This gives each face of a cell a flux which. As the flux leaving each cell must be equal to that entering its neighbours this method is therefore conservative. This allows equations to be obtained for each cell based on the fluxes at the faces of the cell. These equations can be then combined into matrix form giving a matrix which can again be solved by either using direct or iterative solvers.

The primary advantages that the finite volume method has over the finite element method is that it is inherently conservative. The finite element method is not but it can be made so. The finite volume method is also less memory intensive than the finite element method and is often quicker to solve as the matrices it produces are smaller. However the finite element method allows for more degrees of freedom than the finite volume method and so can produce more accurate solutions.

4.4.3 PHYSICA

Initially work was done in PHYSICA version 3g to attempt to solve the problem this involved firstly implementing a finite volume electrostatics solver within the PHYSICA environment. This was achieved using the user routine to solve a new scalar variable for the electric potential, the spatial gradient of this voltage was then found in order to calculate the electric field. This electric field was then used to calculate the force at the fluid-fluid interface. The force was then applied by using a volume source.

There were several difficulties in this implementation, the first of which is that in calculating the interfacial forces the gradient of the electric field needed to be found. To do this a numerical approximation of the gradient of the voltage was needed to obtain the electric field. The force could then be calculated by using the gradient of this electric field. The main issue with this is that in reality there is a discontinuity in the electric field, due to the polarisation in the dielectric liquid polymer. This discontinuity on a discretised grid is obviously smeared along the interface, this allows a gradient of the electric field too be obtained, thus giving a volume force rather than a stress tensor. However there are possibilities for errors to be brought in at this stage as the electric field gradient, other than at the interface will be small, thus slight errors in its calculations can cause large errors in calculating the interfacial forces. This problem was solved by only allowing the calculated force to be applied to the cells either side of the interface.

The other issue is one that was discussed earlier when discussing the reasons for choosing a phase field method to model the freesurface. As PHYSICA only has level set and fluid marker method, the surface tension calculation methods for both of these implementations proved to be unstable for the small scales being considered. This is

due to numerical errors in the calculation of the curvatures, these numerical errors caused large forces to be incorrectly applied at the interface which caused the fluid solver to diverge.

In addition to the convergence problems with surface tension, the meshes needed for the more complex geometries of EFAC compared to EHDIP would be harder to generate in PHYSICA. The combination of these issues led the development of the model to a different path using COMSOL Multiphysics 4.0.

4.4.3.1 Preliminary Modelling in PHYSICA version 3g

Early attempts to model the process were undertaken in PHYSCIA 3g, this implementation was abandoned after the calculation of the surface tension proved unstable, thus these results exclude surface tension and just show the effect of the dielectric force on the surface of a fluid.

Figure (4.2) shows the voltage distribution from the electric field solver for a top electrode which has a high voltage in the centre. These results are early test cases and are using the level set method within PHYSICA.

Figure (4.3) shows the shape of the surface for this voltage distribution, due to the lack of surface tension in this early model the surface has a tendency to form "spikes".

Figure (4.4) shows a similar case but with two high points in the voltage at the top mask, as can be seen two growth occur rather than just the one, and again the "spikes" are there.

This early model proved problematic due to the lack of surface tension calculations which result in unrealistic results, however they did provide early insight into the physics behind the EDHIP process. They showed that the polymer melt will rise up under high areas of electric field when a non-uniform voltage is applied.

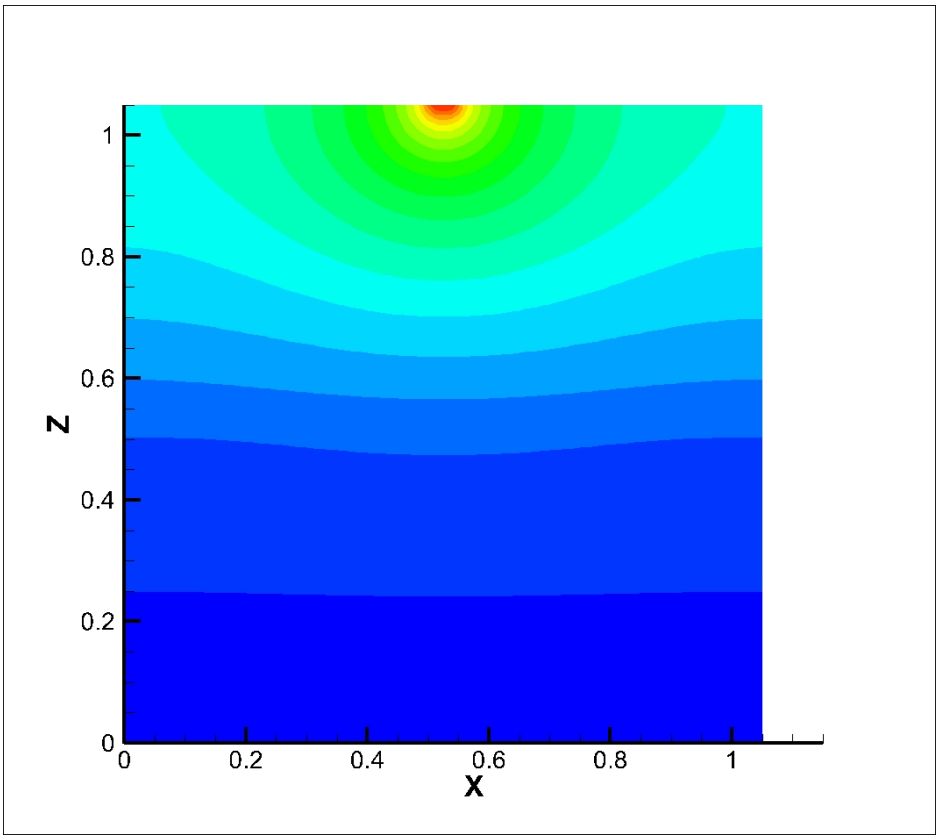

Figure 4.2: Voltage distribution for a mask with one high voltage point.

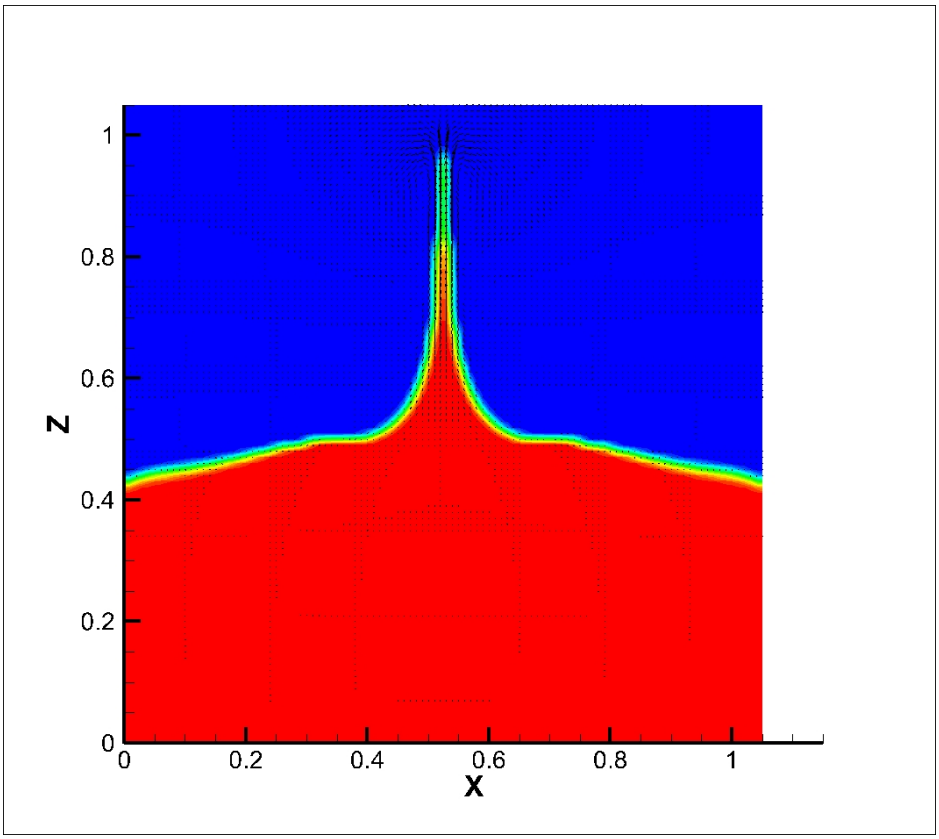

Figure 4.3: Free surface for a mask with one high voltage point.

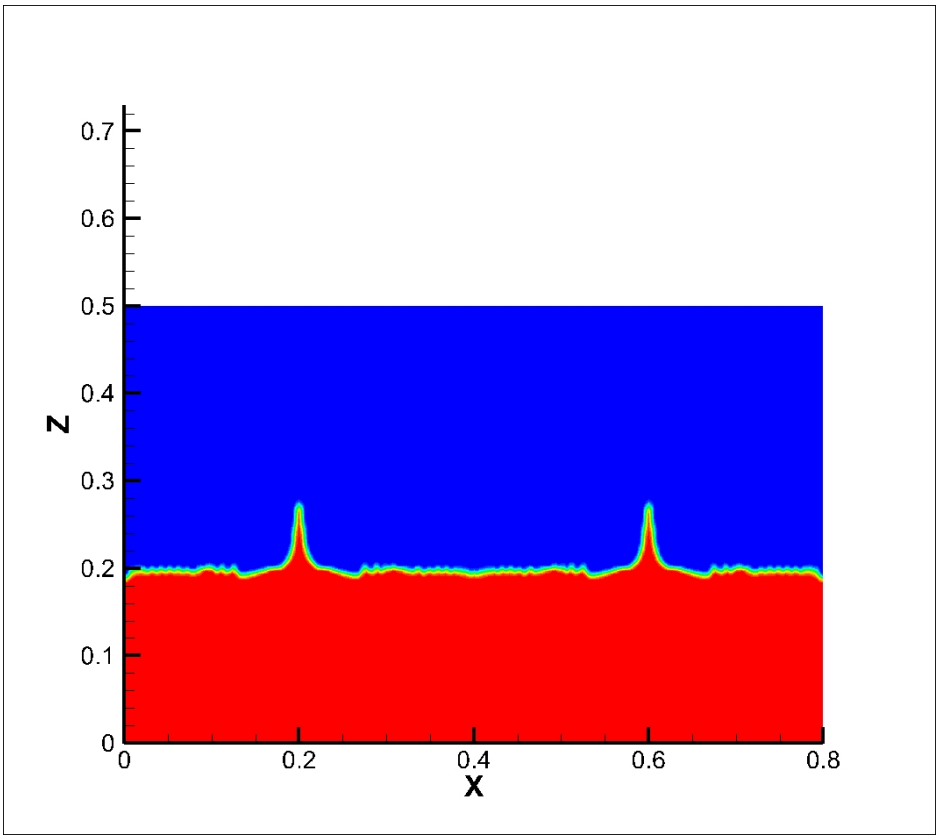

Figure 4.4: Free surface for a mask with two high voltage points.

The model was shelved while work began in using COMSOL Multiphysics to implement a similar model, as this new model dud not have the drawbacks of the PHYSICA model it was used instead.

4.4.4 COMSOL Multiphysics

The move to using COMSOL Multiphysics in order to simulate the process was done due to the issues with the stability of PHYSICA's surface tension calculations. There were several benefits in this but also a few disadvantages.

The benefits of using COMSOL were that the model was much simpler to implement compared to PHYSICA, firstly the electrostatics and phase field modules were already in place and it only required the inputting of the variables to calculate the interfacial force due to the dielectric of the two materials. This was not such an easy task at it seemed it would be at first.

Firstly a method to only apply the force at the interface was needed. COMSOL does not need a Kronecker delta function in order to calculate any of the modules used (it does calculate one for the level set interface), thus an approximation of a Dirac delta function was first calculated and this was then normalised to a Kronecker delta and this was then used to restrict the volume force to the interface. The resulting Kronecker delta is two cells thick at the interface.

Another issue with the calculation of the volume force at the interface was that COMSOL does not calculate derived variables whilst solving, this was a problem as the electric field was a derived variable as it is calculated as the gradient of the voltage. COMSOL is able to calculate the derivatives of variables so the x and y components of the electric field could be obtained by taking the derivatives in the respective directions.

COMSOL's main problem has been simulation time, this is mostly due to the small time-steps that COSMOL uses. The reasons for these small time-steps are due to convergence. COMSOL has several automatic time-stepping routines that reduce the time-step if convergence is not achieved. This is a problem as the time-steps

needed to achieve convergence for some of the time-steps in the cases run are of the order of 10^{-6} times the output time-steps. Each time-step solves quite quickly in 2D as COMSOL uses parallel direct solvers rather than iterative solvers in order to solve each time-step, so only the coupling of the models needs to be iterated. However, as they need the entire matrix loaded into memory to be able to invert it, the number of mesh elements needed for a 3D simulation would be too large to use these methods this meant that the solutions are currently restricted to two dimensions. Due to these small time-steps initially the model took 3 days to run for the meshes presented here. However due to optimisations made during the project and also using newer hardware meant that the simulation time was reduced to approximately 4 hours.

4.5 Summary

In implementing the models presented here two different aspects of the physics needed to be solved the electrostatics and the multiphase fluid flow. These were solved in COMSOL Multiphysics using a finite element solver. The multiphase flow was solved using the phase field model as these models are more stable for small scales than level set techniques.

Chapter 5

RESULTS

5.1 Introduction

This chapter considers the results from the COMSOL models for both the EHDIP and EFAC processes. Firstly some validation cases are considered and compared to the experimental results available, where they show a good agreement. After the validation cases various mask types are considered to show the capabilities of the process. For EHDIP a simple right angled "square" mask is considered as well as a curved "double mask" which could be used in order to produce lenses. For the EFAC cases 3 different single masks are considered, one with a semi-circular top, one with an angled top, and one with a square top. The angled and square top cases have a rounded corner added to enable the top surface to be fully coated. The effect of not having this rounding is discussed further in the following chapter. The "double masked" cases for these show a "hexagonal" mask and a curved mask which could be used to produced stackable channels. The masks themselves are outside of the modelling domain and so are not included in the results presented, however the shape of the masks results in the shape

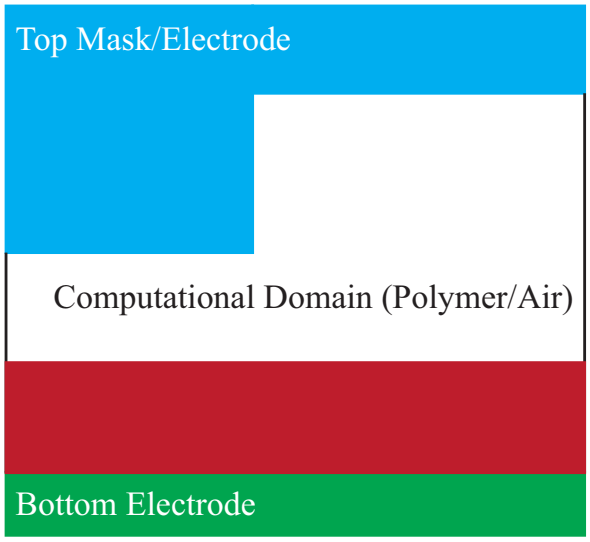

Figure 5.1: Location of masks outside the computational domain.

	Air	Polymer
Relative permittivity	1	2.5
Density	1.204 kg/m^3	1000 kg/m^3
Dynamic viscosity	$1.814 \times 10^{-}5$ Pa$\cdot$s	1 Pa$\cdot$s
Surface tension coefficient	$20 \times 10^{-}3$ N/m	$20 \times 10^{-}3$

Table 5.1: Material properties.

of the outside of the domain. A diagram of an example is shown in figure (5.1).

The same material properties were used for all cases unless otherwise specified and can be seen in table (5.1).

5.2 Validation

Due to the nature of the project it has been difficult to undertake the validation and verification of the modelling work. The limited experimental data for EHDIP and EFAC cases available is qualitative rather than quantitative. This is because the majority of the experimental results published consist of pictures of the channels and

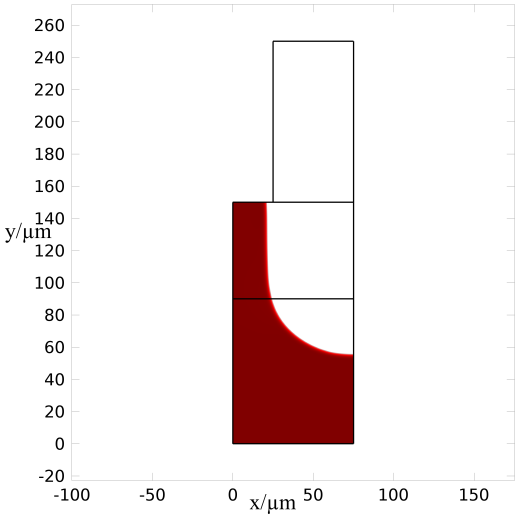

(a) Model Results

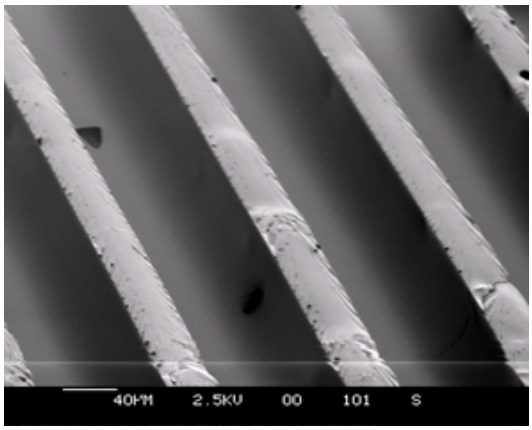

(b) Experimental Results (Images Courtesy of Chinese Key State Laboratory of Applied Optics)

Figure 5.2: Comparison of EHDIP model results with an image of channels produced experimentally.

capsules producible by this method. For validation therefore only qualitative validation is possible showing that the channels produced by the process experimentally match up to the channels produced by the model. Similarly though attempts were made to derive one the complexities of the physics have proven too difficult to find an analytic solution to the problem presented here. So verification of the numerics for the entire model has not been possible.

5.2.1 Electrohydrodynamic Induced Patterning

The validation case for Electrohydrodynamic Induced Patterning looks at a high aspect ratio channel in a high electric field. This channel uses a square mask with a high voltage, spin coated polymer and a high aspect ratio mask, high aspect ratio here referring to a larger depth to the mask than distance between the grooves.

Figure (5.2) shows a comparison of the results from this model with channels

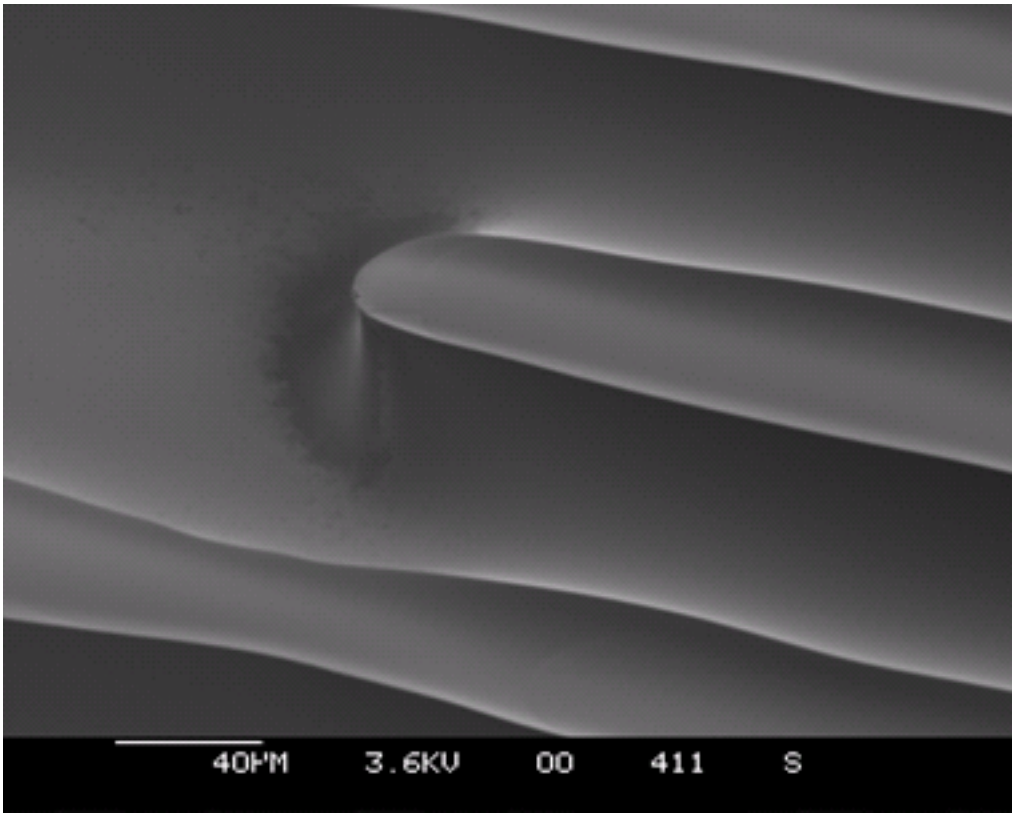

Figure 5.3: Experimental Results for channels produced using EHDIP(Images Courtesy of Chinese Key State Laboratory of Applied Optics).

produced experimentally. Unfortunately there are no measurements available for these channels and they are not quite the same dimensions. However as can be seen the channels have the same flat top (where the channels touch the mask so this area is rough) then the same straight sides but curved bottom as seen in the model. Similar channels can be seen in figure (5.3) along with the mask used to produce these channels. As can be seen again the channels have the same straight sides and curved base as the model suggests.

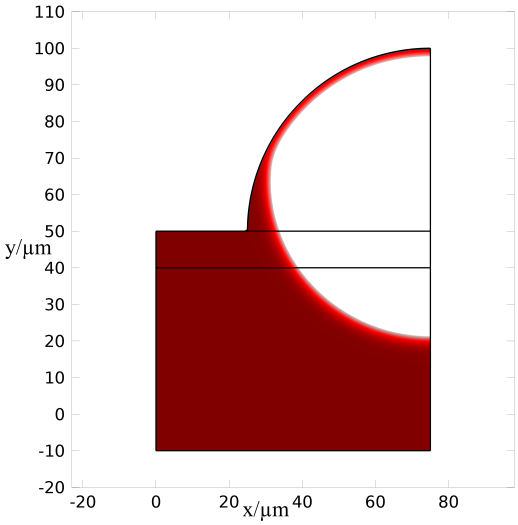

(a) Model results

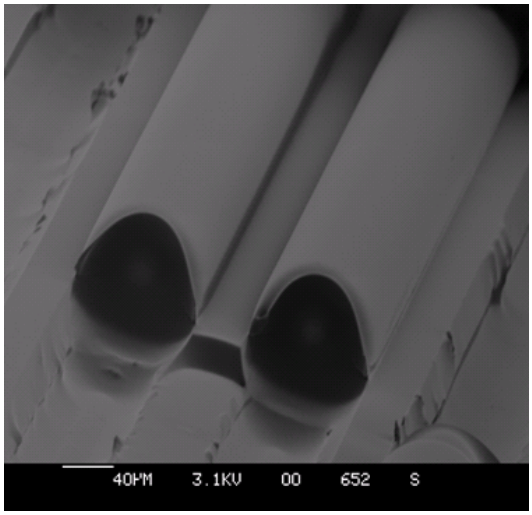

(b) Experimental results(Images Courtesy of Chinese Key State Laboratory of Applied Optics)

Figure 5.4: Comparison of EFAC model results with an image of channels produced experimentally.

5.2.2 Electric Field Assisted Capillarity

Again for the validation of EFAC the model can only be done qualitatively as there is no experimental results available other than the pictures shown here. The first aspect of the validation looks at a curved mask. The modelling and experimental results for such channels can be seen in figure (5.4). This figure shows a case with a long circular channel along with experimental data for similar channels. There is not a 1:1 matchup as the sizes and material properties are slightly different. But the same general shape can be seen in the polymer with a curved channel and curved cap to the channel. Again due to the nature of the experimental results available this rough visual comparison is the only one possible in this case.

Images of an angled capsule case, see figure (5.5), shows comparison of the model to some microcapsules. These are not quite the same situation due to not being channels

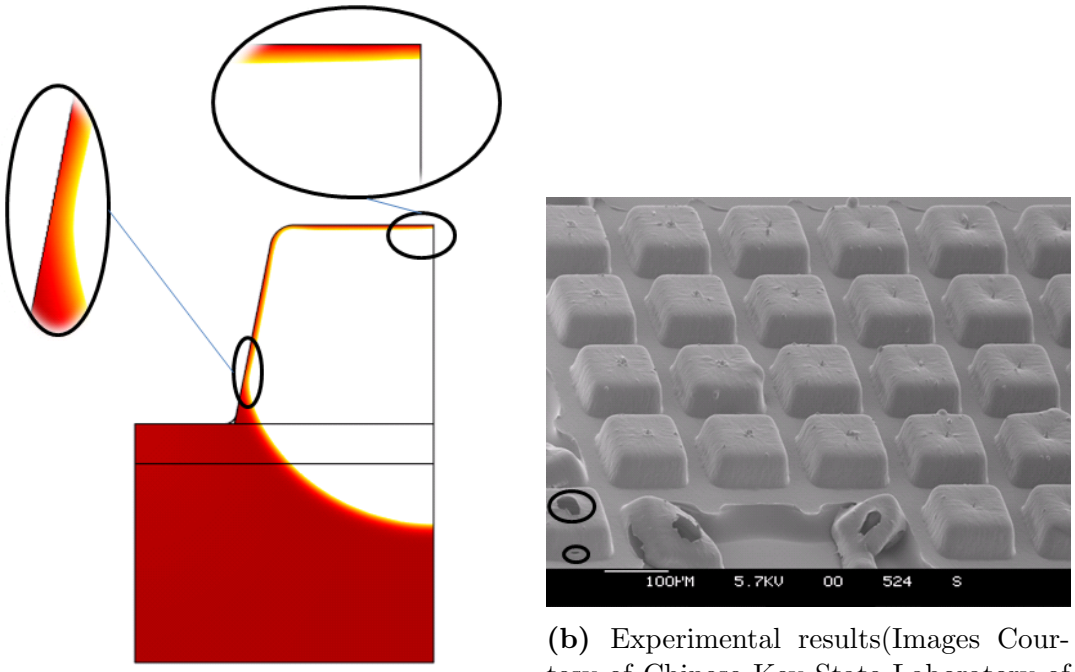

(a) Model results

(b) Experimental results(Images Courtesy of Chinese Key State Laboratory of Applied Optics)

Figure 5.5: Comparison of EFAC model results with an image of microcapsules produced experimentally.

but capsules. This is the reason that the polymer is thicker in the experimental data. Having corners will result in a larger capillary force and so thicker polymer shells in these areas. However away from the corners the two-dimensional model presented here should be sufficient to capture the correct physics. Of interest are the circled areas where on the model these areas are thinner. In the capsules produced from the experiments there are breakages in these spots implying that the polymer in this area is thinner so more prone to damage. The increased thickness is thought be a result of the corners of the capsules causing a greater capillary force than would be present in a channel, thus indicating that this particular design of micro-capsule with sharp angles would not be a suitable mask for use in production as the predictability of the polymer thickness is lower than that of simpler capsule designs.

5.3 Electrohydrodynamic Induced Patterning

As discussed previously EHDIP is a process that uses the dielectric forces at an air-polymer interface to shape molten polymers on a micron scale. Several cases have been run in COMSOL to look at the process. The masks presented here are mostly simple right angled masks other than the double masked case.

5.3.1 Right Angled Channel

Figure (5.6) shows the geometry and boundary conditions for this run. As can be seen that mask has 100 μm wide grooves spaced at 50 μm, the grooves are 100 μm deep. The polymer melt at the bottom is also 100 μm deep and there is an air gap of 50 μm separating the lowest point of the mask from the polymer.

A voltage of 250 V is applied in this case, this gives a large force at the interface as the electric field is large. There are no slip walls on the mask and on the lower surface and symmetry boundaries at either side. This is a 2D case so with the symmetry condition represents multiple infinitely long channels.

Figures (5.7) and (5.8) show the evolution of the surface over time. The polymer is represented by the red region and the air by the white. It starts with the flat surface (5.7a). After this the force due to the variations in the electric field means that the surface rises up under the lower portion of the mask (5.7b). This force increase as the electric field increases as the polymer gets closer to the top mask, thus the surface is pulled upwards until it reaches the mask (5.8a). As the contact angle is much larger than those in EFAC cases the polymer then stops rising at this point. However there is still force on the interface of the polymer so it continues rising upwards until it

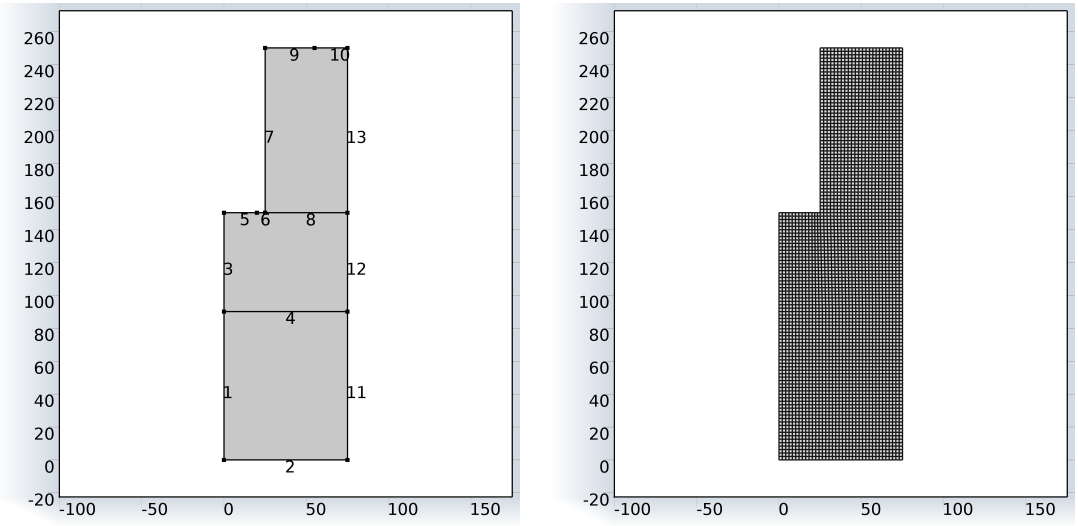

(a) Geometry **(b)** Mesh

Boundary	Electric Field	Fluid Flow
1	Zero Charge ($-\boldsymbol{n} \cdot \boldsymbol{D} = 0$)	Symmetry ($\partial \boldsymbol{u}/\partial \boldsymbol{n} = 0$)
2	Ground (0 V)	No Slip Wall ($\boldsymbol{u} = 0$)
3	Zero Charge ($-\boldsymbol{n} \cdot \boldsymbol{D} = 0$)	Symmetry ($\partial \boldsymbol{u}/\partial \boldsymbol{n} = 0$)
4	Not A Boundary	Initial Interface
5	2500 V	No Slip Wall ($\boldsymbol{u} = 0$)
6	2500 V	No Slip Wall ($\boldsymbol{u} = 0$)
7	2500 V	No Slip Wall ($\boldsymbol{u} = 0$)
9	2500 V	No Slip Wall ($\boldsymbol{u} = 0$)
10	2500 V	No Slip Wall ($\boldsymbol{u} = 0$)
11	Zero Charge ($-\boldsymbol{n} \cdot \boldsymbol{D} = 0$)	Symmetry ($\partial \boldsymbol{u}/\partial \boldsymbol{n} = 0$)
12	Zero Charge ($-\boldsymbol{n} \cdot \boldsymbol{D} = 0$)	Symmetry ($\partial \boldsymbol{u}/\partial \boldsymbol{n} = 0$)
13	Zero Charge ($-\boldsymbol{n} \cdot \boldsymbol{D} = 0$)	Symmetry ($\partial \boldsymbol{u}/\partial \boldsymbol{n} = 0$)

(c) Boundary Conditions

Figure 5.6: Geometry, mesh and boundary conditions for the first EHDIP test case, this is a high aspect ratio case. Axis units in μm

reaches the edge of the mask protrusion (5.8b). The final curved shape is caused by the surface tension, pressure and dielectric forces balancing.

Figures (5.9) and (5.10) show the evolution of the electric field over time. The streamlines are the electric field lines, the colour map shows the voltage and the white line shows the position of the air-polymer interface. The change in relative permittivity between the two materials can be seen at the interface where the electric field lines deflect. This change in dielectric constant gives rise to the dielectric forces at the interface. Initially there is less deflection in the electric field streamlines as the surface is flat, thus the streamlines are close to perpendicular to the surface. However as the surface morphology changes this deflection increases as the streamlines are no longer perpendicular to the surface.

Figures (5.11) and (5.12) show the velocities at different parts of the process, the initial force causes a low velocity in the first time step as the process has not had time to accelerate. However the surface accelerates upwards until it reaches the top. Once the polymer reaches the top it spreads out until it reaches a steady state. Once in the steady state there are recirculation in the polymer melt and the air, though these are damped out by the viscosity eventually.

This channel has a curved bottom and could be used for fabricating polymer micro-channels that do not require a lid on the top, the method could also be used to fabricate complicated microscale shapes in a polymer substrate for other similar applications such as fibre-optic wave-guides.

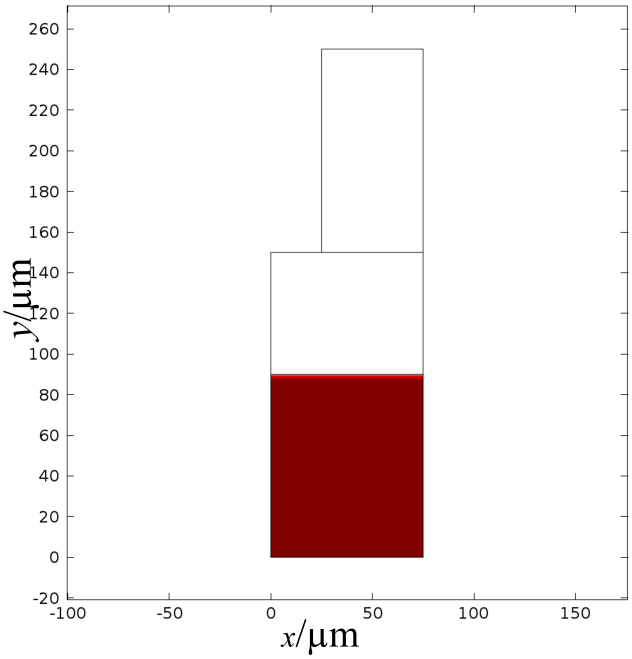

(a) 0 s

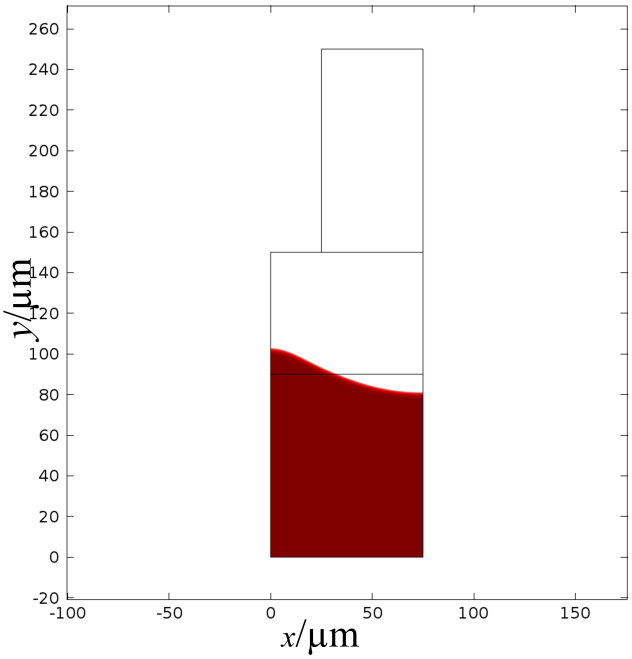

(b) 0.001 s

Figure 5.7: Evolution of the surface for an EHDIP case.

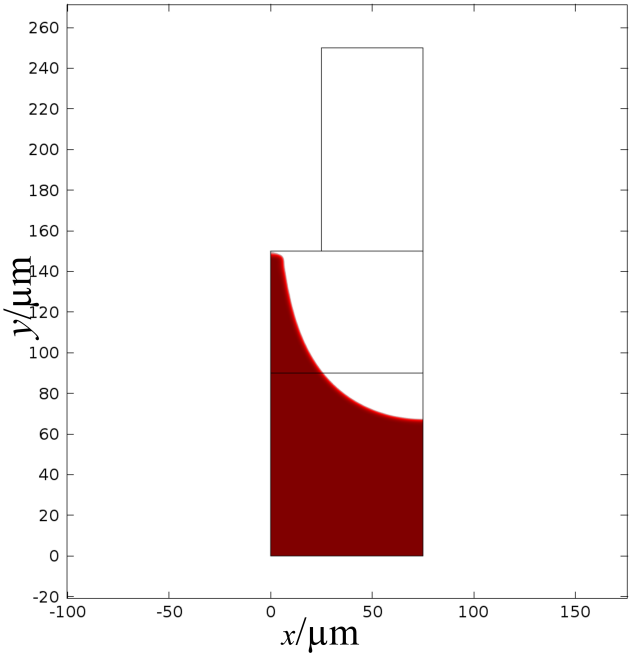

(a) 0.0017 s

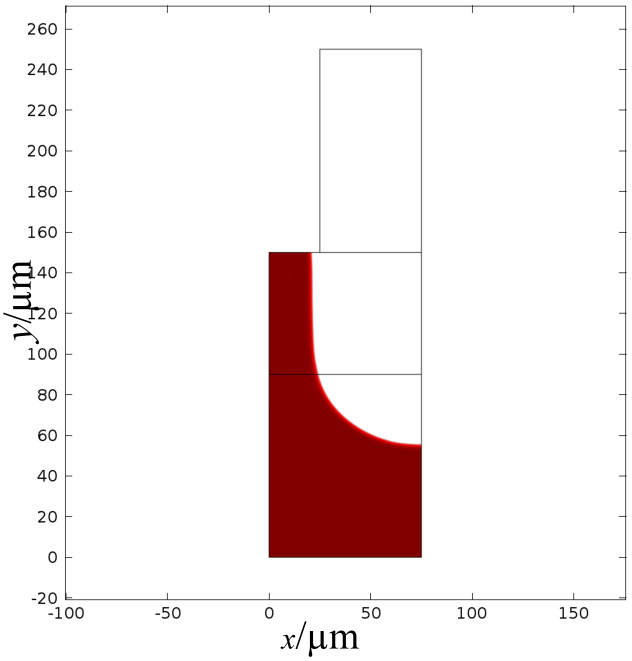

(b) 0.007 s

Figure 5.8: Evolution of the surface for an EHDIP case.

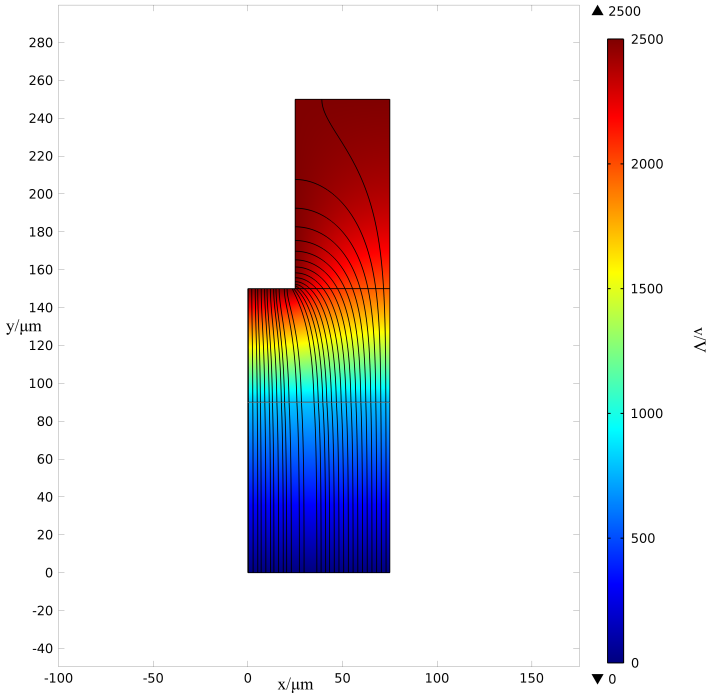

(a) 0s

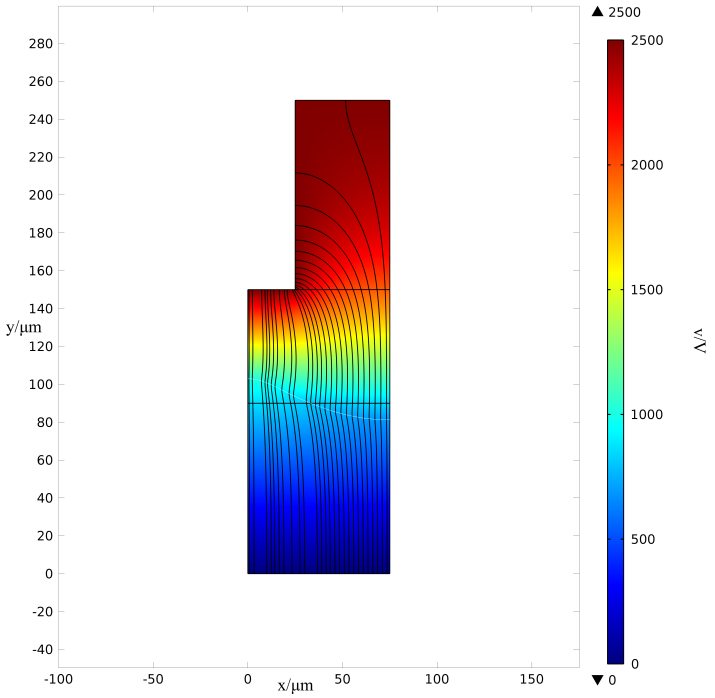

(b) 0.001s

Figure 5.9: Evolution of the electric field for an EHDIP case.

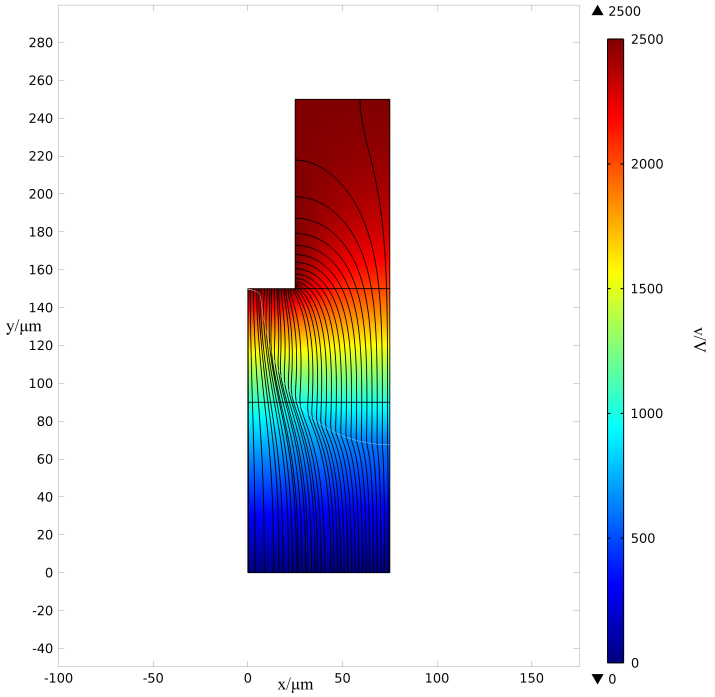

(a) 0.0017s

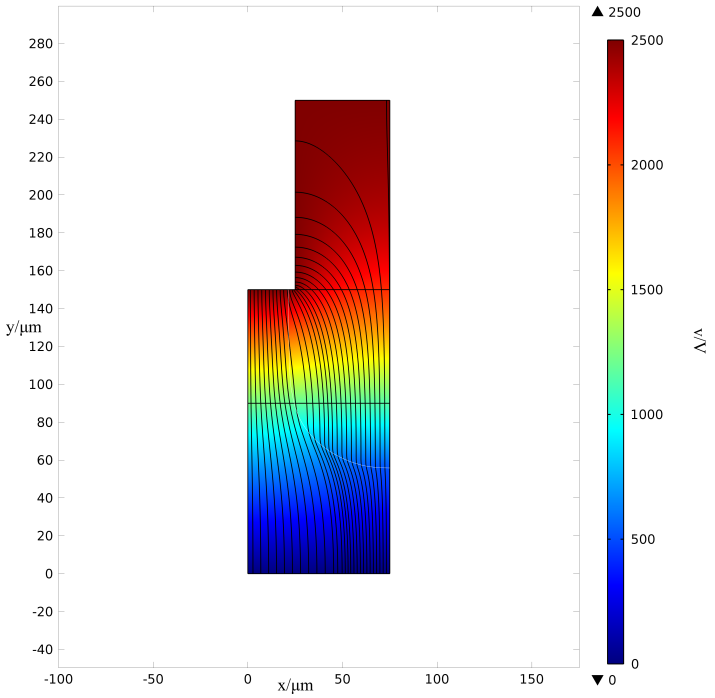

(b) 0.007s

Figure 5.10: Evolution of the electric field for an EHDIP case.

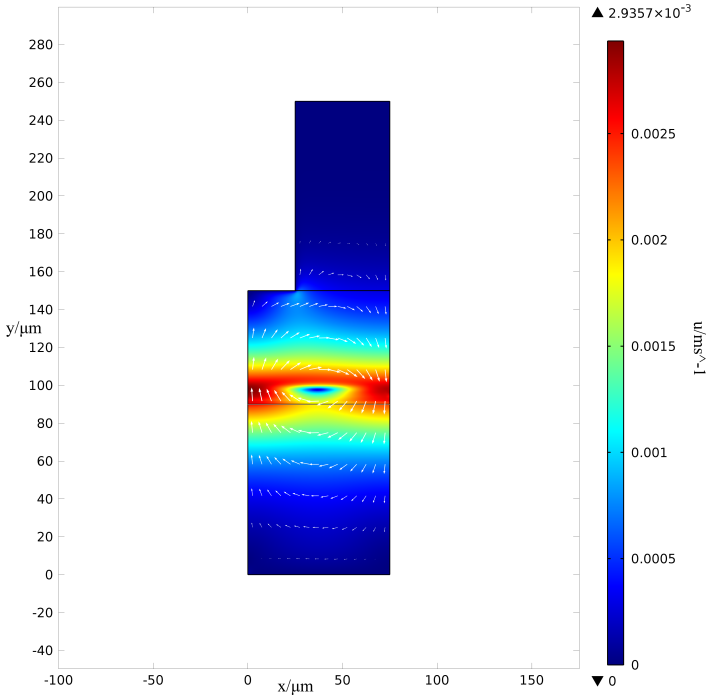

(a) 0s

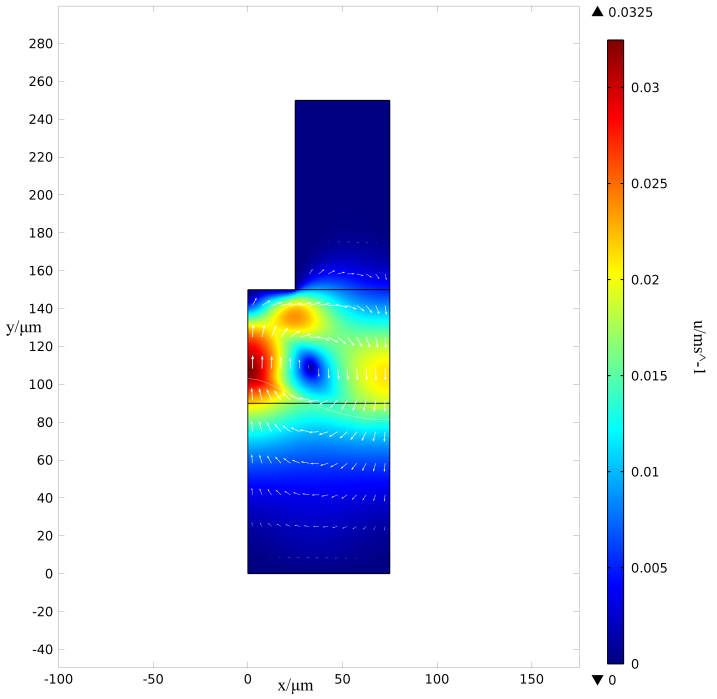

(b) 0.001s

Figure 5.11: Evolution of the velocities for an EHDIP case.

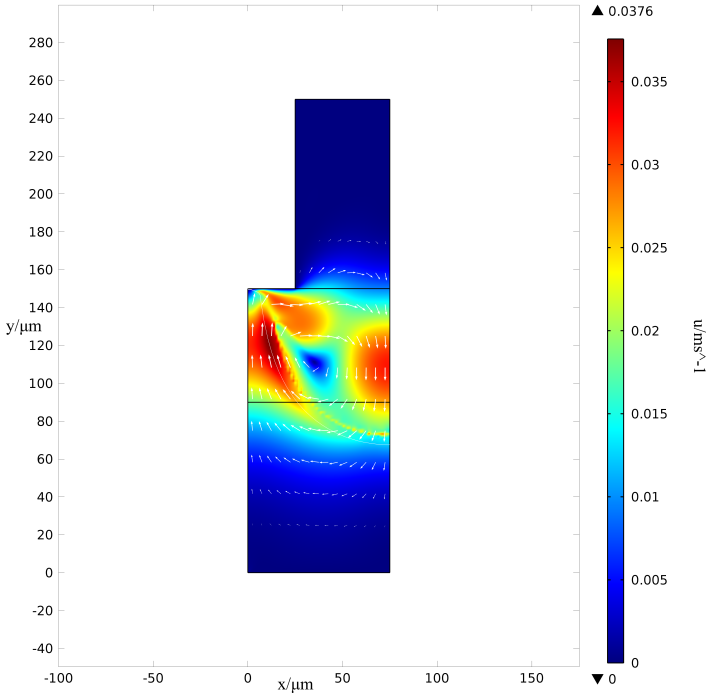

(a) 0.0017s

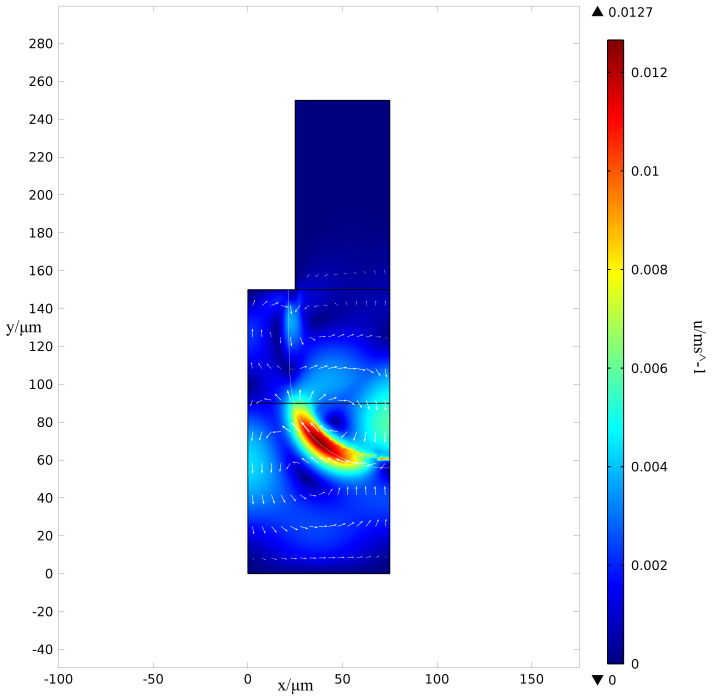

(b) 0.007s

Figure 5.12: Evolution of the velocities for an EHDIP case.

5.3.2 Double Masked EHDIP

During the modelling an idea was had to try using a shaped mask at the bottom rather than the top. This was suggested as as way to get more useful shapes for producing structures such as lenses. When this was tested however it was found that the shape of the electric field that this configuration produced meant that the dielectric forces were not in the correct directions to get the desired effects. It was therefore decided to use a "double mask" with a duplicate mask at the top and the bottom of the polymer, see figure (5.13). In this case it was also assumed that the rounded top section of the mask was filled in with a material so there would be no flow in it (the material has been modelled with a relative permittivity of 1, however results should be similar with other permittivities).

The case presented here is for a manufacturing a convexo-concave micro-lens, as this geometry is only an example the focal length is arbitrary but this could be altered by changing the shape of the outer mask, the air gap and the initial polymer thickness to provide the desired inner and outer shape to the lens. This method has only been tested with this mask, as it is a typical lens shape for LED lighting, however it is likely possible to manufacture different shapes using this method.

The evolution of the surface as seen in figures (5.14) and (5.15) is similar to that in the square channel EHDIP case. It starts with the polymer rising upwards due to the imbalance in the electric field, the polymer eventually reaches the top mask and spreads out. Due to the shape of the outer mask at the bottom this leaves a convexo-concave lens shape with an outer curved surface and an inner curved surface. The outer surface of this lens can obviously be manipulated by changing the shape of the bottom mask. The shape of the inner surface can then be altered by modifying the

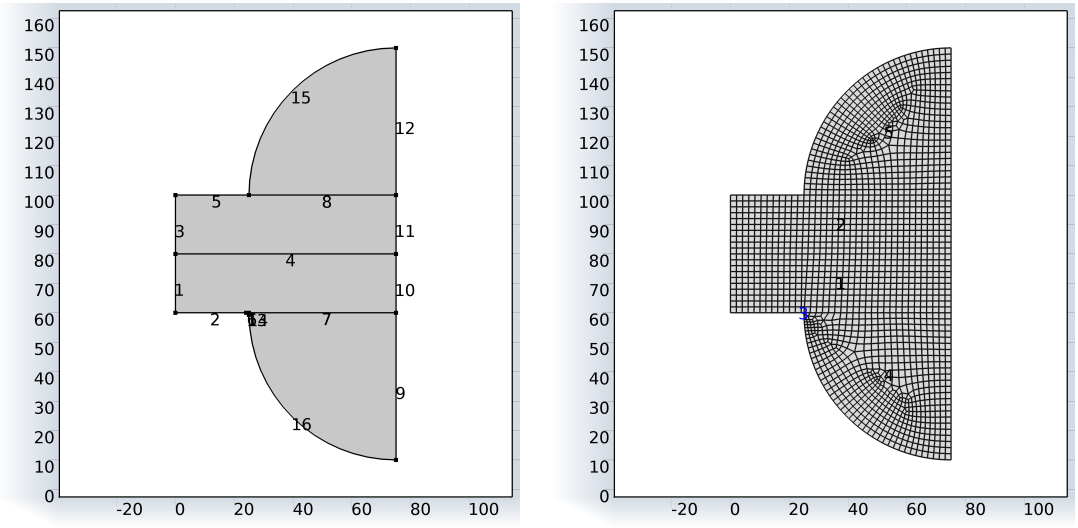

(a) Geometry **(b)** Mesh

Boundary	Electric Field	Fluid Flow
1	Zero Charge ($-\boldsymbol{n}\cdot\boldsymbol{D}=0$)	Symmetry ($\partial\boldsymbol{u}/\partial\boldsymbol{n}=0$)
2	Ground (0 V)	Slip Wall ($\boldsymbol{u}\cdot\widehat{\boldsymbol{n}}=0$)
3	Zero Charge ($-\boldsymbol{n}\cdot\boldsymbol{D}=0$)	Symmetry ($\partial\boldsymbol{u}/\partial\boldsymbol{n}=0$)
4		Initial Interface
5	500 V	Slip Wall ($\boldsymbol{u}\cdot\widehat{\boldsymbol{n}}$)
6		Slip Wall ($\boldsymbol{u}\cdot\widehat{\boldsymbol{n}}$)
8		Slip Wall ($\boldsymbol{u}\cdot\widehat{\boldsymbol{n}}$)
9,10,11,12	Axial Symmetry	Axial Symmetry
13	Ground (0 V)	
14		Slip Wall ($\boldsymbol{u}\cdot\widehat{\boldsymbol{n}}$)
15	500V	
16	Ground (0 V)	Slip Wall ($\boldsymbol{u}\cdot\widehat{\boldsymbol{n}}$)

(c) Boundary Conditions

Figure 5.13: The geometry, mesh and boundary conditions for a lens test case. Axis units in μm

thickness of the initial polymer or the airgap between the polymer and the top mask.

The electric field evolution shown in figures (5.16) and (5.17) is similar to in the previous case showing the deflection of the electric field at the interface due to the change in the relative permittivity at the air-polymer boundary.

As this technique allows the shaping of both sides of the structure it has the potential for the manufacture of microlens arrays by incorporating several lenses in one mask. There are also many other potential uses where shaped micro-structures are needed.

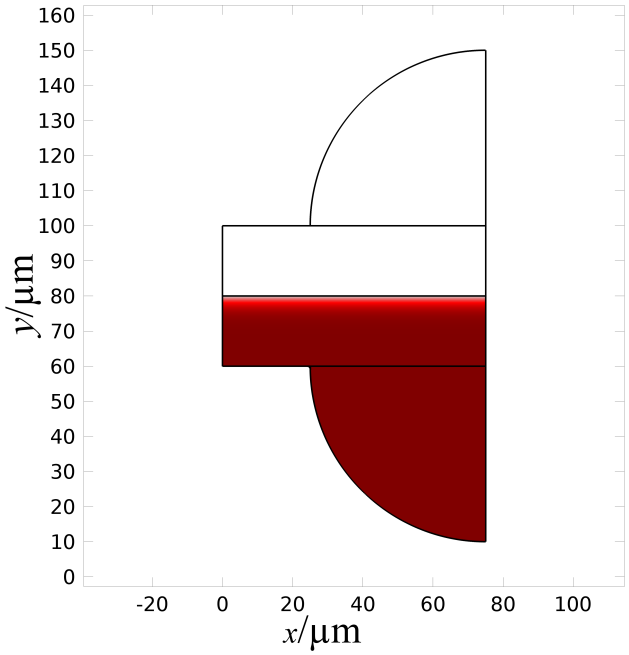

(a) 0.001s

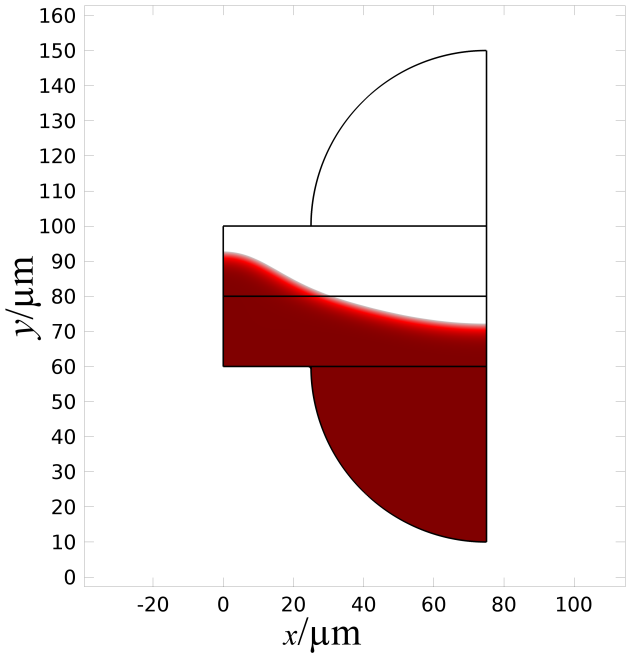

(b) 0.022s

Figure 5.14: Evolution of the surface for a lens geometry.

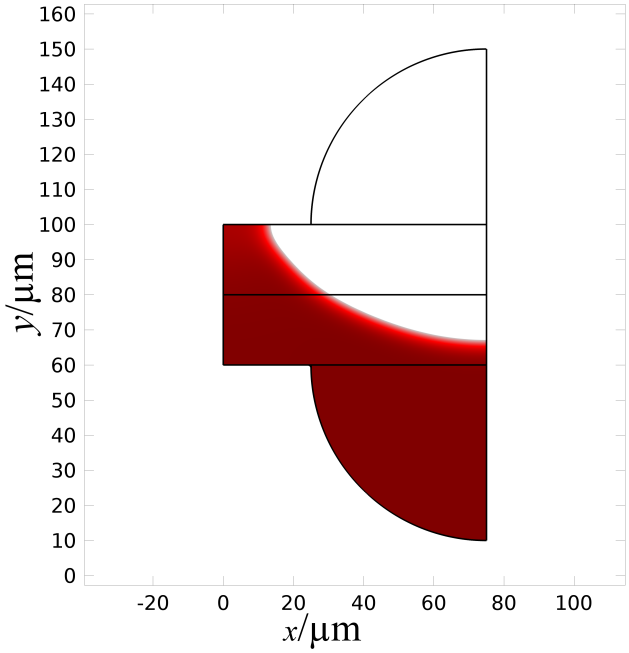

(a) 0.027s

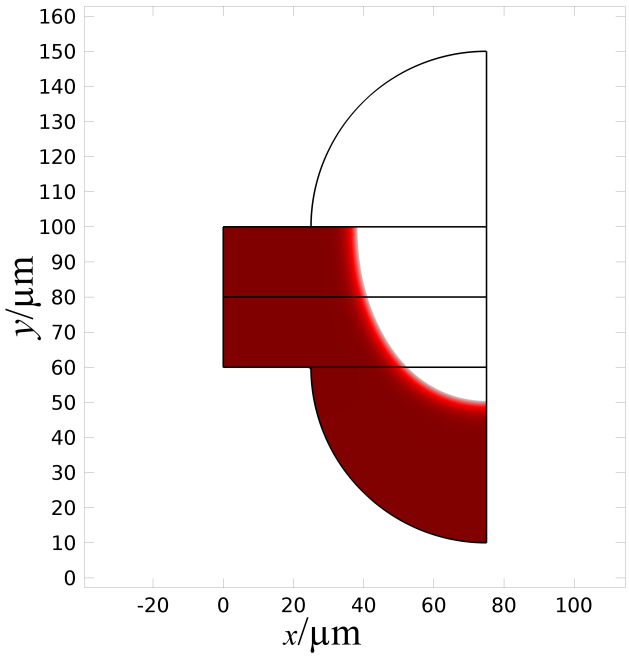

(b) 0.1s

Figure 5.15: Evolution of the surface for a lens geometry.

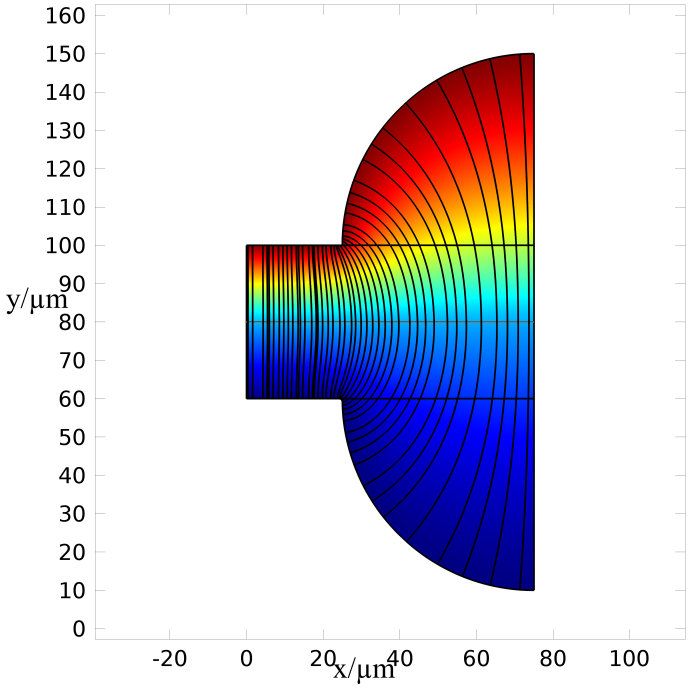

(a) 0.001s

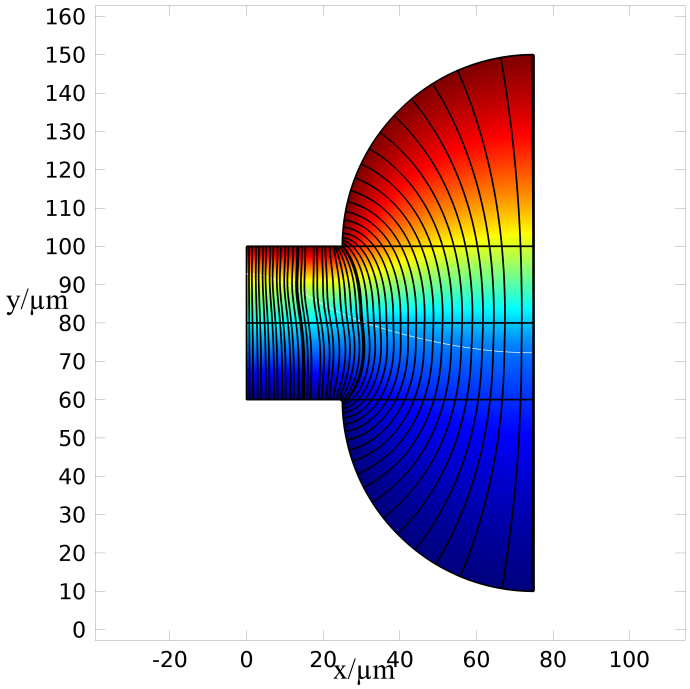

(b) 0.022s

Figure 5.16: Evolution of the electric field for a lens geometry.

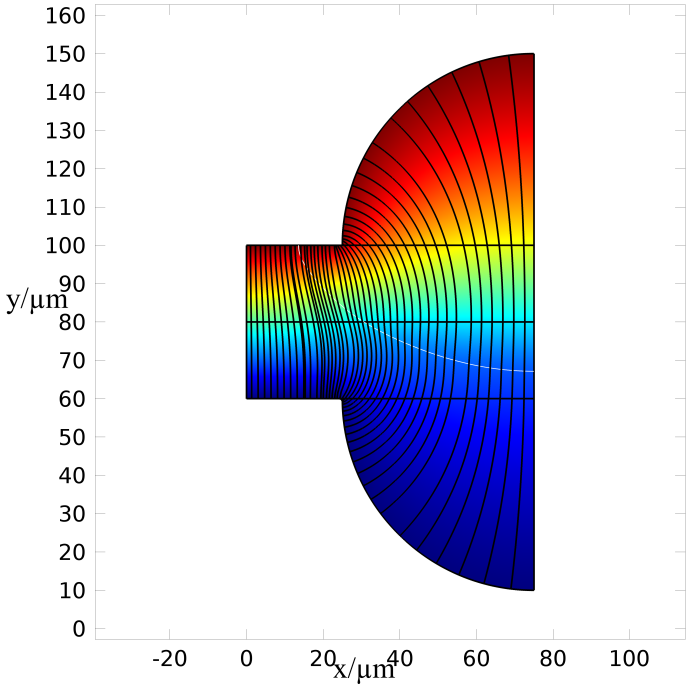

(a) 0.027s

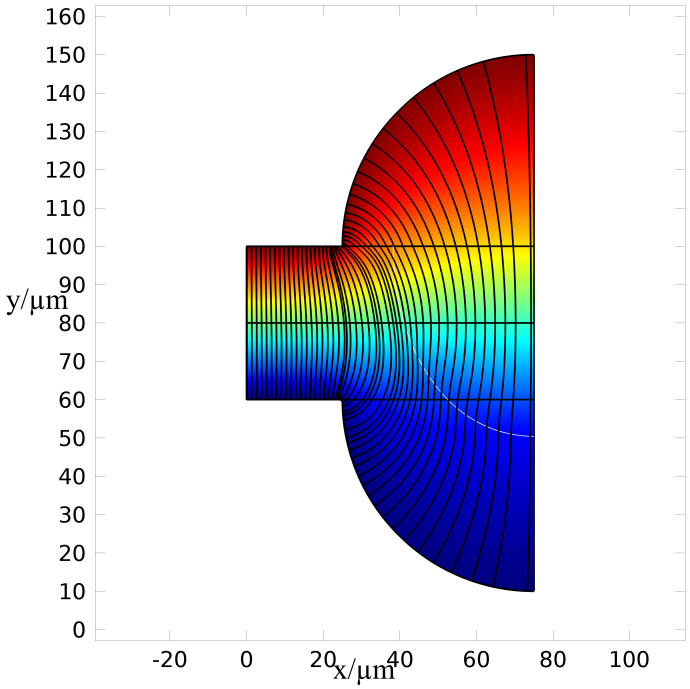

(b) 0.1s

Figure 5.17: Evolution of the electric field for a lens geometry.

5.4 Electric Field Assisted Capillarity

The Electric Field assisted Capillarity (EFAC) results extend the EHDIP model to include heavily wetted surfaces on the top mask, this causes the polymer to coat the top mask forming an enclosed shape.

Presented here are several different shapes to the top mask, enabling the production of different shaped micro-channels. The caps produced by the process are typically $1 - 2\,\mu$m thick.

5.4.1 Rounded Mask

This mask will produce round micro-channels within the polymer. The geometry, mesh and boundary conditions for this case can be seen in figure (5.23). It is hard to see but in the corner of the mask between the arc and the flat surface, there is a curved section where only the electric field is solved, this is to avoid the numerical difficulties of solving an electric field at a point, which in reality there would not be, as this causes as singularity, therefore only the electric field is solved in this section and not the flow.

The evolution of the surface of the polymer is seen in figures (5.19) and (5.20). In the initial conditions the surface is flat (5.19a). It then begins to gradually rise upwards towards the top mask, when it reaches the top mask (5.19(b) the capillary force becomes dominant and the polymer is pulled along the surface of the mask 5.20(a), Finally it reaches the top of the mask and forms a near cylindrical bubble in the polymer (5.20b). At this stage the pressure, surface tension and electric field forces are balanced at the surface so it no longer moves. There are however currents

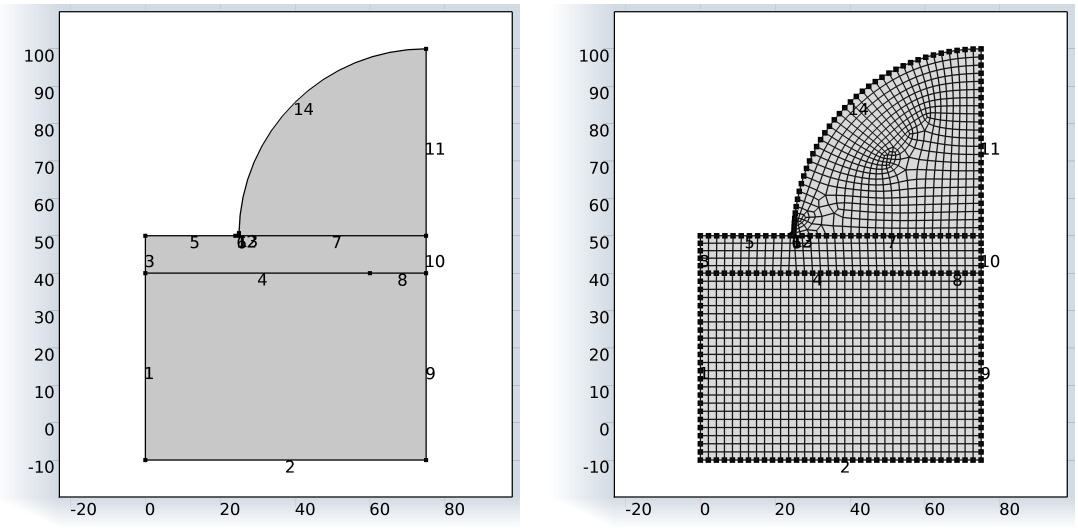

(a) Geometry **(b)** Mesh

Boundary	Electric Field	Fluid Flow
1	Zero Charge ($-\boldsymbol{n} \cdot \boldsymbol{D} = 0$)	Symmetry ($\partial \boldsymbol{u}/\partial \boldsymbol{n} = 0$)
2	Ground (0 V)	Slip Wall ($\boldsymbol{u} \cdot \boldsymbol{n} = 0$)
3	Zero Charge ($-\boldsymbol{n} \cdot \boldsymbol{D} = 0$)	Symmetry ($\partial \boldsymbol{u}/\partial \boldsymbol{n} = 0$)
4		Initial Interface
5	250 V	Wetted wall ($\theta = 20°$)
6	250 V	
8		Initial Interface
9	Zero Charge ($-\boldsymbol{n} \cdot \boldsymbol{D} = 0$)	Symmetry ($\partial \boldsymbol{u}/\partial \boldsymbol{n} = 0$)
10	Zero Charge ($-\boldsymbol{n} \cdot \boldsymbol{D} = 0$)	Symmetry ($\partial \boldsymbol{u}/\partial \boldsymbol{n} = 0$)
11	Zero Charge ($-\boldsymbol{n} \cdot \boldsymbol{D} = 0$)	Symmetry ($\partial \boldsymbol{u}/\partial \boldsymbol{n} = 0$)
12		Wetted wall ($\theta = 20°$)
13		Wetted wall ($\theta = 20°$)
14	250 V	Wetted wall ($\theta = 20°$)

(c) Boundary Conditions

Figure 5.18: The geometry, mesh and boundary conditions. Axis units in μm

still, primarily in the air.

The evolution of the electric field shown in figures (5.21) and (5.22) is similar to in EHDIP, the same deflections at the surface of the polymer are present. As can be seen the electric field changes due to the changing surface morphology, this is due to the altering dielectric properties based on the position of the surface.

This mask shape produces roughly cylindrical micro-channels, which by the nature of their production by surface tension and electric fields have a smooth surface at the bottom, much smoother than could be produced by using conventional techniques for micro-channel production. This type of channel has a large range of uses in microfluidics and with complex top masks arrays of microchannels could potentially be produced using this technique.

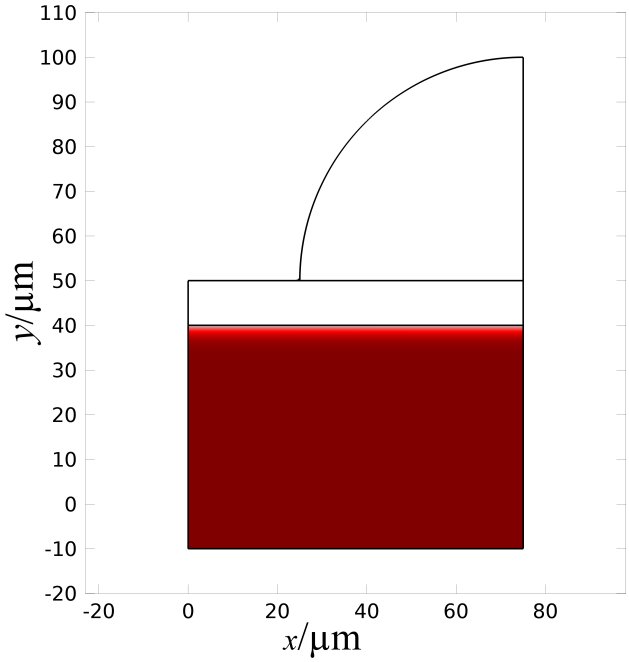

(a) 0.001s

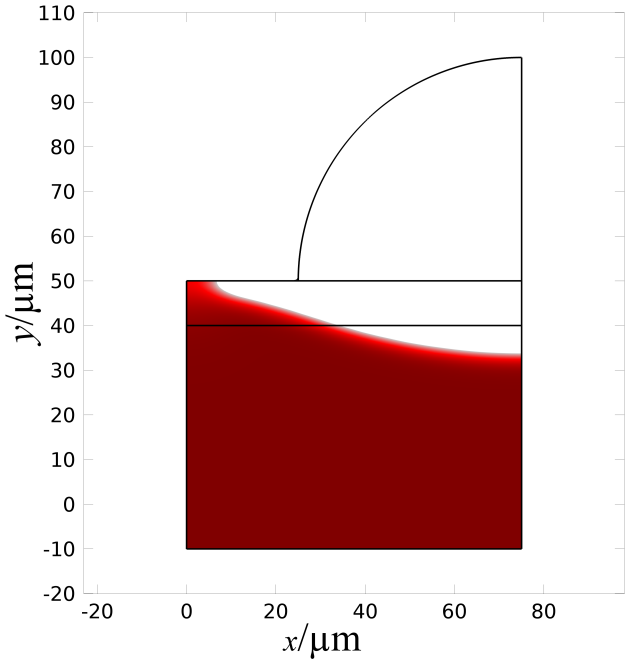

(b) 0.022s

Figure 5.19: Evolution of the surface for an EFAC case.

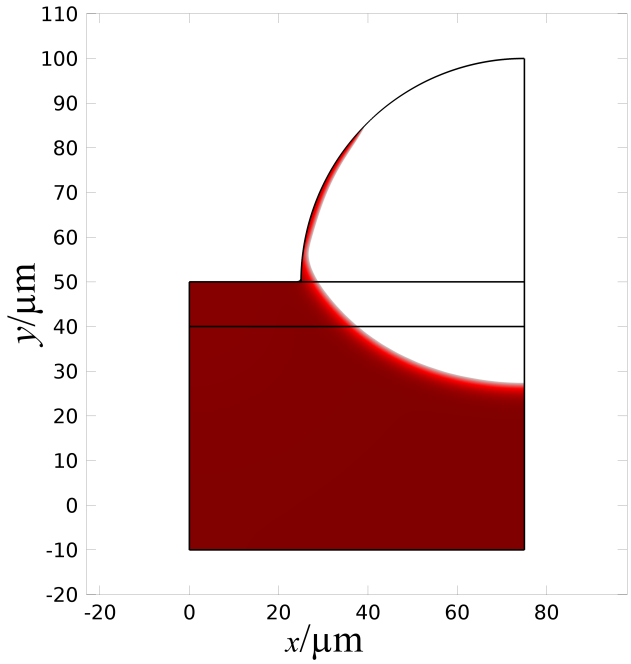

(a) 0.027s

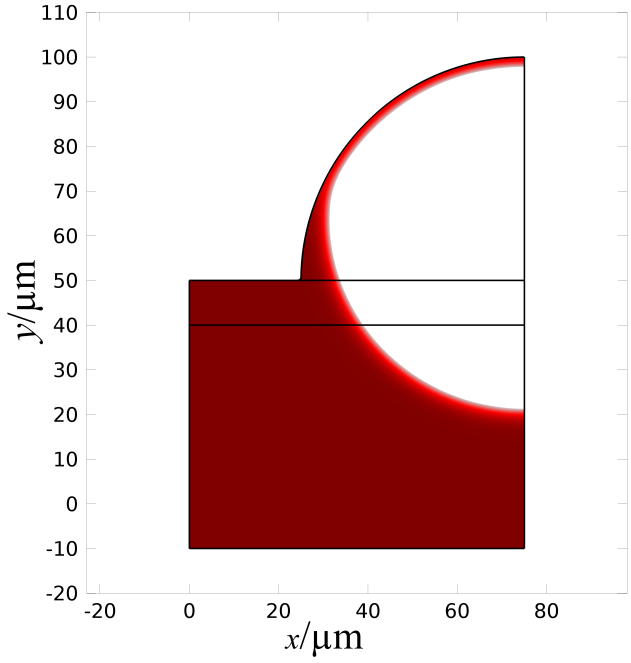

(b) 0.1s

Figure 5.20: Evolution of the surface for an EFAC case.

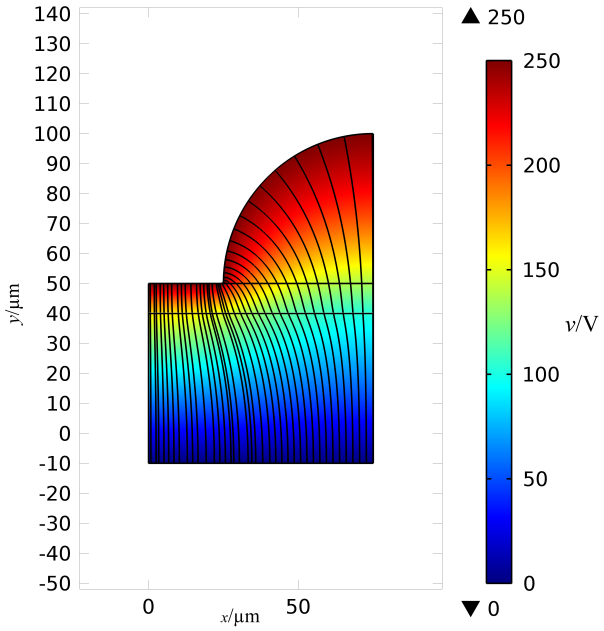

(a) 0.001s

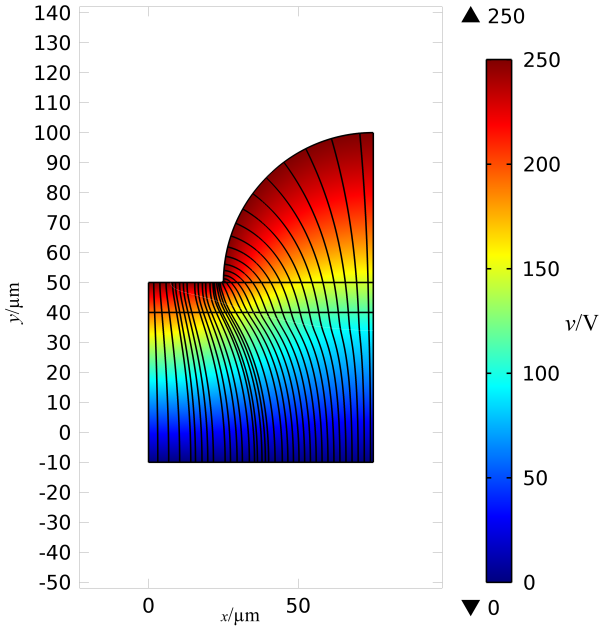

(b) 0.022s

Figure 5.21: Evolution of the electric field for an EFAC case.

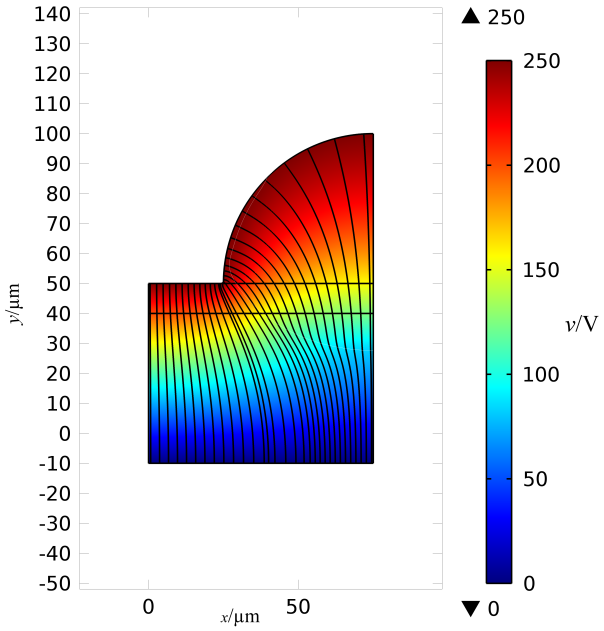

(a) 0.027s

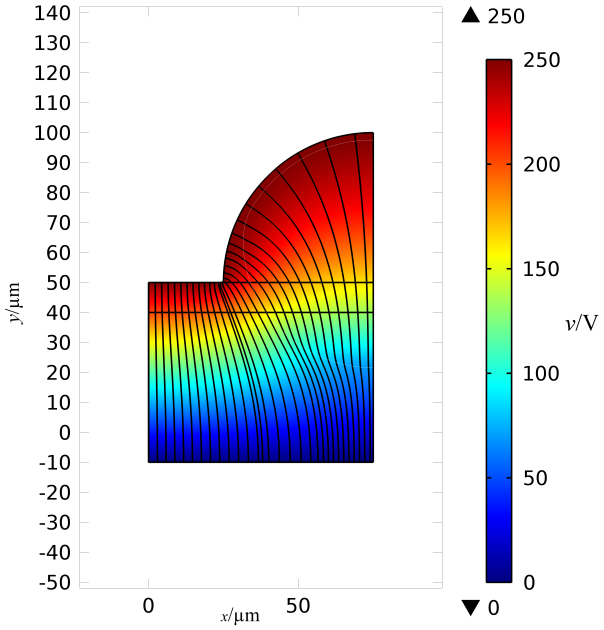

(b) 0.1s

Figure 5.22: Evolution of the electric field for an EFAC case.

5.4.2 Angled Mask

The previous example showed an EFAC case with a round mask at the top, this case presents an angular mask. Though this mask has some straight sides there are also rounded corners. This is because without these rounded corners the polymer is unable to fully coat the inside of the mask. There is also the same small area where only the electric field is solved in order to avoid the singularity in the electric field and thus unrealistic forces.

In this case the evolution of the surface as shown in figures (5.24) and (5.25) is very similar to the previous case. Notable features of this case are the thin area of polymer where the curved part of the polymer meets the mask, in experiments there is also a thin area here and it is prone to breaking.

The electric field, figures (5.26) and (5.27), has a similar changing electric field to the previous case. The results demonstrate the deflection of the electric field at the surface of the polymer due to the change in the permittivity. This change in permittivity is what gives rise to the dielectric forces.

These channels could again be used for a wide range of applications in the field of microfluidics.

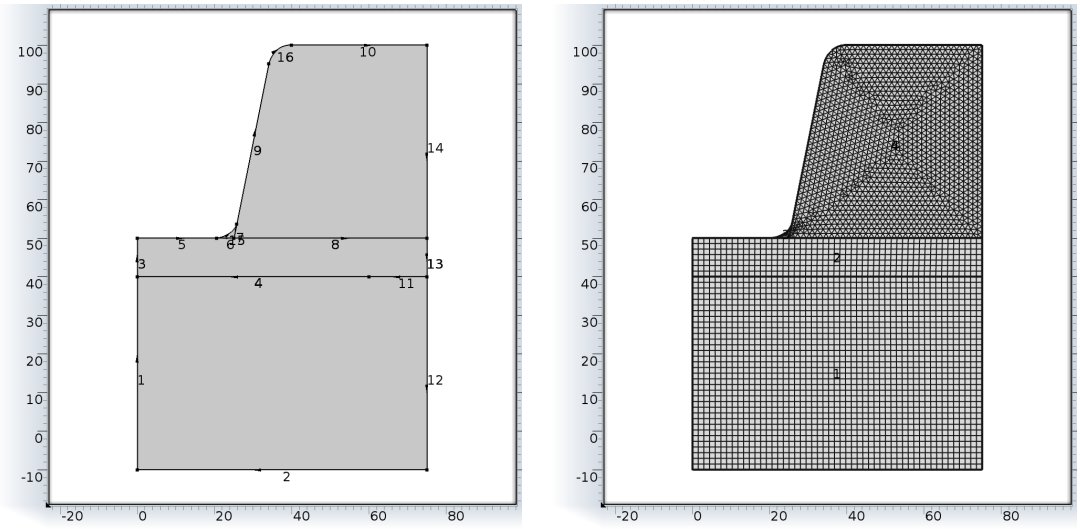

(a) Geometry **(b)** Mesh

Boundary	Electric Field	Fluid Flow
1	Zero Charge ($-\boldsymbol{n} \cdot \boldsymbol{D} = 0$)	Symmetry ($\partial \boldsymbol{u}/\partial \boldsymbol{n} = 0$)
2	Ground (0 V)	Slip Wall ($\boldsymbol{u} \cdot \boldsymbol{n} = 0$)
3	Zero Charge ($-\boldsymbol{n} \cdot \boldsymbol{D} = 0$)	Symmetry ($\partial \boldsymbol{u}/\partial \boldsymbol{n} = 0$)
4		Initial Interface
5	300 V	Wetted wall ($\theta = 20°$)
6		Wetted wall ($\theta = 20°$)
7		Wetted wall ($\theta = 20°$)
9	300 V	Wetted wall ($\theta = 20°$)
10	300 V	Wetted wall ($\theta = 20°$)
11		Initial Interface
12,13,14	Zero Charge ($-\boldsymbol{n} \cdot \boldsymbol{D} = 0$)	Symmetry ($\partial \boldsymbol{u}/\partial \boldsymbol{n} = 0$)
15	300V	
16	300 V	Wetted wall ($\theta = 20°$)

(c) Boundary Conditions

Figure 5.23: The geometry, mesh and boundary conditions for an EFAC case with an angled top mask. Axis units in μm

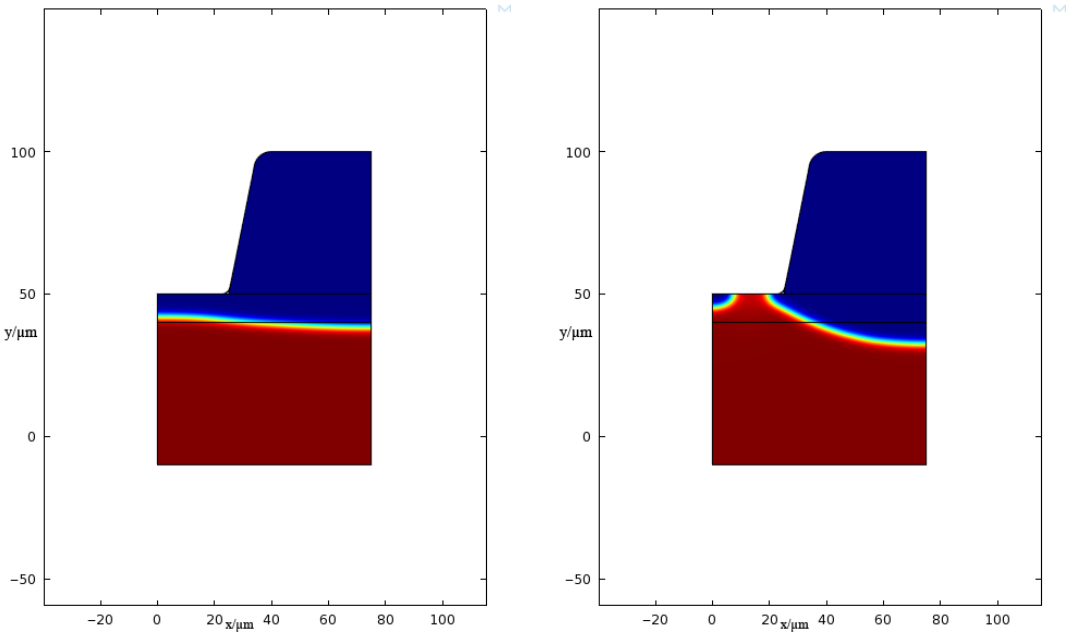

(a) 0.001s **(b)** 0.021s

Figure 5.24: Evolution of the surface for an EFAC case with an angled top mask.

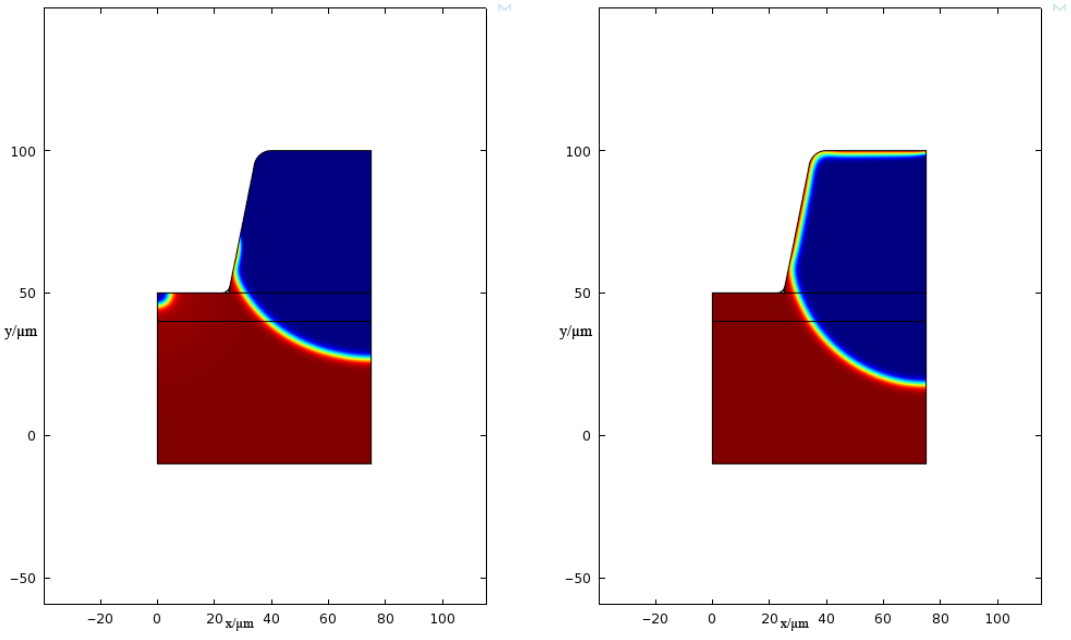

(a) 0.027s **(b)** 0.1s

Figure 5.25: Evolution of the surface for an EFAC case with an angled top mask.

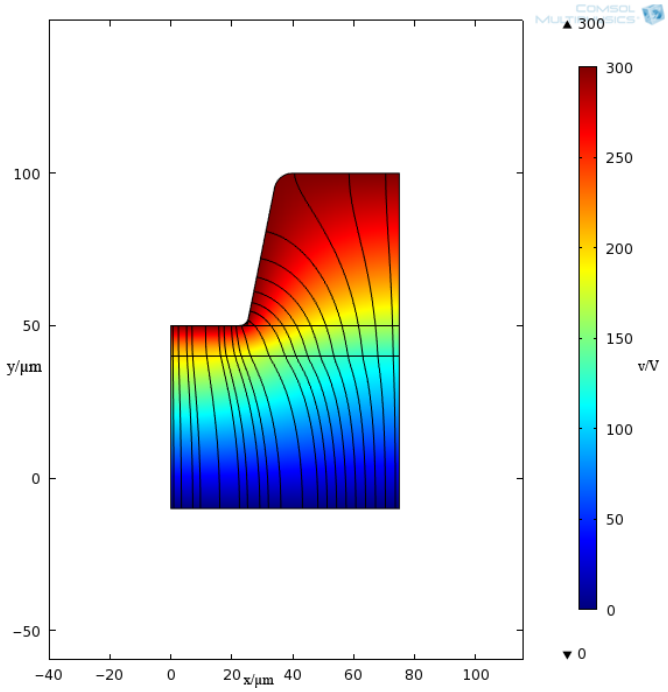

(a) 0.001s

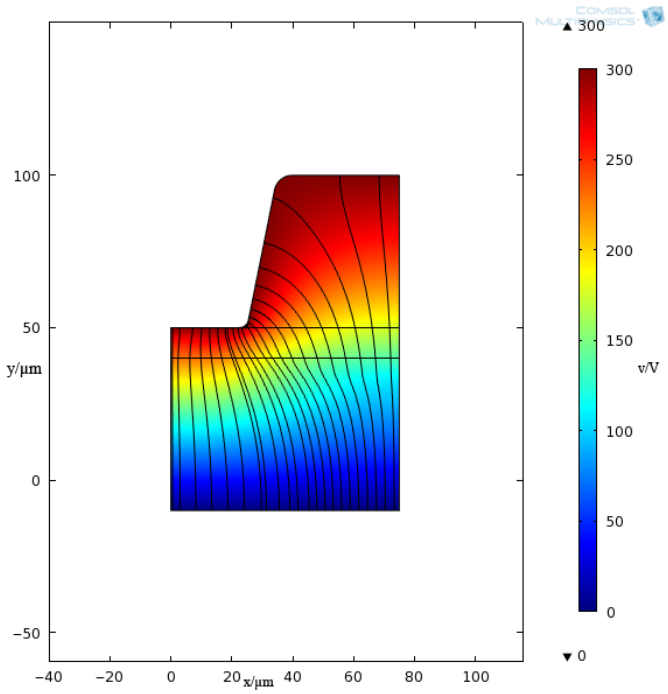

(b) 0.021s

Figure 5.26: Evolution of the electric field for an EFAC case with an angled top mask.

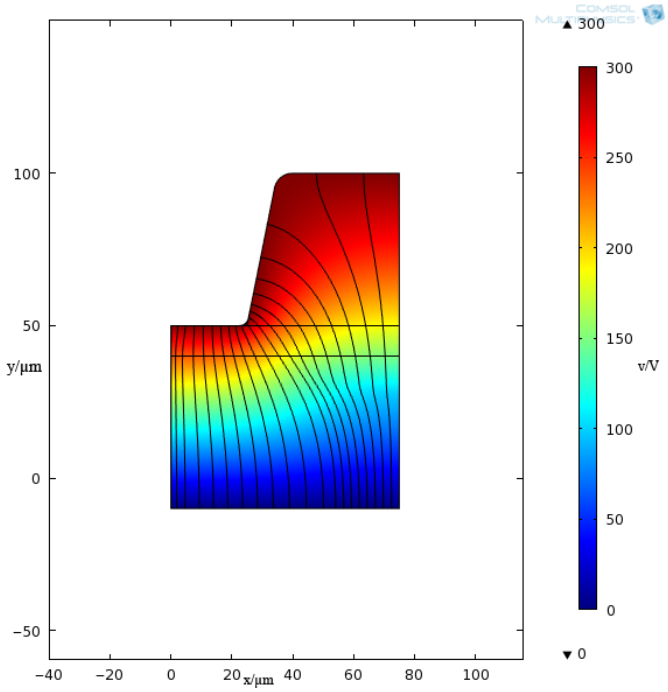

(a) 0.027s

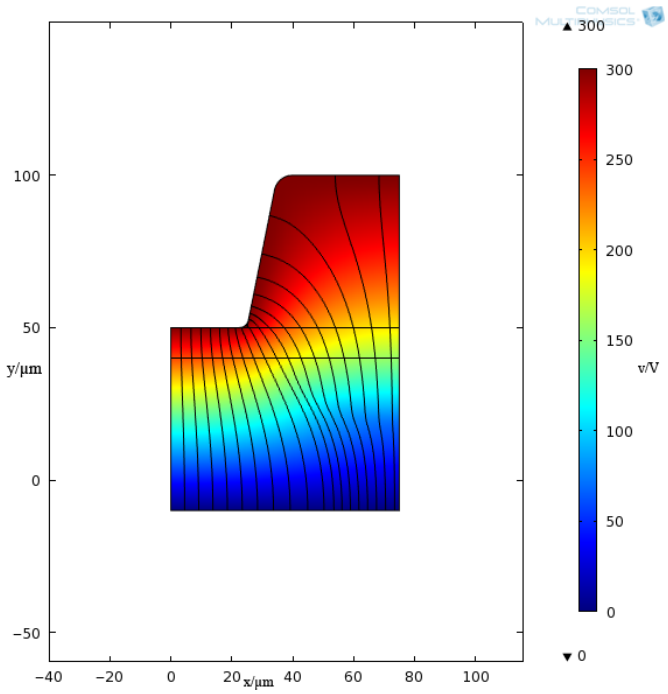

(b) 0.1s

Figure 5.27: Evolution of the electric field for an EFAC case with an angled top mask.

5.4.3 Right Angled Mask

This case has a similar mask but it uses 90 degree angles. This provides a roughly square cap on the channels, the geometry and mesh for this case can be seen in figure (5.28). The mask still has the same curved corners of the previous case for the same reasons.

As can be seen from the evolution of the surface of the polymer shown in figures (5.29) and (5.30), this case results in a roughly semicircular channel with a roughly square cap on the top. The evolution other than that is standard for the model, with the interface rising up under the lowest portion of the mask, reaching the surface and then coating the inside of the top mask to produce a fully enclosed microstructure.

The evolution of the electric field, figures (5.31) and (5.32), is again similar to the previous cases. The deflections a the polymer air-interface can again be seen along with the changing electric field as the morphology of the polymer changes. The channels produced could be used for a wide range of microfluidic applications.

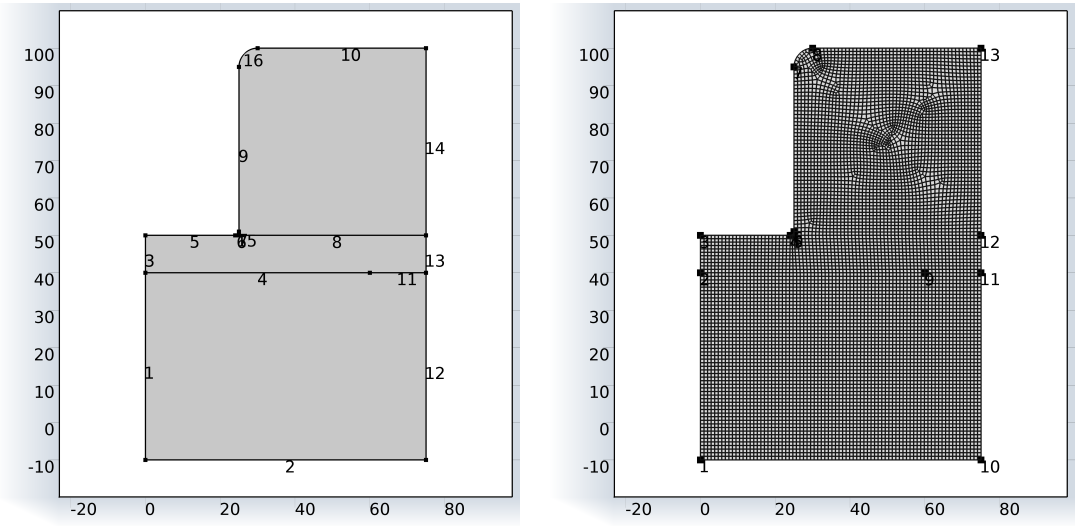

(a) Geometry **(b)** Mesh

Boundary	Electric Field	Fluid Flow
1	Zero Charge ($-\boldsymbol{n}\cdot\boldsymbol{D}=0$)	Symmetry ($\partial\boldsymbol{u}/\partial\boldsymbol{n}=0$)
2	Ground (0 V)	Slip Wall ($\boldsymbol{u}\cdot\boldsymbol{n}=0$)
3	Zero Charge ($-\boldsymbol{n}\cdot\boldsymbol{D}=0$)	Symmetry ($\partial\boldsymbol{u}/\partial\boldsymbol{n}=0$)
4		Initial Interface
5	250 V	Wetted wall ($\theta=20°$)
6		Wetted wall ($\theta=20°$)
7		Wetted wall ($\theta=20°$)
9	250 V	Wetted wall ($\theta=20°$)
10	250 V	Wetted wall ($\theta=20°$)
11		Initial Interface
12,13,14	Zero Charge ($-\boldsymbol{n}\cdot\boldsymbol{D}=0$)	Symmetry ($\partial\boldsymbol{u}/\partial\boldsymbol{n}=0$)
15	250V	
16	250 V	Wetted wall ($\theta=20°$)

(c) Boundary Conditions

Figure 5.28: Geometry, mesh and boundary conditions for an EFAC case with a right angled top mask. Axis units in μm

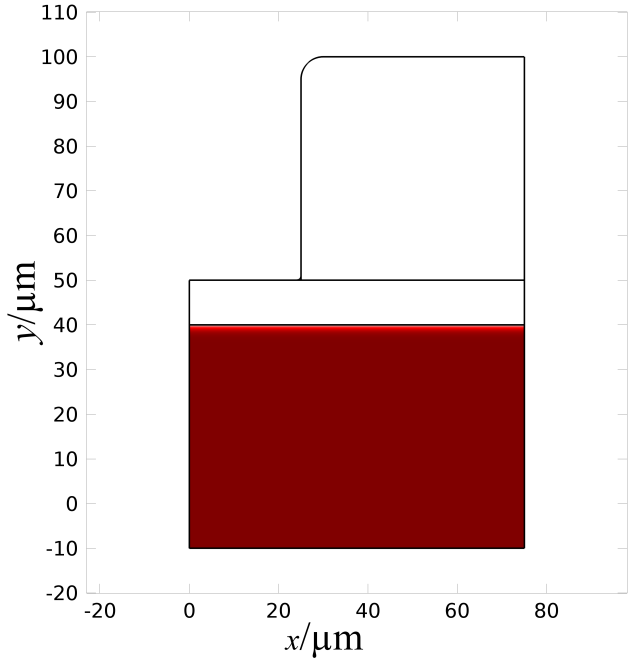

(a) 0.001s

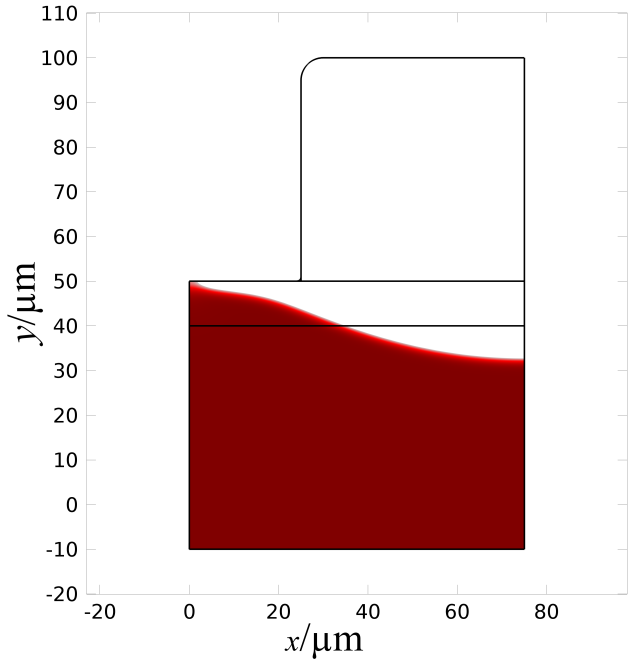

(b) 0.022s

Figure 5.29: Evolution of the surface for an EFAC case.

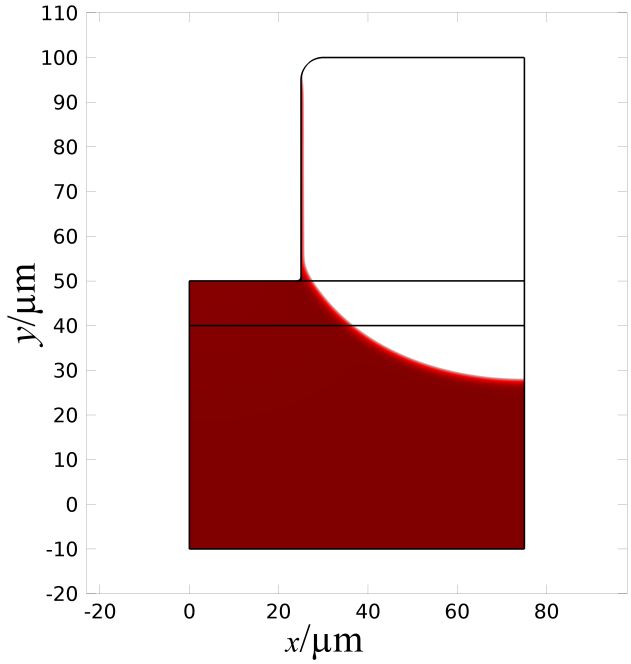

(a) 0.027s

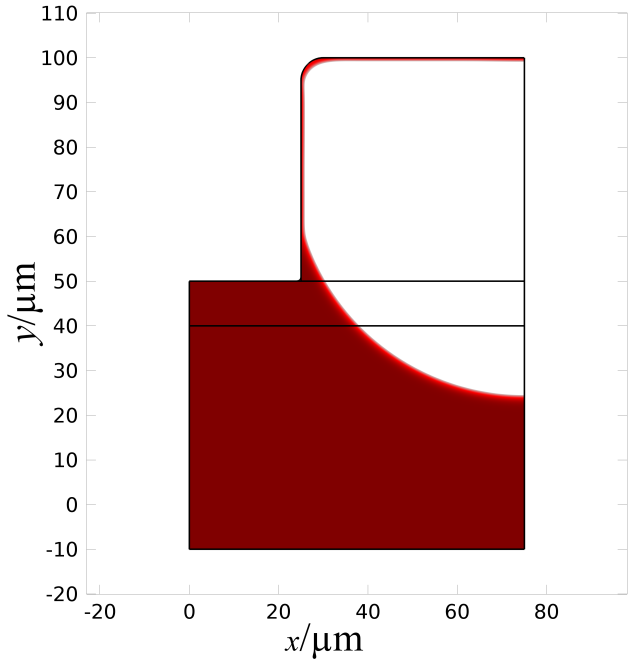

(b) 0.1s

Figure 5.30: Evolution of the surface for an EFAC case.

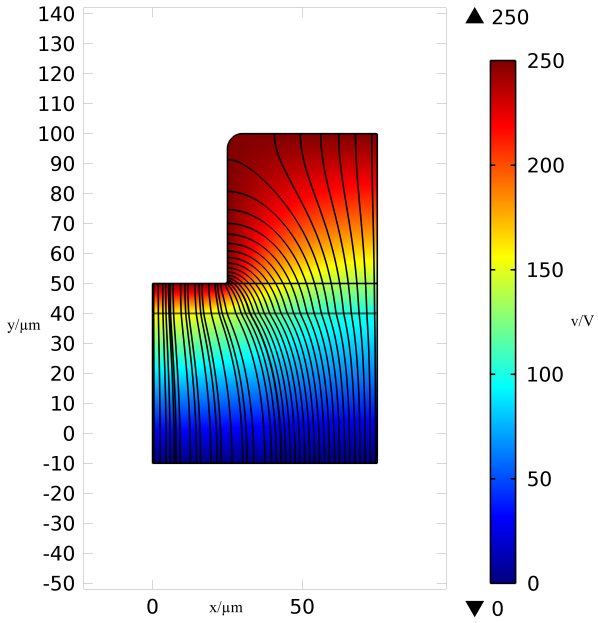

(a) 0.001s

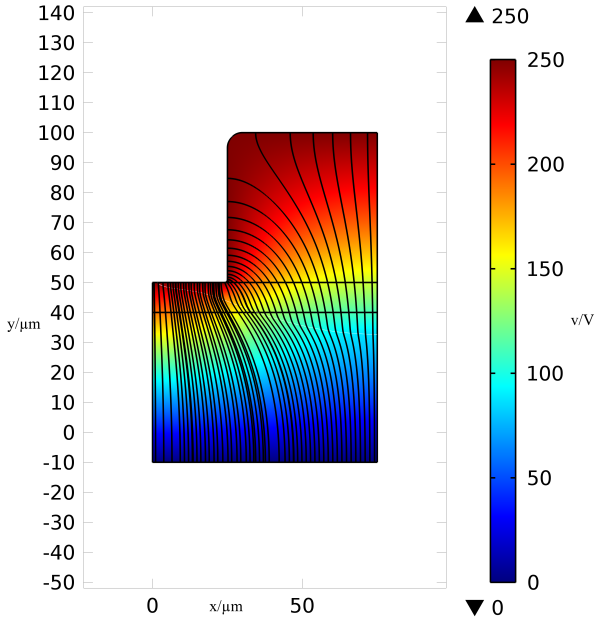

(b) 0.022s

Figure 5.31: Evolution of the electric field for an EFAC case.

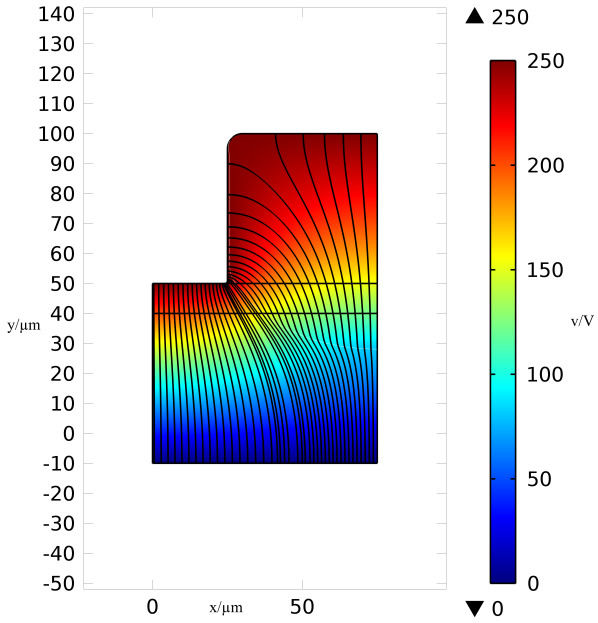

(a) 0.027s

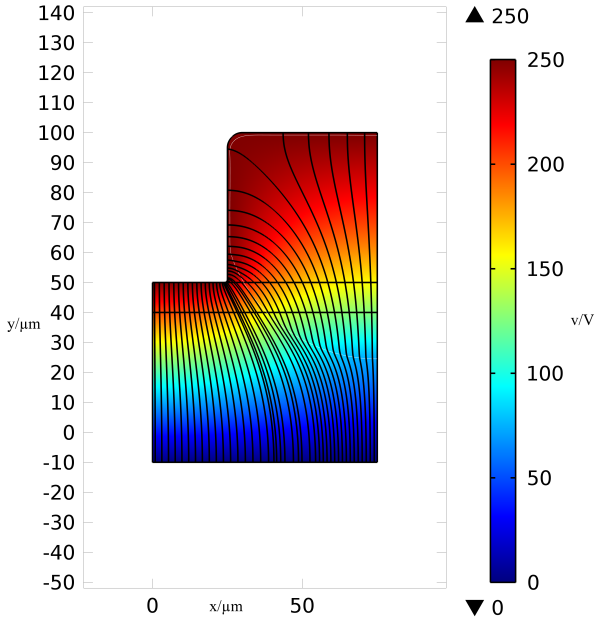

(b) 0.1s

Figure 5.32: Evolution of the electric field for an EFAC case.

5.4.4 Double Masked EFAC: Stackable Channels

5.4.4.1 "Hexagonal" Mask

One of the problems with EFAC as it is presented here is that the structures produced can only be used to form either a single layer of micro capsules or an array of micro channels in a single layer. To solve this problem the double masked technique described earlier to produce a micro-lens was extended to produce stackable channels. The obvious advantage of this being that multiple layered structures will be possible. Again like the EHDIP lens technique this is currently only theoretical and has not been tested experimentally.

The first of these stackable channels has a half hexagon mask at the top and the bottom, which produces roughly rectangular channels with rounded corners. As the mask is shaped in such a way that the outside of the channels match up to produce a stackable pattern. The geometry and mesh can be seen in figure (5.33).

The Evolution of the surface in this case is more complicated than previous EFAC cases. The surface evolution can be seen in figures (5.34), (5.35), (5.36) and (5.37). The surface starts flat then gradually grows under the lower part of the top mask, gradually rising upwards until it meets the top surface, from there it starts to coat the top surface until it has completely coated it. Once it has coated the stop surface the electrostatic force and surface tension on the polymer combined with the pressure gradients in the air moves the polymer at the edges to the left and the lower polymer downwards, eventually the surface reaches a steady state with a hollow in the centre of the polymer that is a rounded corner rectangle.

The electric field can be seen in figures (5.38), (5.39), (5.40) and (5.41). This follows a similar pattern to previous cases with the same deflections in the electric

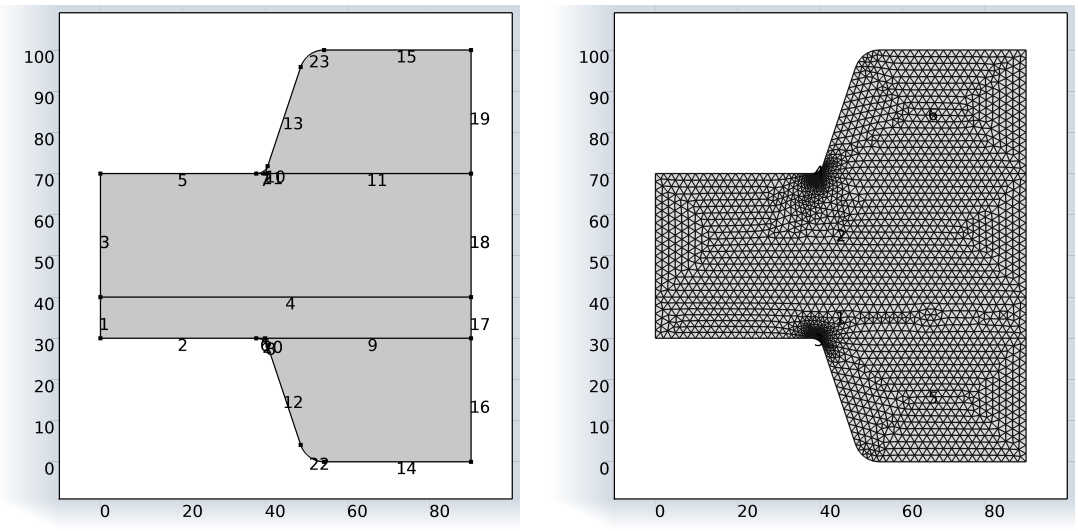

(a) Geometry **(b)** Mesh

Boundary	Electric Field	Fluid Flow
1	Zero Charge ($-\boldsymbol{n}\cdot\boldsymbol{D}=0$)	Symmetry ($\partial\boldsymbol{u}/\partial\boldsymbol{n}=0$)
2	Ground (0 V)	Slip Wall ($\boldsymbol{u}\cdot\boldsymbol{n}=0$)
3	Zero Charge ($-\boldsymbol{n}\cdot\boldsymbol{D}=0$)	Symmetry ($\partial\boldsymbol{u}/\partial\boldsymbol{n}=0$)
4		Initial Interface
5,7,10,13,15,23	500V	Wetted wall ($\theta=20°$)
6,8,9,12,14	Ground (0V)	Wetted wall ($\theta=20°$)
16,17,18,19	Zero Charge ($-\boldsymbol{n}\cdot\boldsymbol{D}=0$)	Symmetry ($\partial\boldsymbol{u}/\partial\boldsymbol{n}=0$)
20	500V	
21	500V	
22	Ground (0V)	Wetted wall ($\theta=20°$)

(c) Boundary Conditions

Figure 5.33: Geometry, mesh and boundary conditions for an EFAC case with a symmetrical "'hexagonal"' mask. Axis units in μm

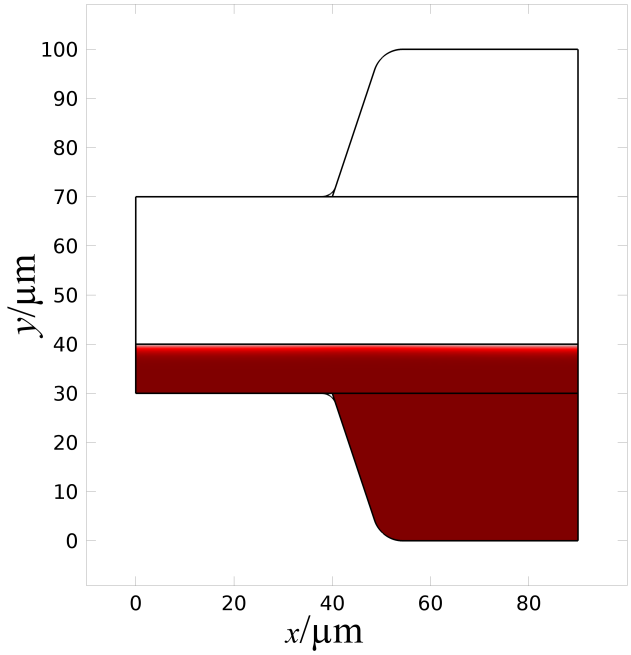

(a) 0.001s

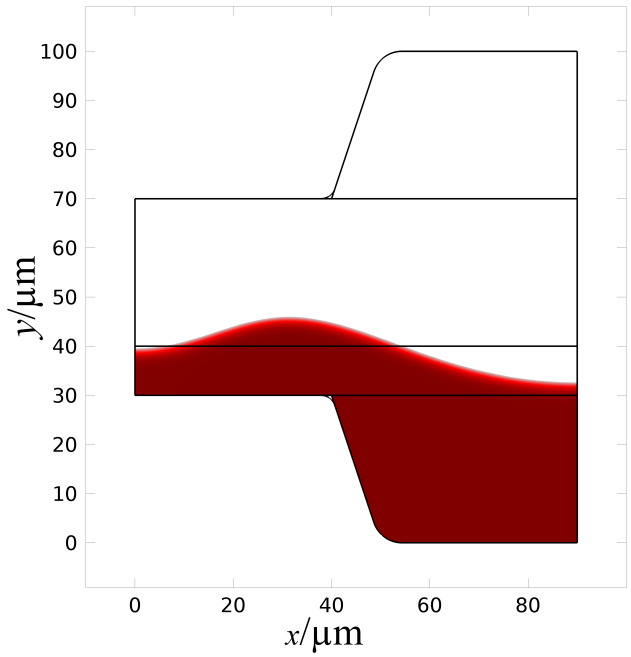

(b) 0.022s

Figure 5.34: Evolution of the surface for an EFAC case with a symmetrical "hexagonal" mask.

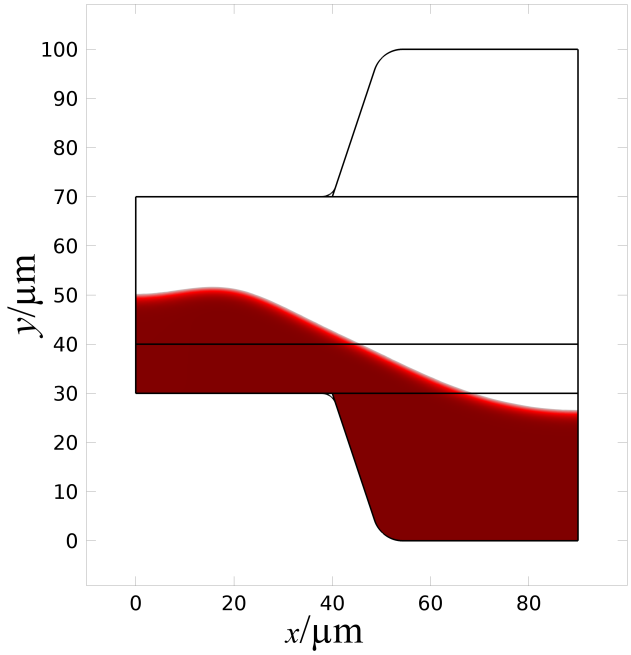

(a) 0.027s

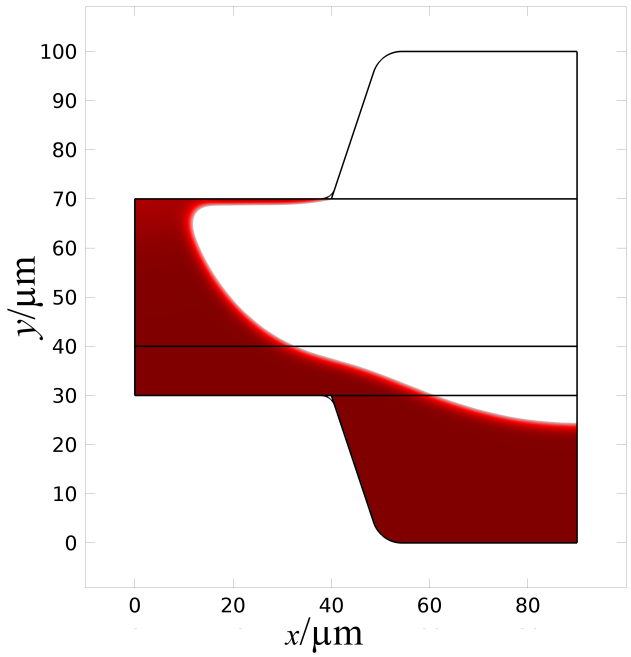

(b) 0.1s

Figure 5.35: Evolution of the surface for an EFAC case with a symmetrical "hexagonal" mask.

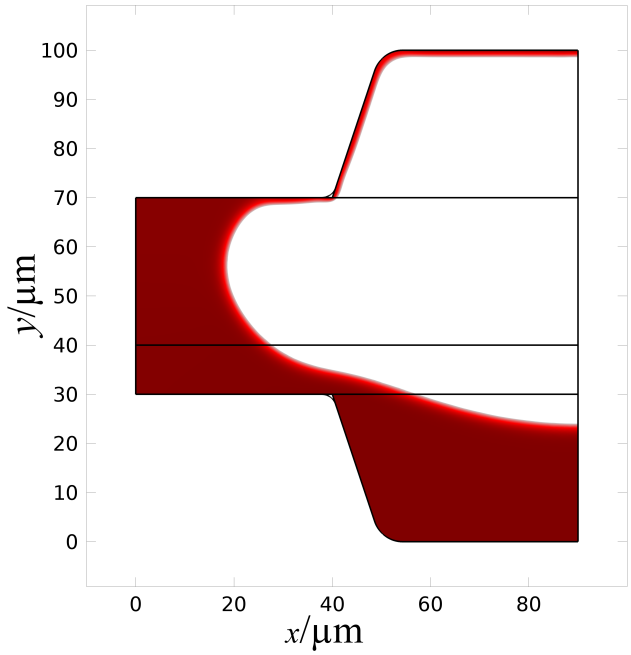

(a) 0.001s

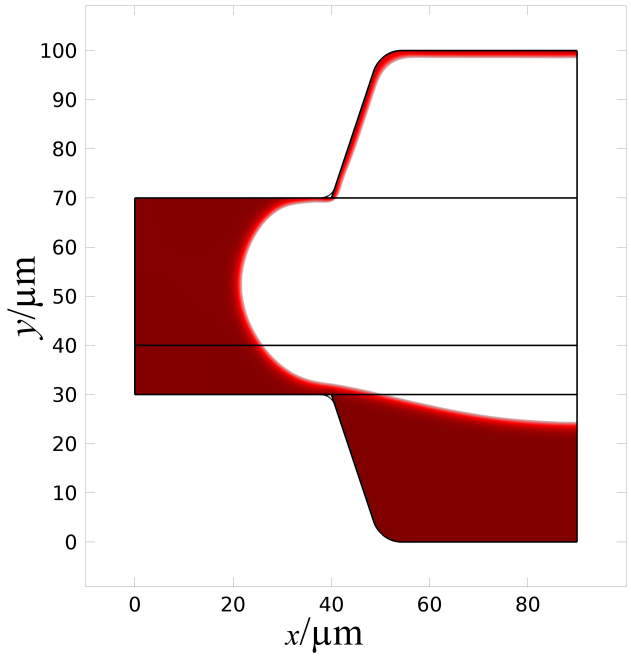

(b) 0.022s

Figure 5.36: Evolution of the surface for an EFAC case with a symmetrical "hexagonal" mask.

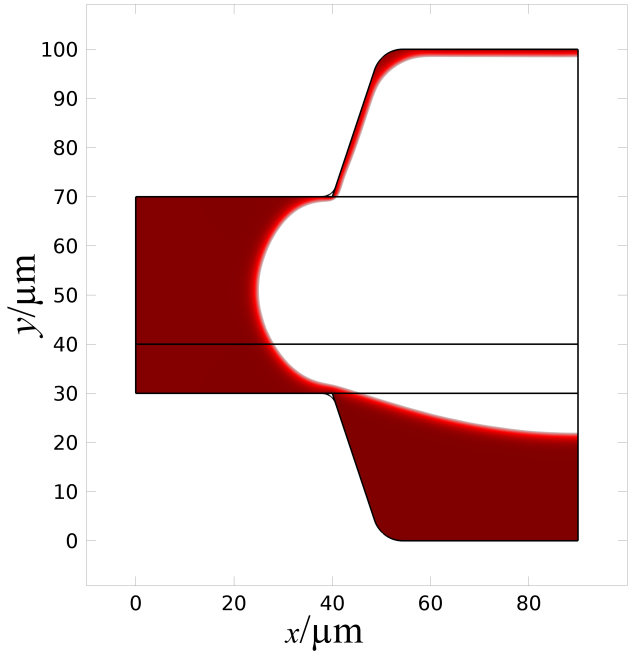

(a) 0.027s

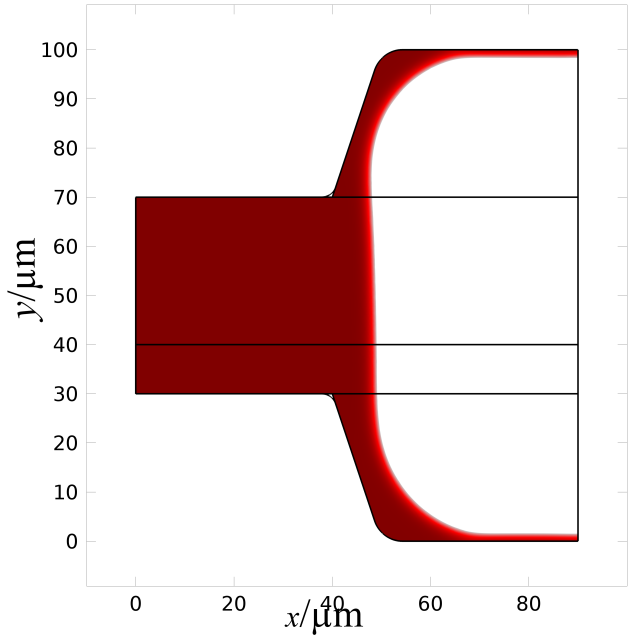

(b) 0.1s

Figure 5.37: Evolution of the surface for an EFAC case with a symmetrical "hexagonal" mask.

field at the interface.

Figure (5.42) shows how these channels can be stacked, with clever mask design this would enable various devices to be produced that don't rely on having a single layer of micro-channels, similarly the method has the potential to be used to create stackable micro-capsules for drug delivery.

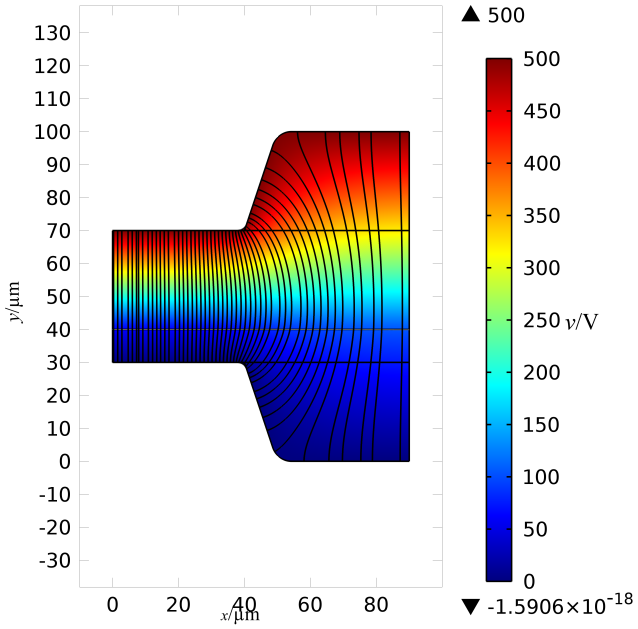

(a) 0.001s

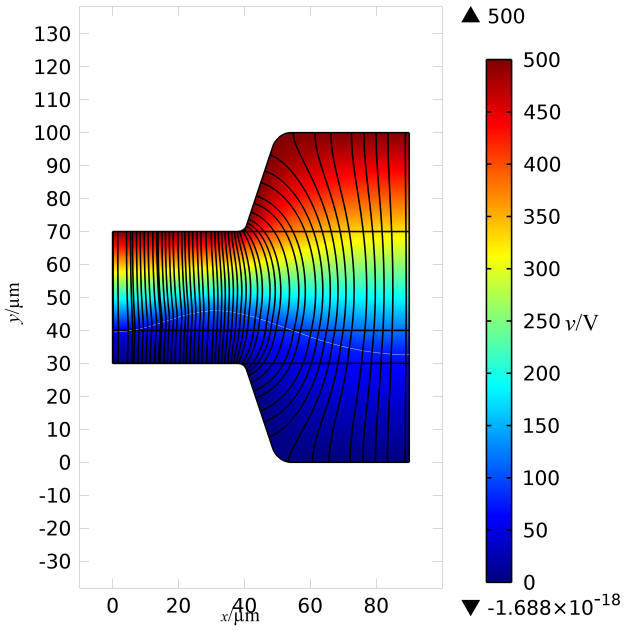

(b) 0.022s

Figure 5.38: Evolution of the electric field for an EFAC case with a symmetrical "hexagonal" mask.

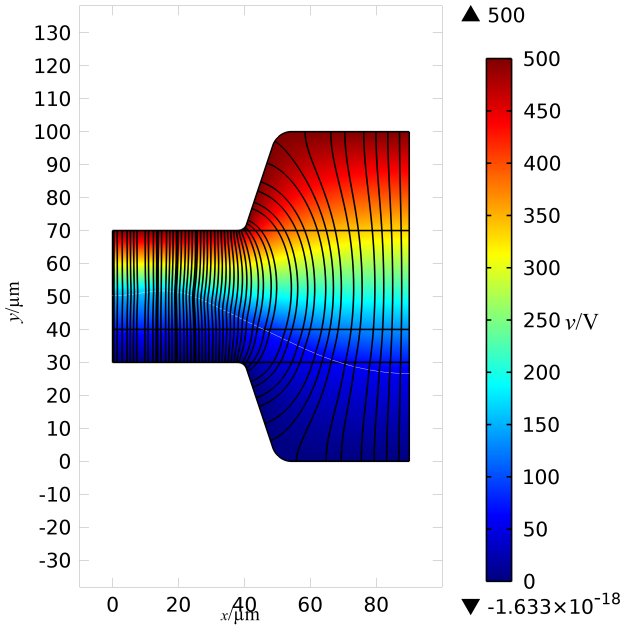

(a) 0.027s

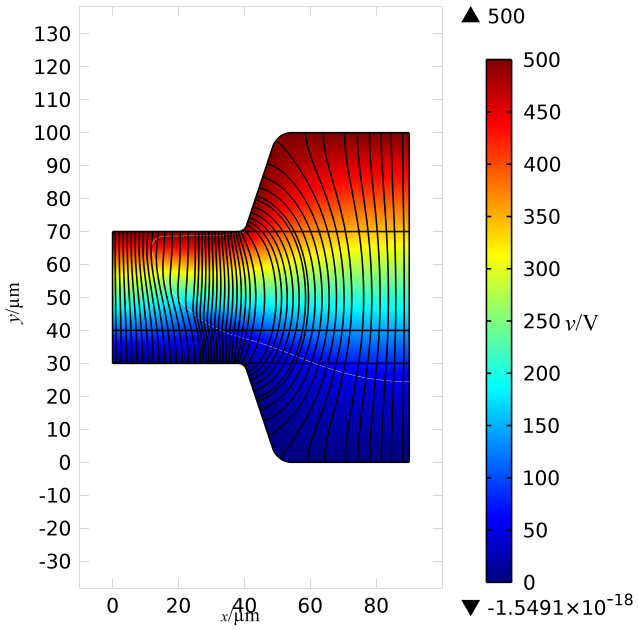

(b) 0.1s

Figure 5.39: Evolution of the electric field for an EFAC case with a symmetrical "hexagonal" mask.

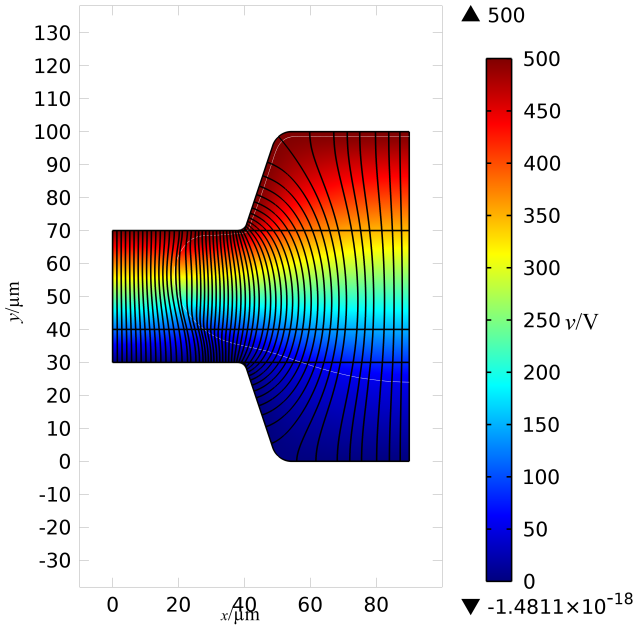

(a) 0.001s

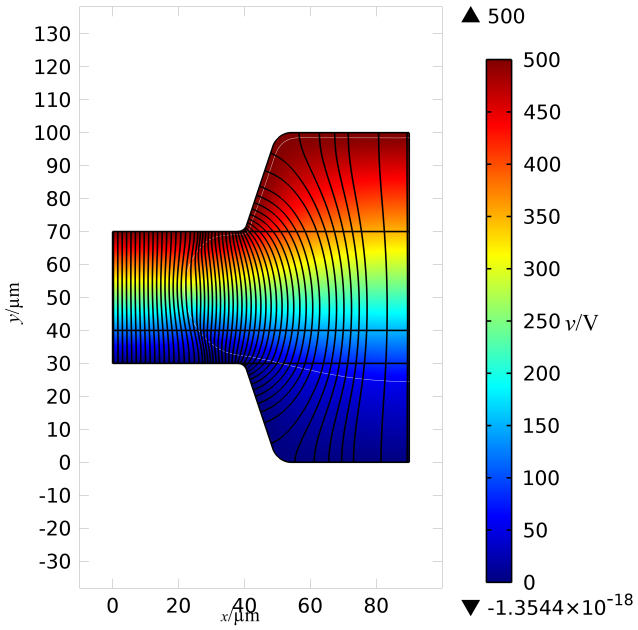

(b) 0.022s

Figure 5.40: Evolution of the electric field for an EFAC case with a symmetrical "hexagonal" mask.

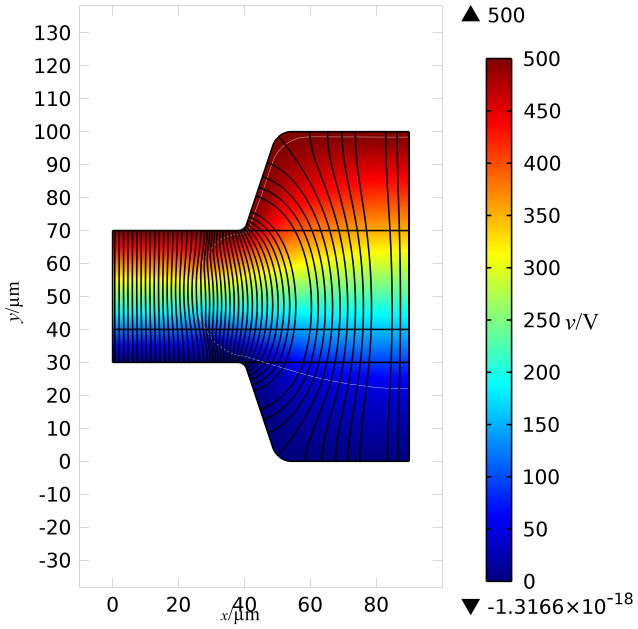

(a) 0.027s

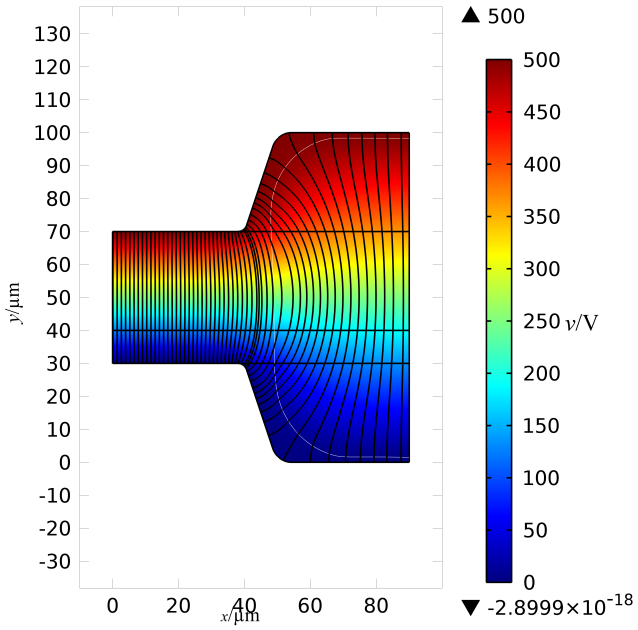

(b) 0.1s

Figure 5.41: Evolution of the electric field for an EFAC case with a symmetrical "hexagonal" mask,

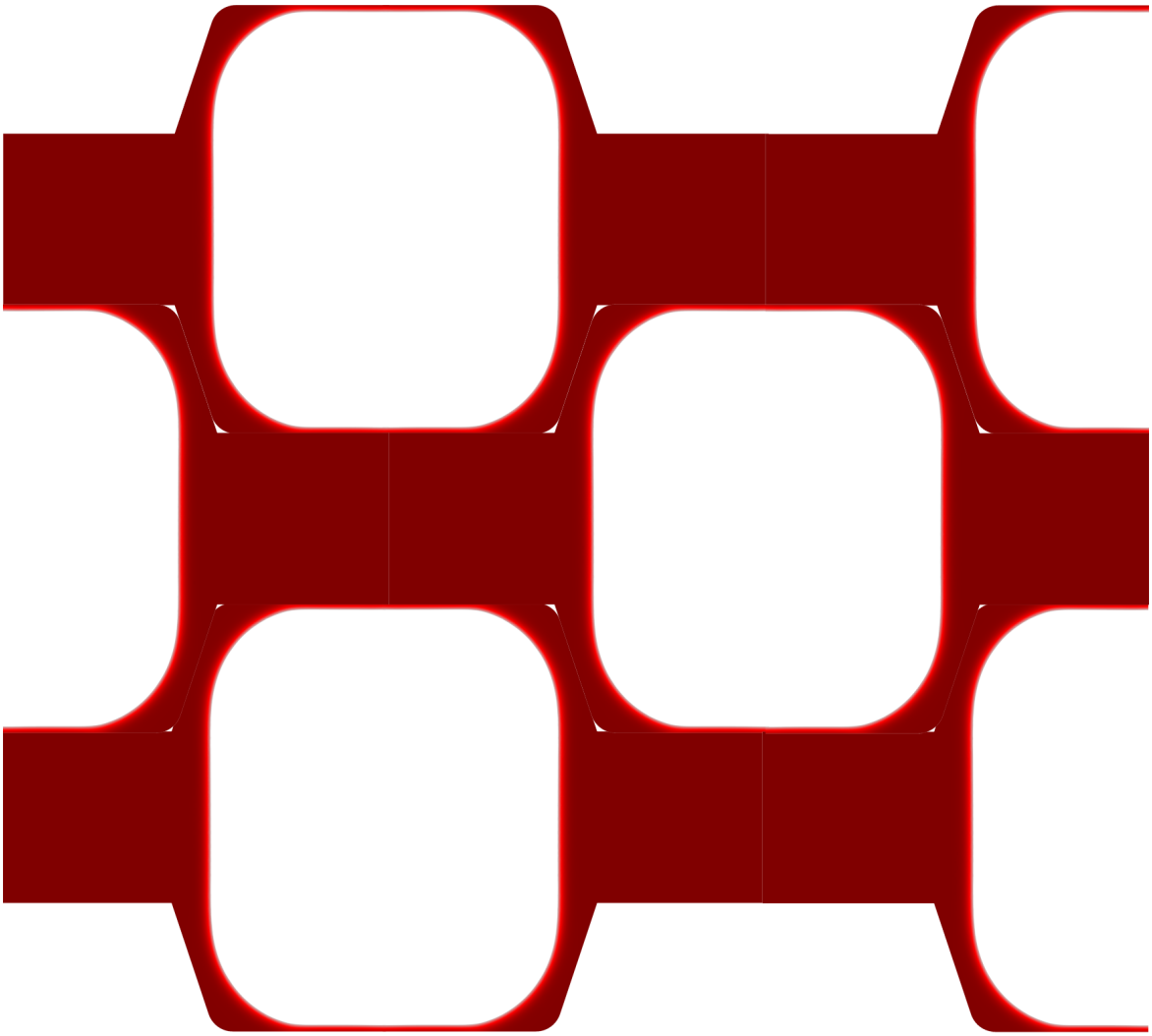

Figure 5.42: Effect of stacking the channels for the “hexagonal” mask.

5.4.4.2 Curved Mask

The Hexagonal mask however has some gaps so the stacking is not quite perfect, so a continuous curved top and lower mask was used. The geometry for this new mask can be seen in figure (5.43). As can be seen this is a symmetrical mask with heavily wetted surfaces and a potential difference of 500 V has been applied between them. The lower wetted surface of the mask enables the polymer to adhere to the mask thus not entirely depleting, tests done with similar masks but no wetted surface underneath resulted in an uncoated bottom surface.

The evolution of the surface of the polymer can be seen in figures (5.44) and (5.45) as can be seen the evolution is similar to the hexagonal mesh case resulting in a channel in the middle. There is still motion in the final frame of this case so it is likely that the internal channel will continue to change shape until it becomes symmetrical leaving a symmetrical channel.

The evolution of the electric field in this case shown in figures (5.46) and (5.47) is similar to previous cases with the deflection of the electric field at the interface due to the change in dielectric properties.

The effect of stacking the geometries can be seen in figure (5.48) this method would provide a regular array of channels. These channels could then be used to produce micro-filters or for applications where multiple layers of microchannels are needed.

5.5 Summary

A range of results have been presented here for different geometries for both EHDIP and EFAC cases for differing geometries. The results demonstrate channels produced

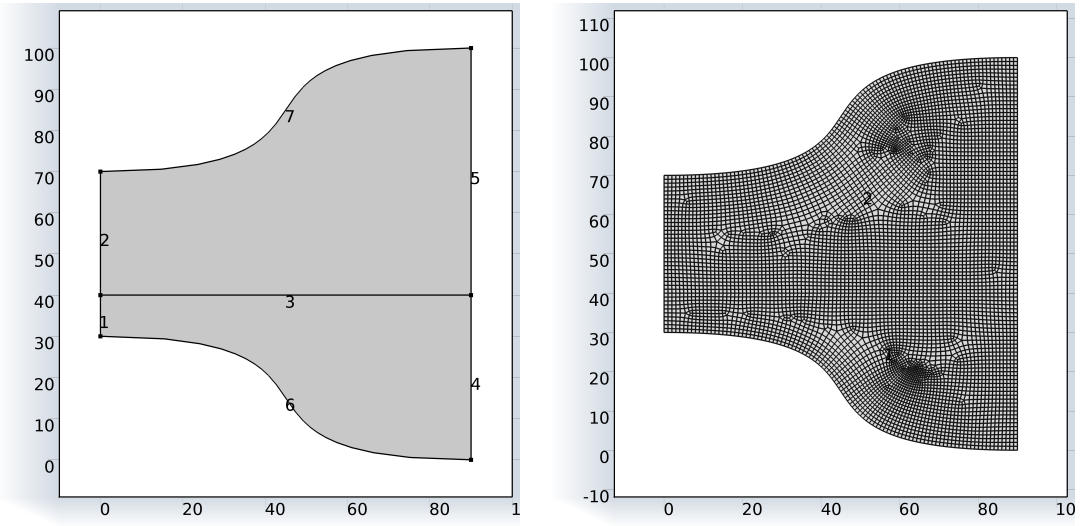

(a) Geometry **(b)** Mesh

Boundary	Electric Field	Fluid Flow
1	Zero Charge ($-\boldsymbol{n} \cdot \boldsymbol{D} = 0$)	Symmetry ($\partial \boldsymbol{u}/\partial \boldsymbol{n} = 0$)
2	Zero Charge ($-\boldsymbol{n} \cdot \boldsymbol{D} = 0$)	Symmetry ($\partial \boldsymbol{u}/\partial \boldsymbol{n} = 0$)
3		Initial Interface
4	Zero Charge ($-\boldsymbol{n} \cdot \boldsymbol{D} = 0$)	Symmetry ($\partial \boldsymbol{u}/\partial \boldsymbol{n} = 0$)
5	Zero Charge ($-\boldsymbol{n} \cdot \boldsymbol{D} = 0$)	Symmetry ($\partial \boldsymbol{u}/\partial \boldsymbol{n} = 0$)
6	Ground (6V)	Wetted wall ($\theta = 20°$)
7	500V	Wetted wall ($\theta = 20°$)

(c) Boundary Conditions

Figure 5.43: Geometry, mesh and boundary conditions for an EFAC case with a symmetrical curved mask. Axis units in μm

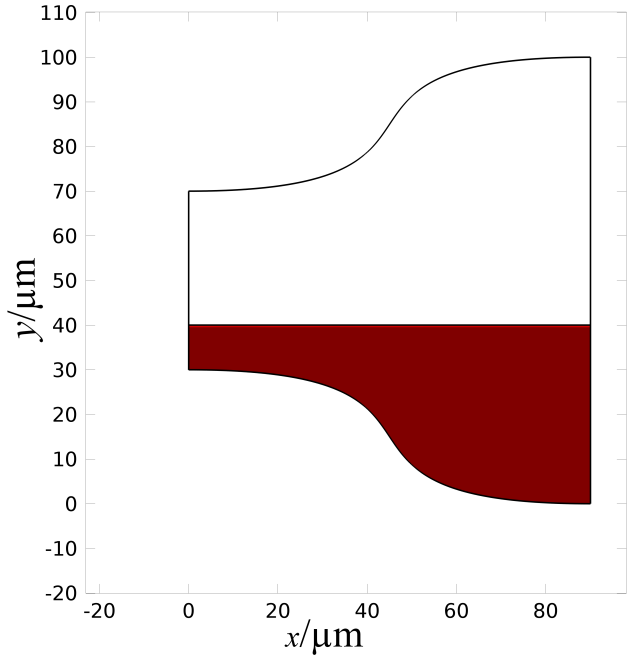

(a) 0.001s

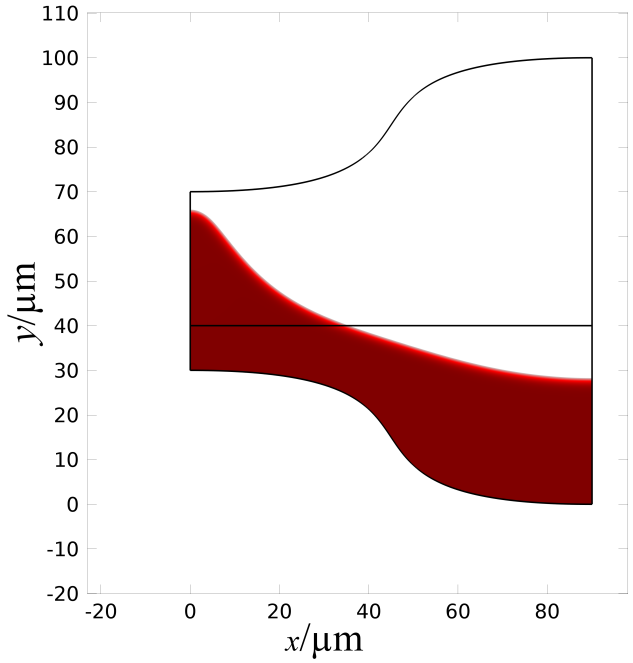

(b) 0.022s

Figure 5.44: Evolution of the surface for an EFAC case with a symmetrical curved mask.

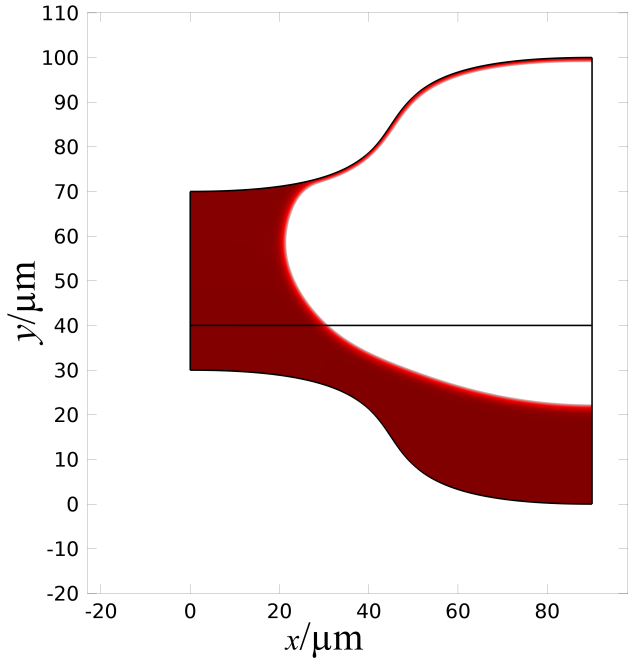

(a) 0.027s

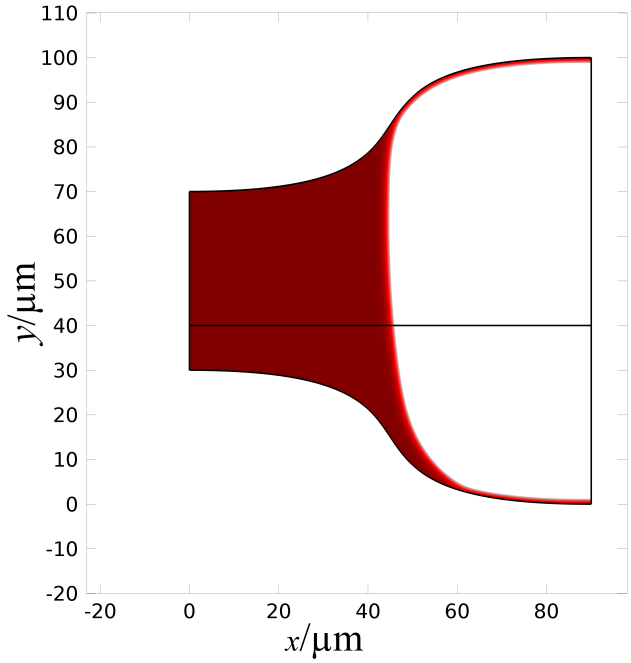

(b) 0.1s

Figure 5.45: Evolution of the surface for an EFAC case with a symmetrical curved mask.

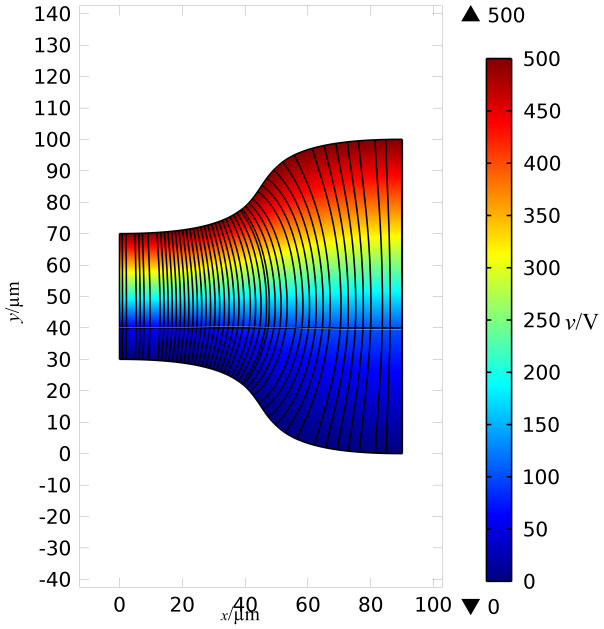

(a) 0.001s

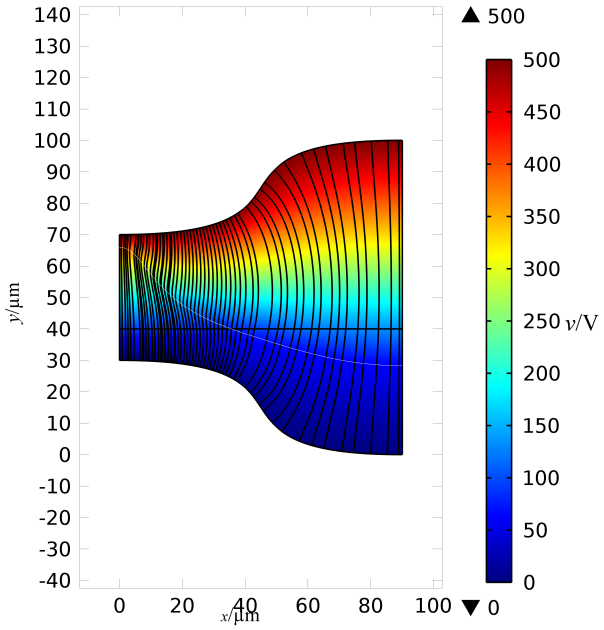

(b) 0.022s

Figure 5.46: Evolution of the electric field for an EFAC case with a symmetrical curved mask.

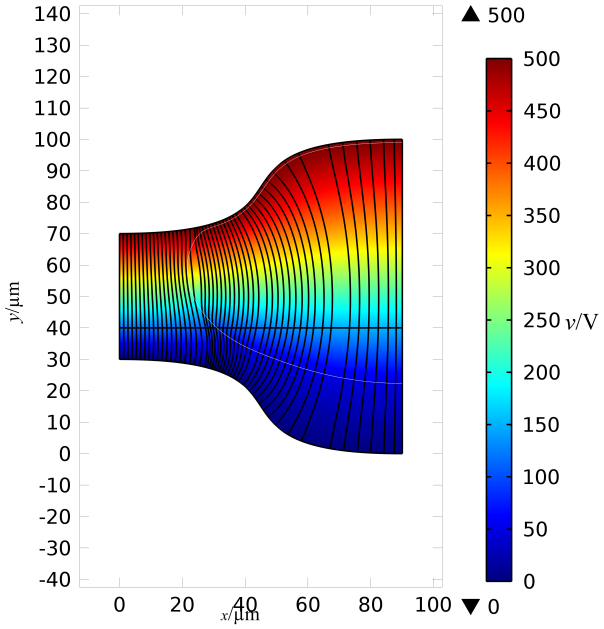

(a) 0.027s

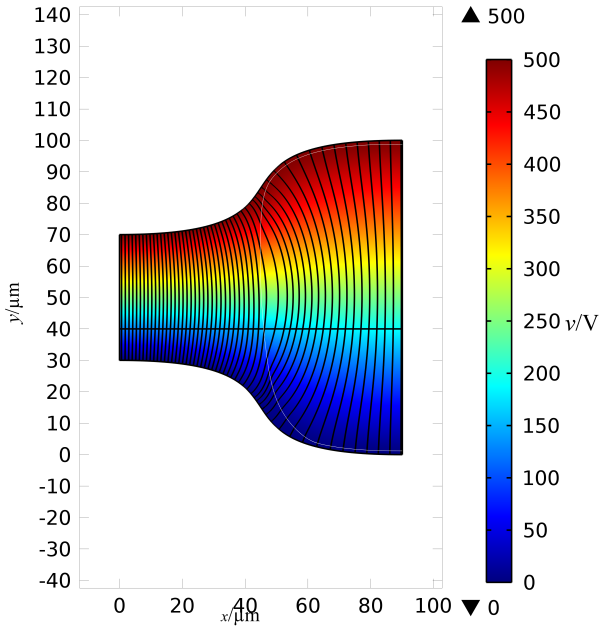

(b) 0.1s

Figure 5.47: Evolution of the electric field for an EFAC case with a symmetrical curved mask.

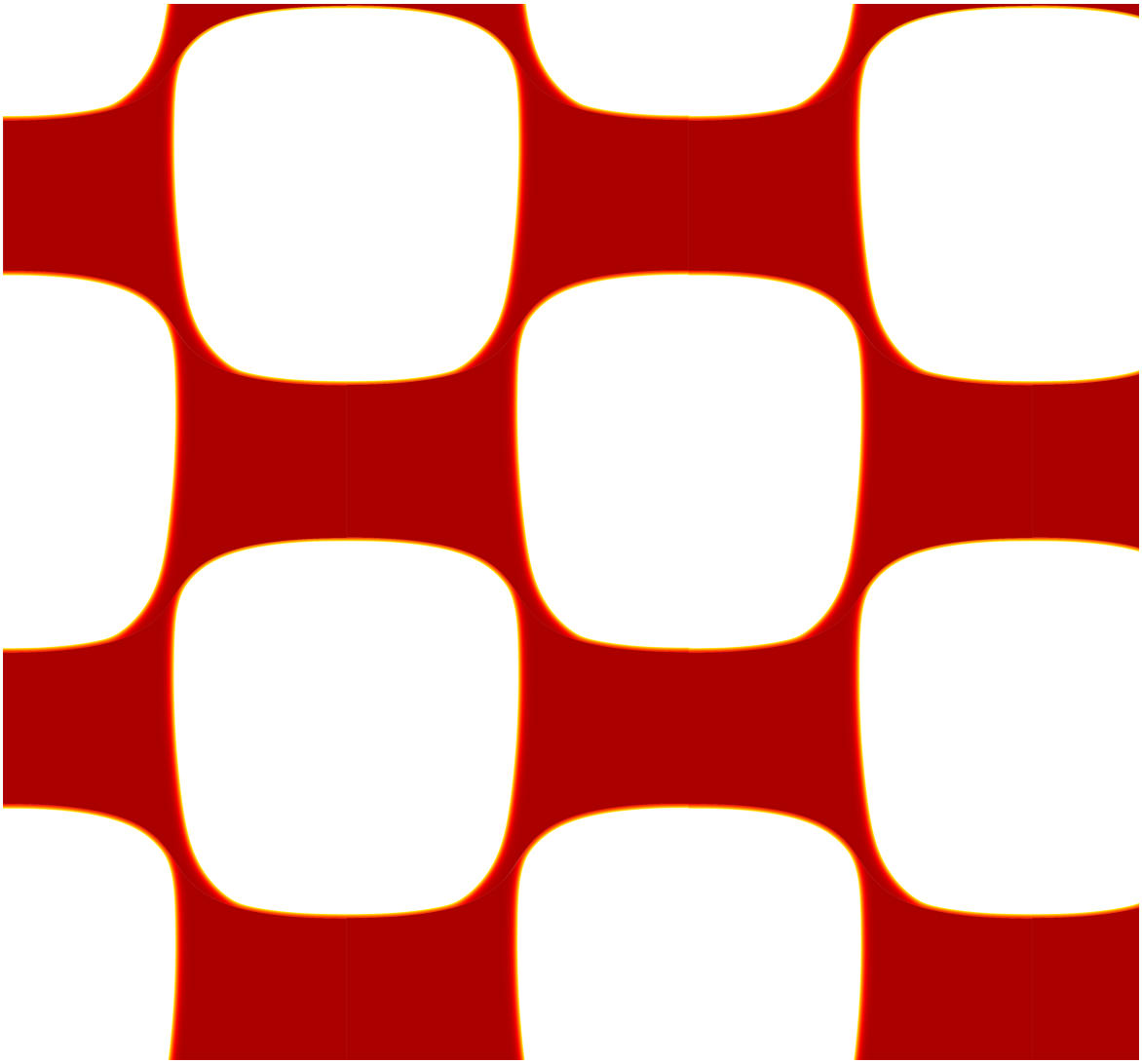

Figure 5.48: Effect of stacking the channels for the curved mask.

through the process. As the model is two-dimensional the work here has been for microchannels, however the processes can be used to create a wide range of different microstructures. The masks presented here are example masks and wide range of masks would be able to be used for the process, however time constraints meant that the number of masks that could be tested was limited. Therefore both curved and angled masks were simulated to show the differences in using these shapes.

The extension of the processes to using two shaped masks rather than just one is new to the field. It was an idea the author proposed and tested with the model. However further experiments on this would be advantageous to see if it works experimentally.

Chapter 6

PROCESS SENSITIVITY

6.1 Introduction

In the previous chapter results from various mask shapes were considered, these mask shapes are the primary method of controlling the final shapes obtained from the modelling. However they are not the only factor to be considered as material properties, distances and voltages may also be altered. In this chapter this is considered along with the effect of making minor alterations on one of the masks in the previous section in an attempt to see the limits of the EFAC process.

The two material properties that were investigated where the contact angle and the permittivity of the polymer. The contact angle was considered as changing this alters the capillary force in the final stages of the process. The permittivity of the polymer was modelled to look at its effects on the surface morphology. This was likely to have a small effect as the magnitude of the dielectric forces are related to the differences in the relative permittivities between the polymer and the air.

In addition to changing the material properties the effect of changing two dimen-

sional quantities was considered firstly changing the air gap between the polymer-air interface and the top mask and secondly changing the thickness of the polymer melt. These were selected as they both have an effect on the final surface morphology based on the initial problem.

The mask shape was considered looking at the effect of changing the sharpness of a corner of the mask. This was considered as the corners on the mask were rounded partially to avoid singularities in the electric field, but also to enable the polymer to flow smoothly round the corners. However an arbitrary radius was selected for these rounded corners so a study was done to see how tight this radius could be.

Finally the effect of changing the voltage on the top mask was considered, as the electric field strength is proportional to this when the domain size is kept constant. As the dielectric force is proportional to the square of the electric field, a small change in this voltage should create a different surface morphology.

6.2 Contact Angle

Changing the contact angle appears to have the effect of changing the thickness of the top polymer shell. This is likely due to the reduced capillary force caused by the reduced surface adhesion that corresponds to a smaller contact angle. This reduced force means that less of the polymer is able to be "pulled" upwards by the capillary force causing less of a coating of the top mask. Figure (6.1) shows the effect of changing the contact angle. The 10 degree contact angle has a slightly thicker top shell than the 20 degree case, also the 25 degree case has been unable to form a full shell due to the reduced capillary force present meaning there is not enough force to fully coat the top mask.

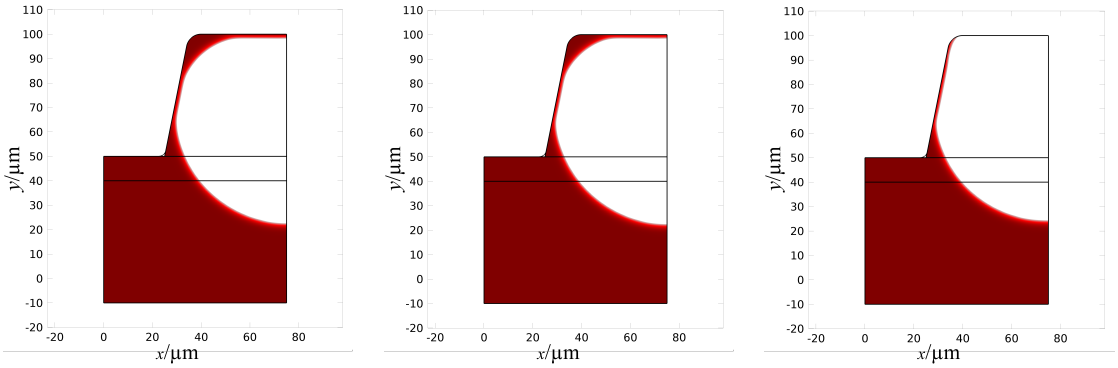

(a) 10°s, Works **(b)** 20°, Works **(c)** 25°, Failure

Figure 6.1: Comparison between different contact angles on the top mask.

Changing the contact angle between the polymer and the top mask can so be used for tuning the thickness of the top shell to make it thicker or thinner. In these cases the 10° contact angle results in a thickness of 2.1 µm; compared to 1.5 µm for a 20° contact angle; and 1.4 µm for a 25° contact angle. The very thin cases would be prone to breaking very easily, however this shows that they can be made thicker by increasing how heavily wetted the top surface is.

6.3 Polymer Permittivity

The polymer permittivity was investigated to see the effect of using different polymers in the process. Different polymers usually have different permittivities and so the viability of this process partially depends on its sensitivity to the material permittivities. In this case an extra two cases were run, one with the polymer with a very low permittivity (the same as air) and another with double the permittivity for the other cases considered. Therefore there are results for the same mask for relative permittivities of 1, 2.5 and 5.

Due to the formulation of the surface force the case with a permittivity of 1 is a

trivial case as there is no change of permittivity at the interface there is no dielectric force and so the polymer surface should remain flat. As can be seen from the results in figures (6.2) and (6.3) this is clearly the case. At 0s the surface is flat and at each additional image.

The comparison between relative permittivities of 2.5 and 5 is more illuminating, they can be seen in figures (6.4), (6.5), (6.6) and (6.7). In both cases the surface starts off flat at 0s. However by the time the polymer has reached the top mask for the relative permittivity of 5 (0.004s) it is still growing upwards for the permittivity of 2.5. Once the polymer has reached the top mask for the lower permittivity (0.03s) for the cases with the higher permittivities the top mask has been completely coated already. And the final shape (0.1s) is slightly different for both polymers, this can be seen more clearly in a comparison between all surfaces at the end of the simulation in figure (reffig:freesurfacepermcomparison0.1s).

A comparison of the electric fields in these cases can also be seen in figures (6.9) and (6.10). Due to the increase in the difference in the permittivities between the polymer and the air, the amount the electric field deflects when it crosses the air-polymer interface increases as the permittivity does. This results in the increased dielectric forces which are seen by the change in the final shape of the polymer and also by the increased speed of the polymer.

These simulations show that the speed of the process may be controlled by the changing of the permittivity of the polymer, however this also has an effect on the final shape of the polymer obtained as the increased dielectric forces mean that the surface tension forces will not be as dominant.

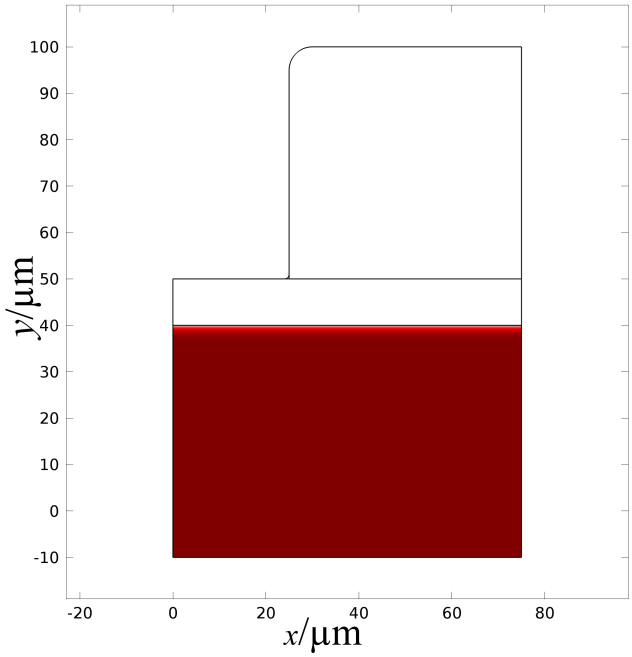

(a) 0s

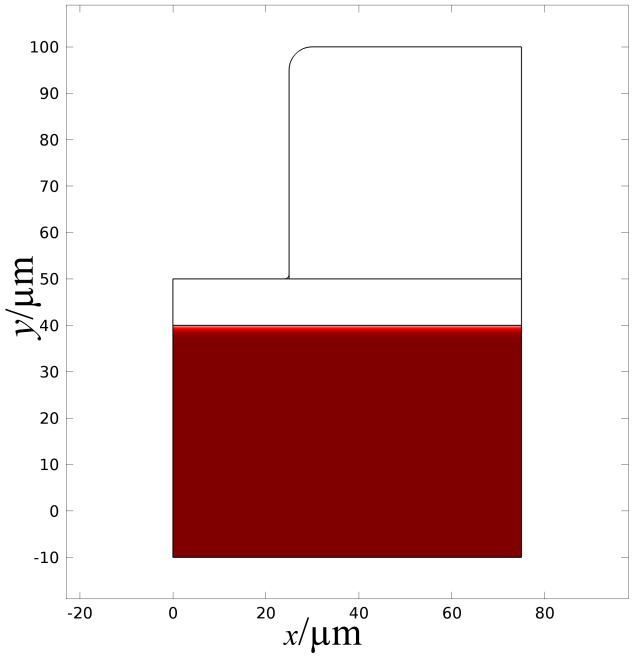

(b) 0.004s

Figure 6.2: Free surface at different times for a case with a relative permittivity of 1.

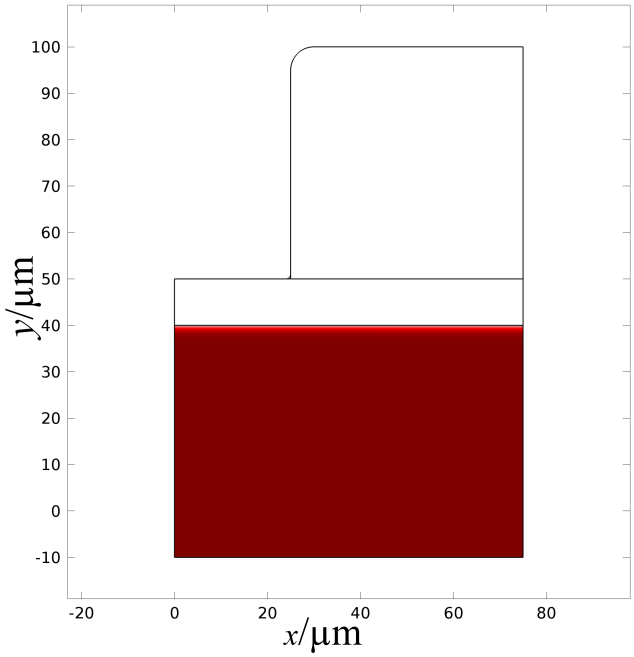

(a) 0.03s

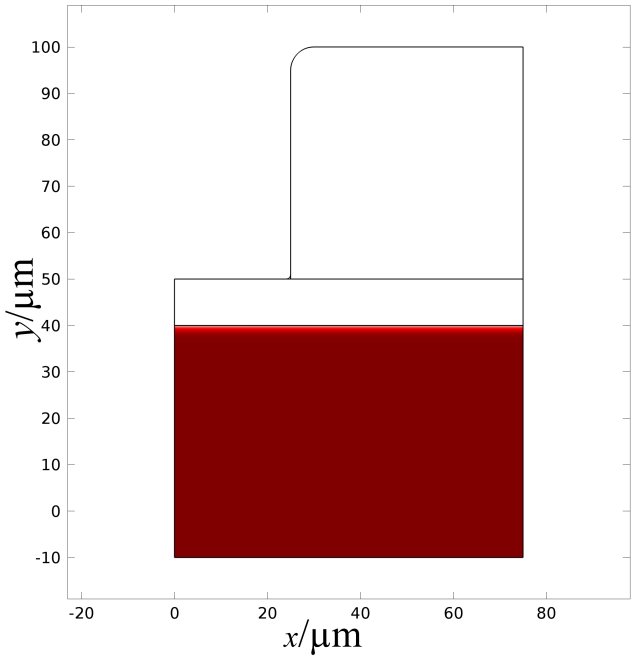

(b) 0.1s

Figure 6.3: Free surface at different times for a case with a relative permittivity of 1.

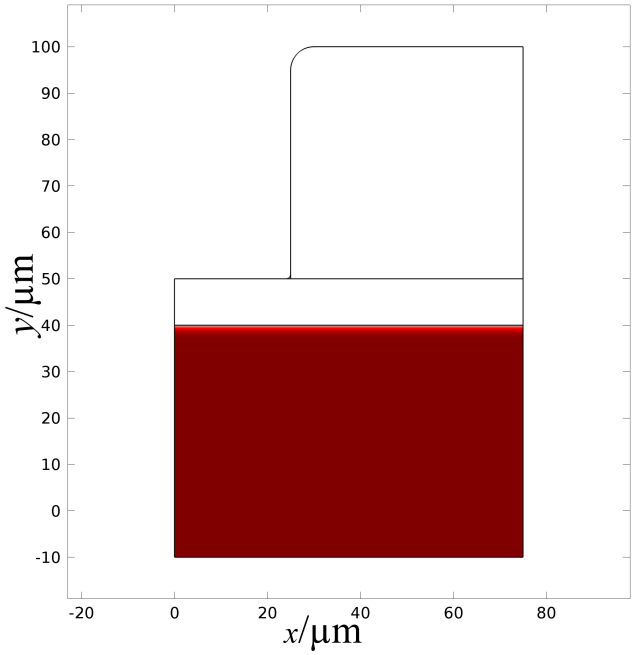

(a) ϵ_r=2.5

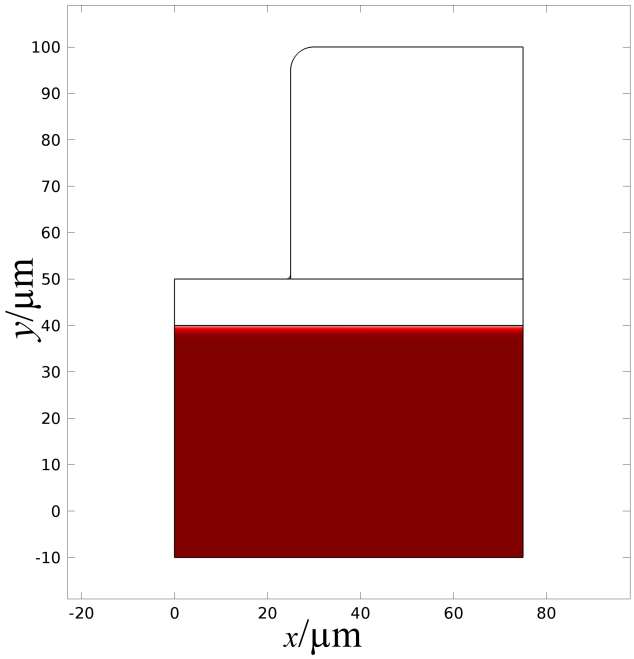

(b) ϵ_r=5

Figure 6.4: Free surfaces at 0s with a relative permittivities of 2.5 and 5.

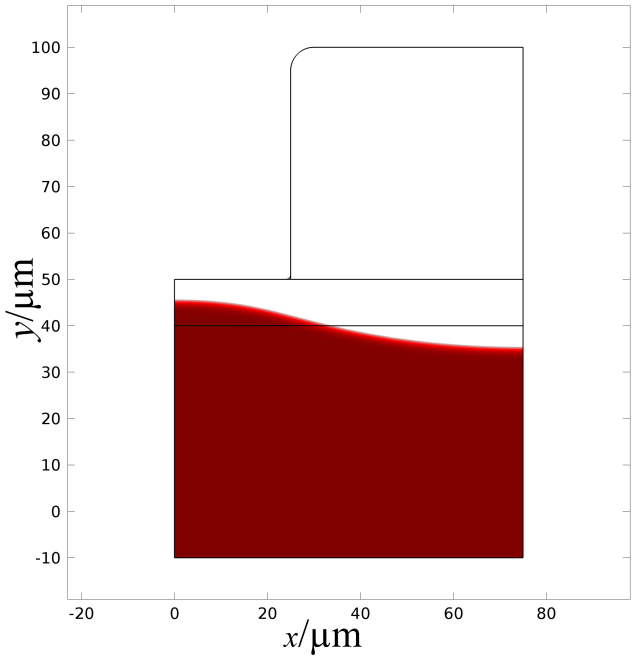

(a) ϵ_r=2.5

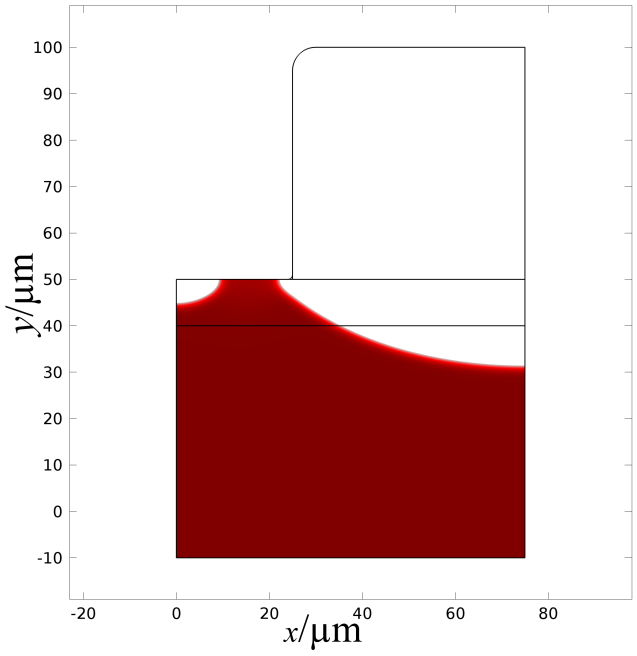

(b) ϵ_r=5

Figure 6.5: Free surfaces at 0.004s with a relative permittivities of 2.5 and 5.

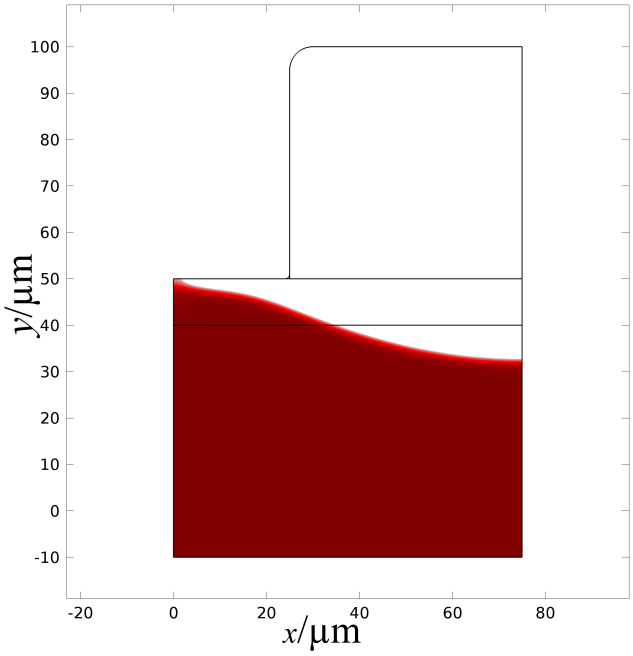

(a) ϵ_r=2.5

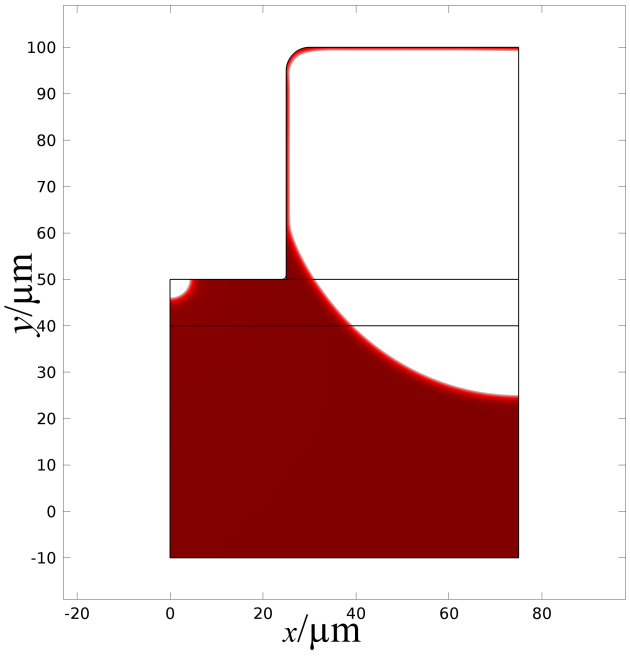

(b) ϵ_r=5

Figure 6.6: Free surfaces at 0.03s with a relative permittivities of 2.5 and 5.

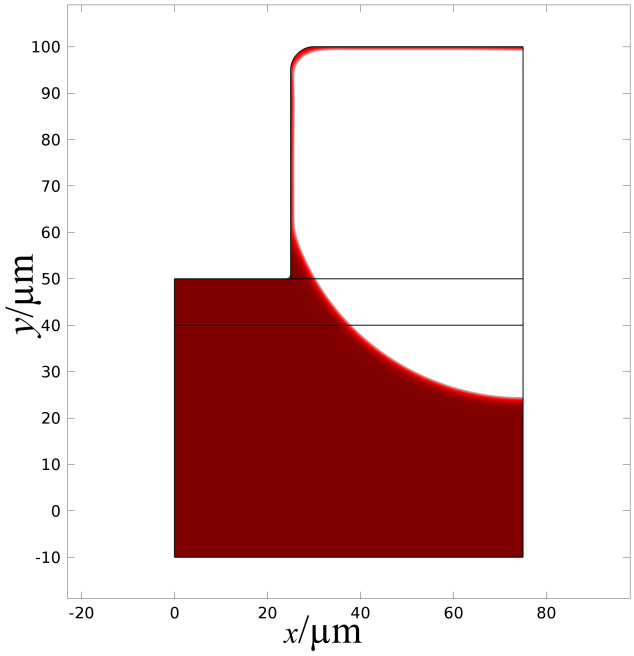

(a) ϵ_r=2.5

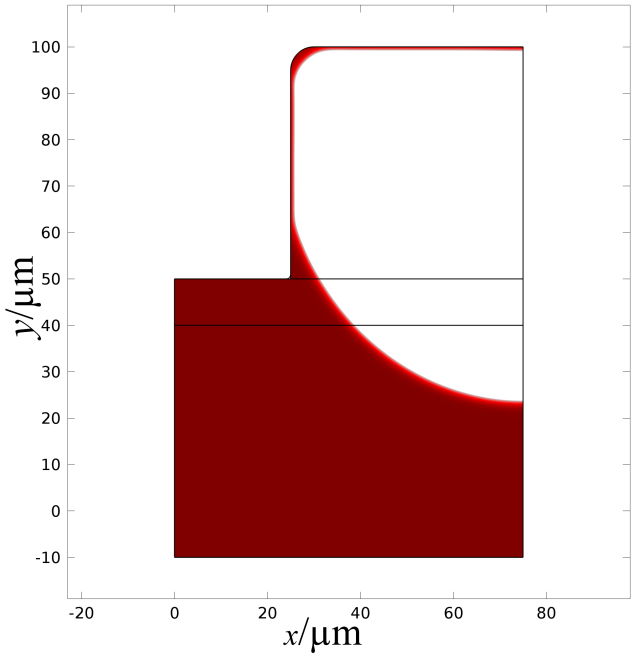

(b) ϵ_r=5

Figure 6.7: Free surfaces at 0.1s with a relative permittivities of 2.5 and 5.

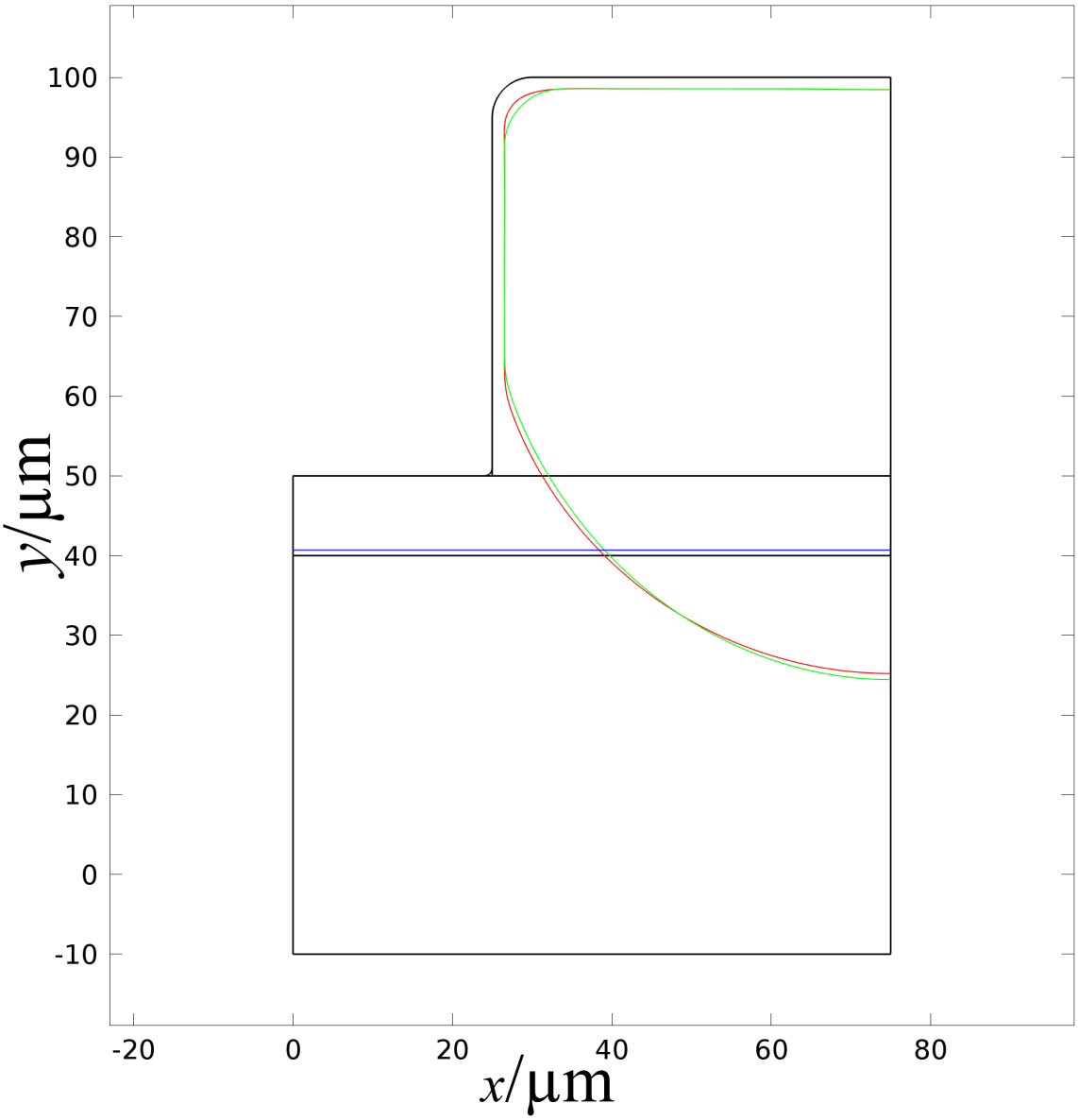

Figure 6.8: Free surfaces at the end of the simulation for permittivities of 1 (Blue), 2.5 (Red) and 5(Green).

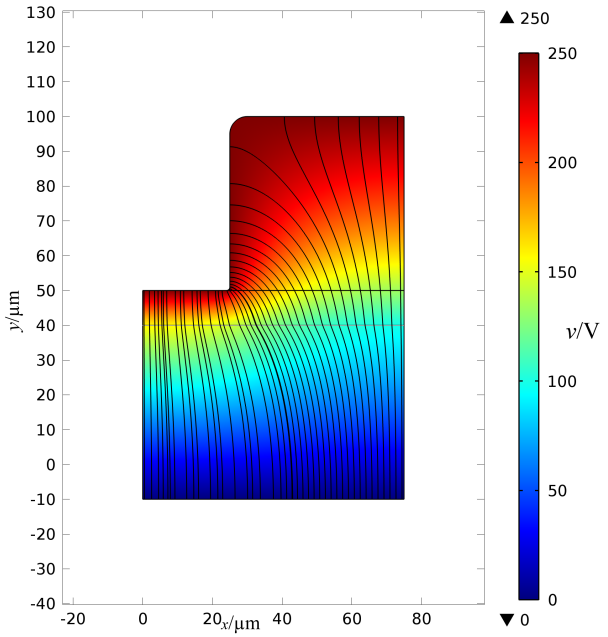

(a) ϵ_r=2.5

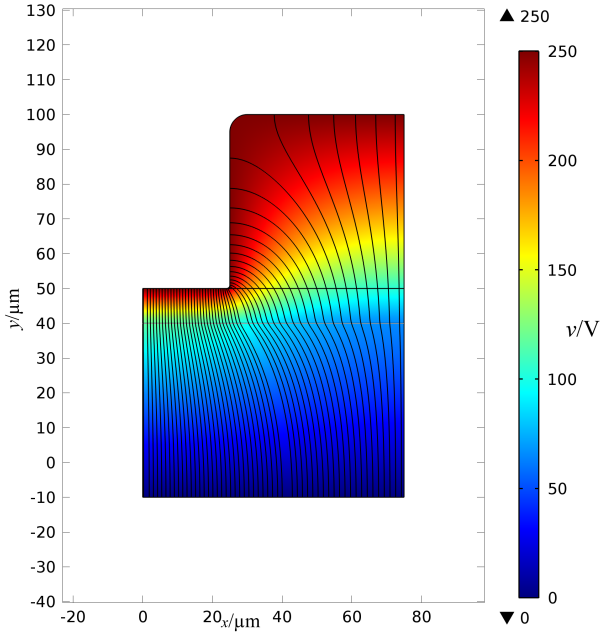

(b) ϵ_r=5

Figure 6.9: Electric fields at 0s with a relative permittivities of 2.5 and 5.

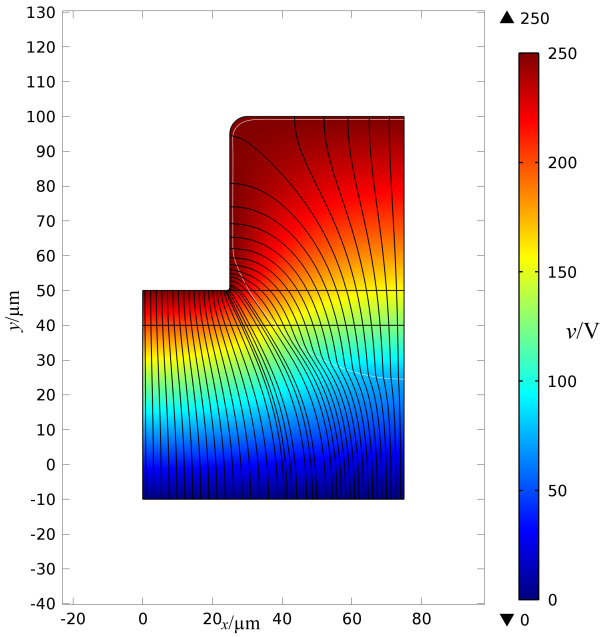

(a) ϵ_r=2.5, 0.1s

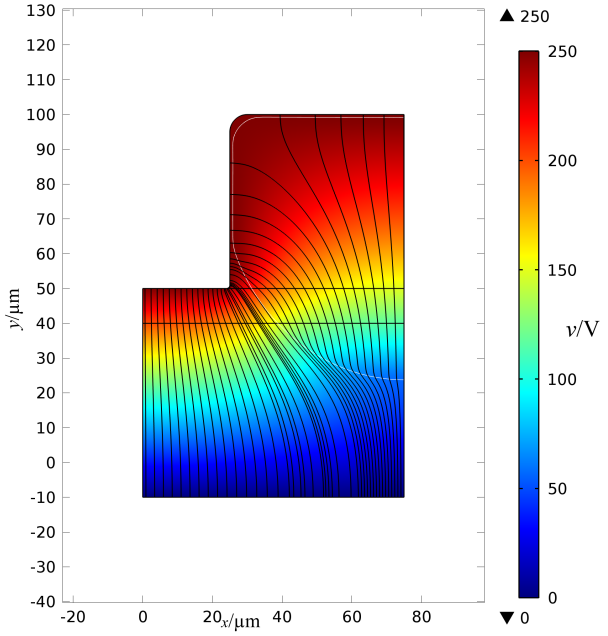

(b) ϵ_r=5, 0.1s

Figure 6.10: Electric fields at 0.1s with a relative permittivities of 2.5 and 5.

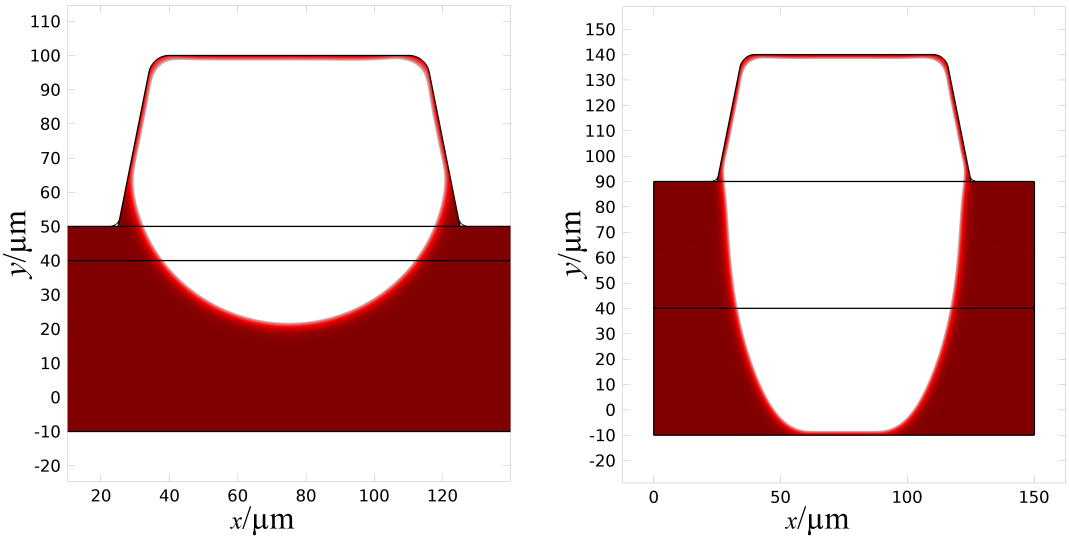

(a) 10 μm Air Gap **(b)** 50 μm Air Gap

Figure 6.11: Comparison between different air gaps.

6.4 Air Gap

Increasing the air gap allows larger channels to be produced with the same amount of material. This gives deeper channels of the similar width. With a larger air gap it is possible to almost deplete the lower region of the polymer unless there is the same heavily wetted surface on the bottom mask. Figure (6.11) shows the effect of increasing the air gap. A larger channel is produced compared to a smaller air gap and there is now a flat bottom to the channel. The only caveat with this flat bottom to the channel is that it is also very thin like that of the top mask. Increasing the polymer thickness at the same time as the air gap would avoid this problem and create a deeper channel with the same width.

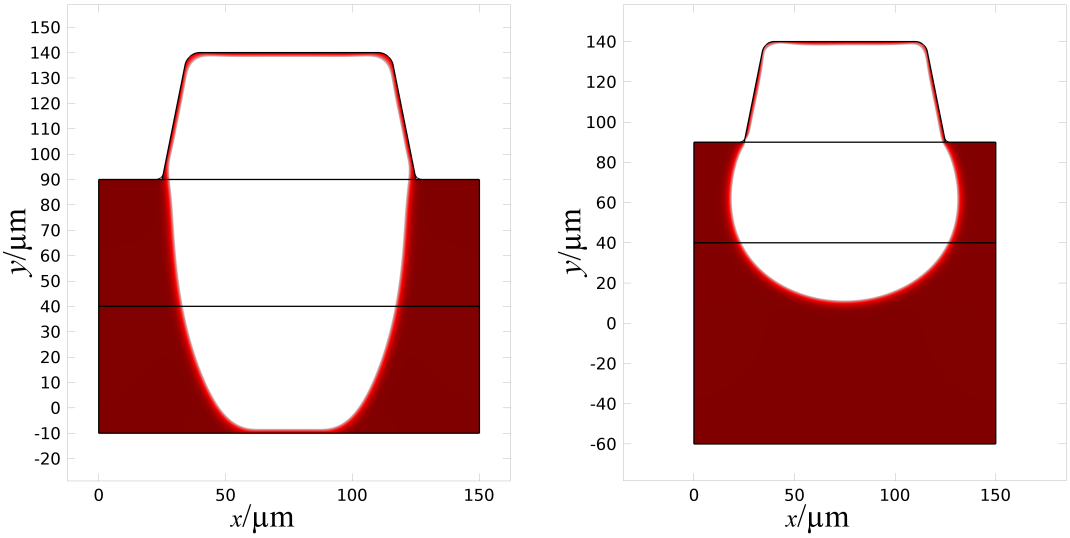

(a) 50 µm thick polymer **(b)** 100 µm thick polymer

Figure 6.12: Comparison between different initial polymer thickness.

6.5 Polymer Thickness

In increasing the polymer thickness different shapes are possible in the lower part of the polymer. Figure (6.12) shows the effect of changing the polymer thickness the first of these images is the same as the previous figure, the second however has an increased polymer thickness. This increased polymer thickness causes a different final shape in the polymer. This shape would not be very useful for manufacturing microchannels. This means that the polymer thickness would have to be tightly controlled were the process to be used as a manufacturing technique.

6.6 Mask Shape

Though large changes of mask shape were considered in the previous chapter, smaller differences were not looked at. To this end the effect of decreasing the radius of the

curve in the top left corner of the "square" mask was considered. This was considered important as the curve in the top corner was added for two reasons. Firstly right angles for the prescribed voltages cause infinite gradients of the voltage this causes the electric field be infinite at these points. This would cause an infinite force at these points. In reality it is not possible to manufacture a perfectly square mask and so the decision was made to curve the corner to avoid this problem. Rounding the corner also had the added benefit of allowing the polymer to flow more smoothly under the capillary force.

The results for these cases can be seen in figures (6.13), (6.14), (6.15) and (6.16). For the earlier time-steps there was very little differences in these cases until the mask was reached. At this stage slight differences in the electric field caused by the change in the corner seem to have effected the ability to coat the top mask with the polymer. This would be a problem as the shapes produced would not be usable.

The electric fields for these cases can be seen in figures (6.17), (6.18), (6.19) and (6.20). The sharper corner does result in an increased electric field in the corner, however it has very little effect on the electric field at the initial surface of the polymer. But the electric field in the top half of the mask seems to have changed significantly enough to retard the growth of the polymer along the top mask. This would benefit from further investigation.

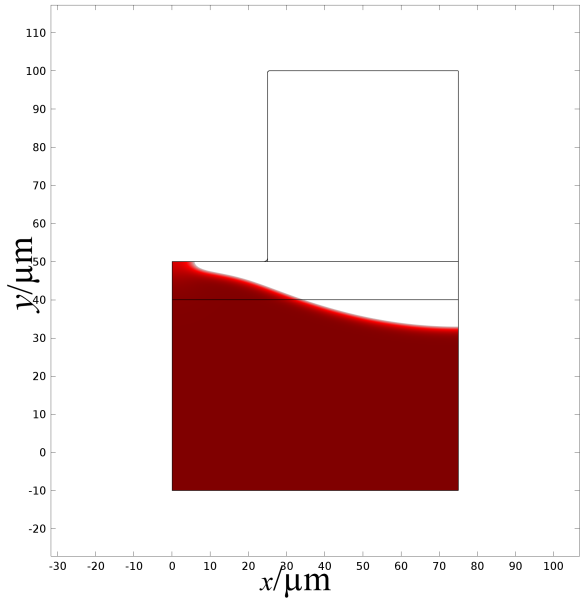

(a) Corner radius= 0.5 µm

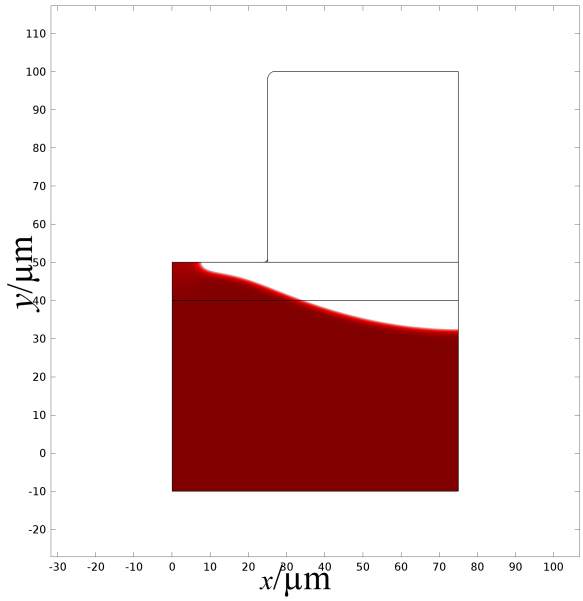

(b) Corner radius= 2 µm

Figure 6.13: Free surface at the point where the polymer touches the mask for different corner radii.

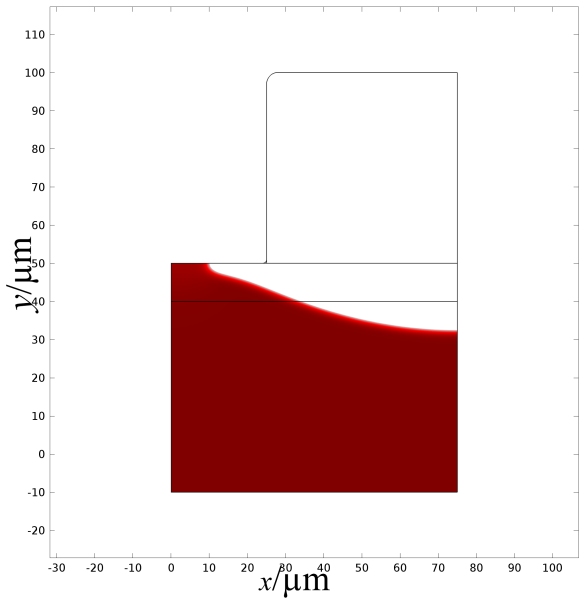

(a) Corner radius= 3 µm

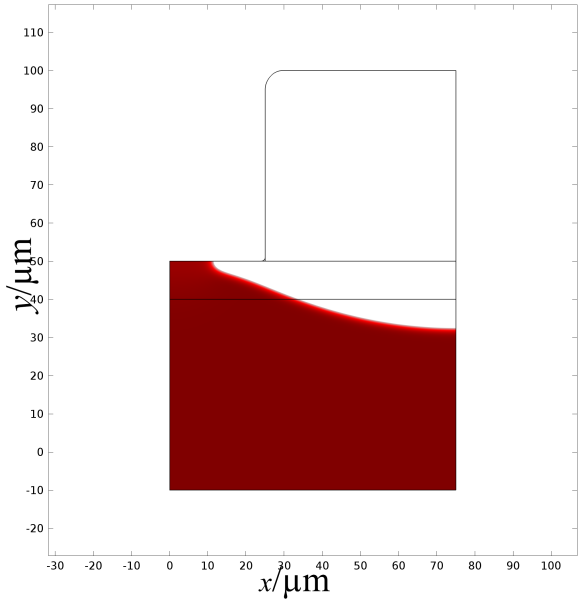

(b) Corner radius= 5 µm

Figure 6.14: Free surface at the point where the polymer touches the mask for different corner radii.

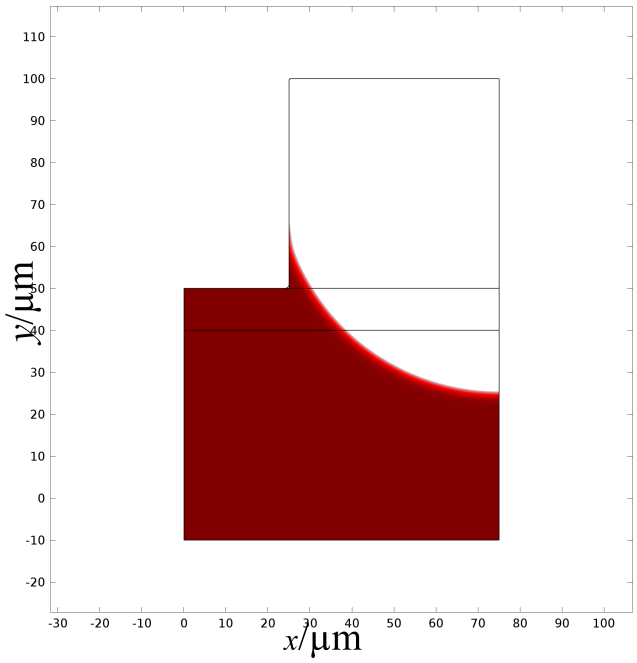

(a) Corner radius= 0.5 µm

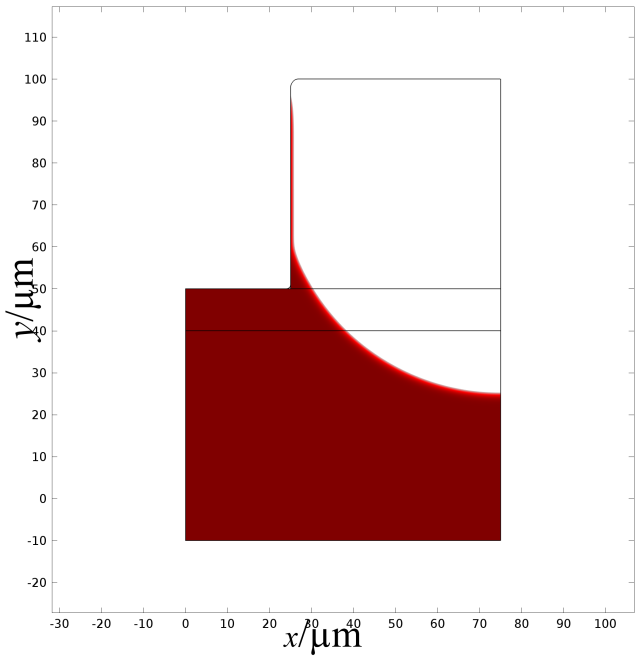

(b) Corner radius= 2 µm

Figure 6.15: Free surface at the end of the simulation for different corner radii.

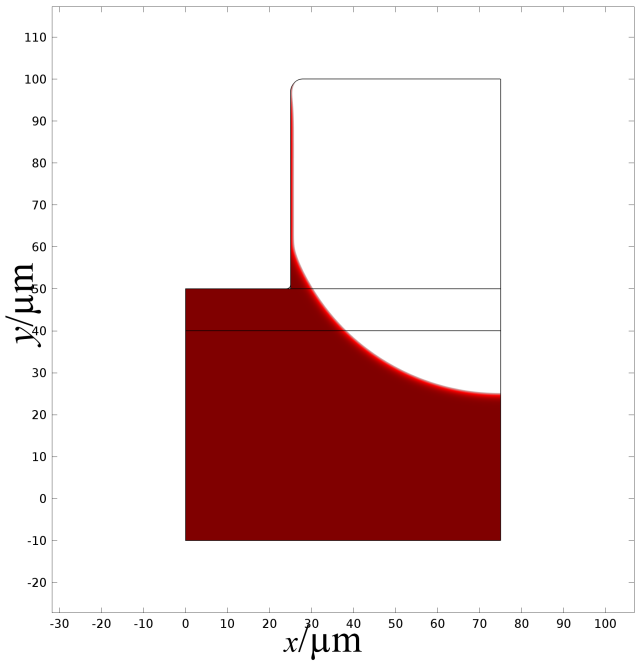

(a) Corner radius= 3 µm

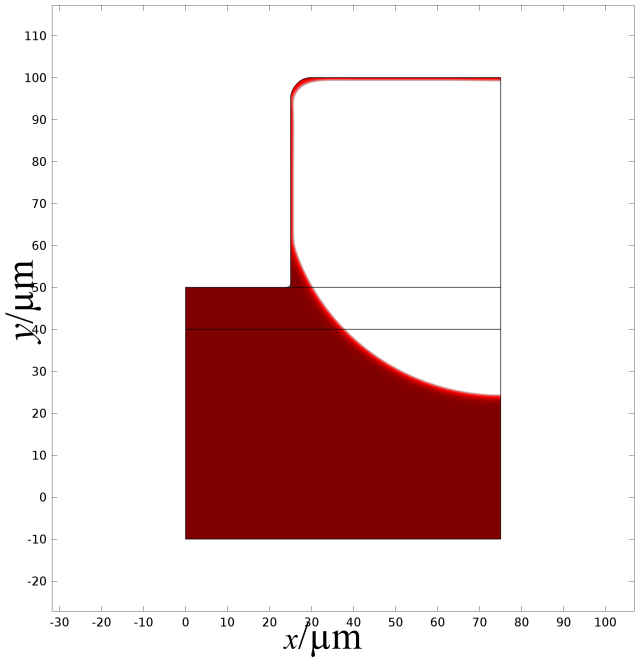

(b) Corner radius= 5 µm

Figure 6.16: Free surface at the end of the simulation for different corner radii.

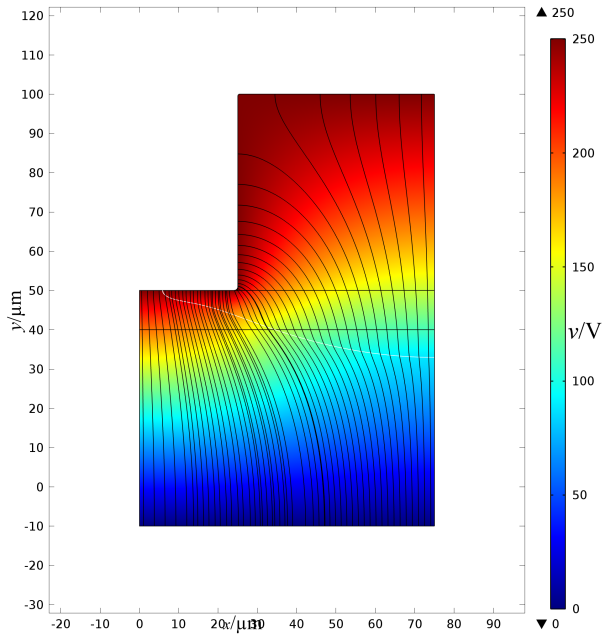

(a) Corner radius = 0.5 µm

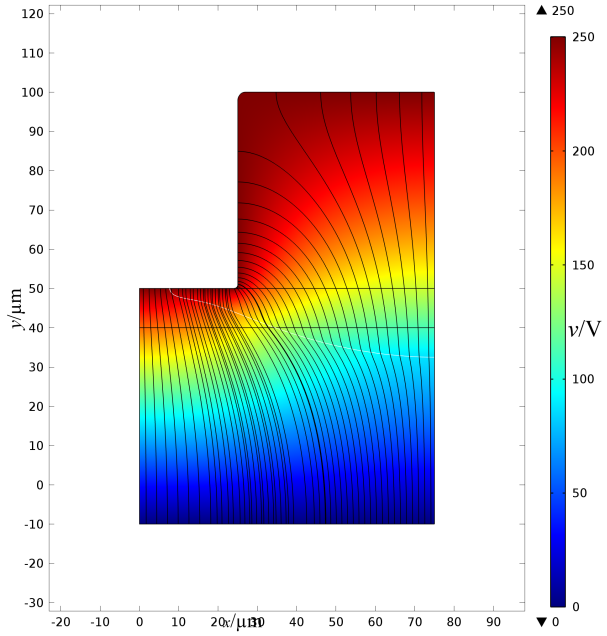

(b) Corner radius = 2 µm

Figure 6.17: Electric fields at the point where the polymer touches the mask for different corner radii.

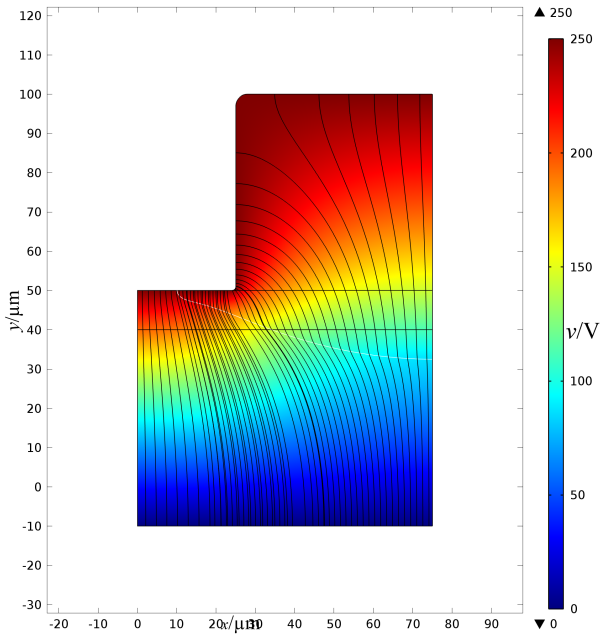

(a) Corner radius = 3 µm

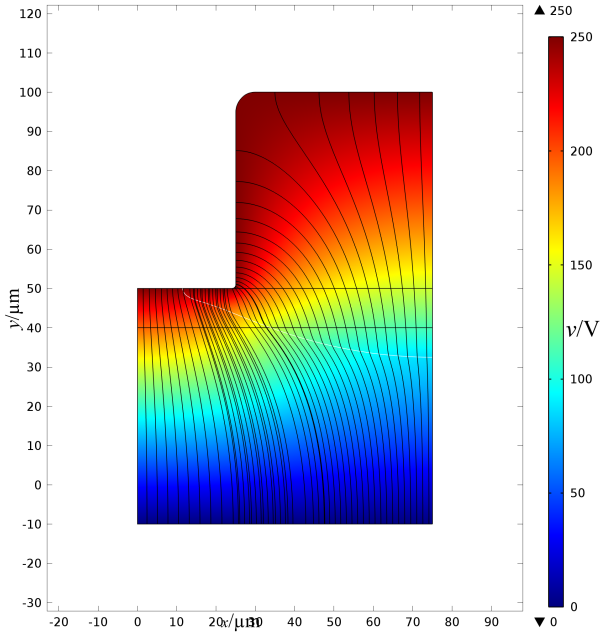

(b) Corner radius = 5 µm

Figure 6.18: Electric fields at the point where the polymer touches the mask for different corner radii.

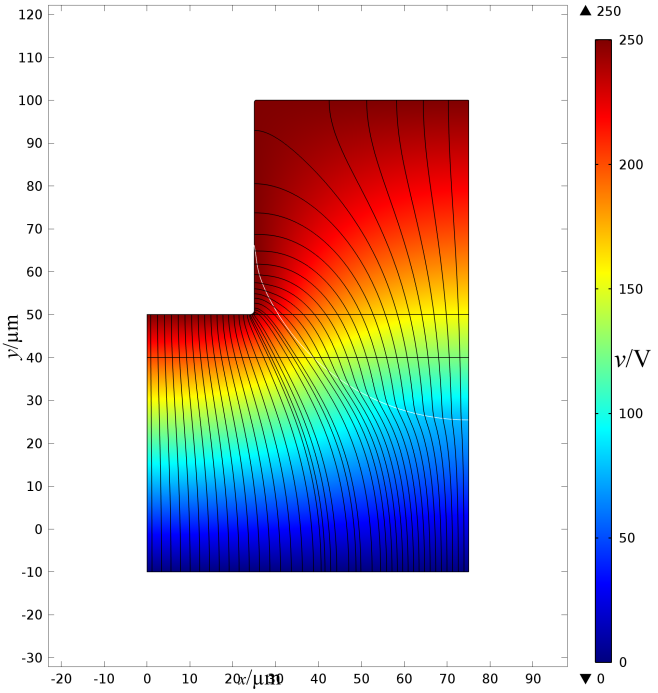

(a) Corner radius = 0.5 µm

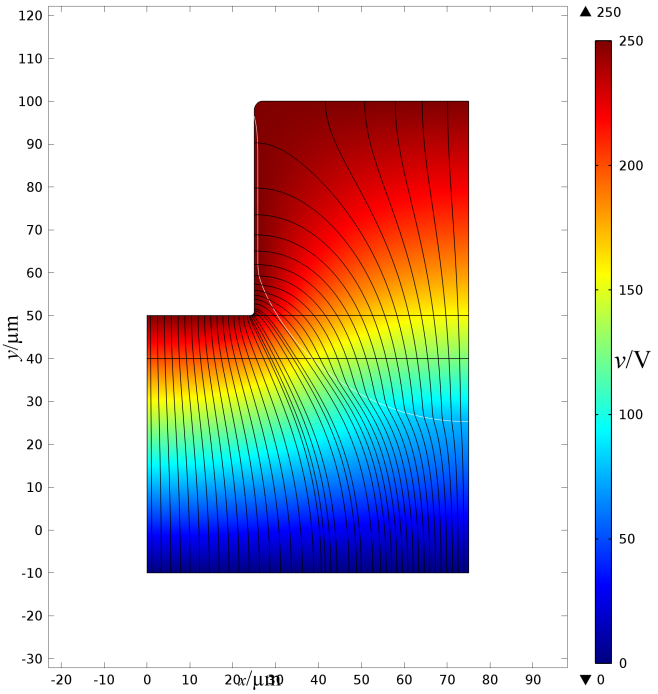

(b) Corner radius = 2 µm

Figure 6.19: Electric fields at the end of the simulation for different corner radii.

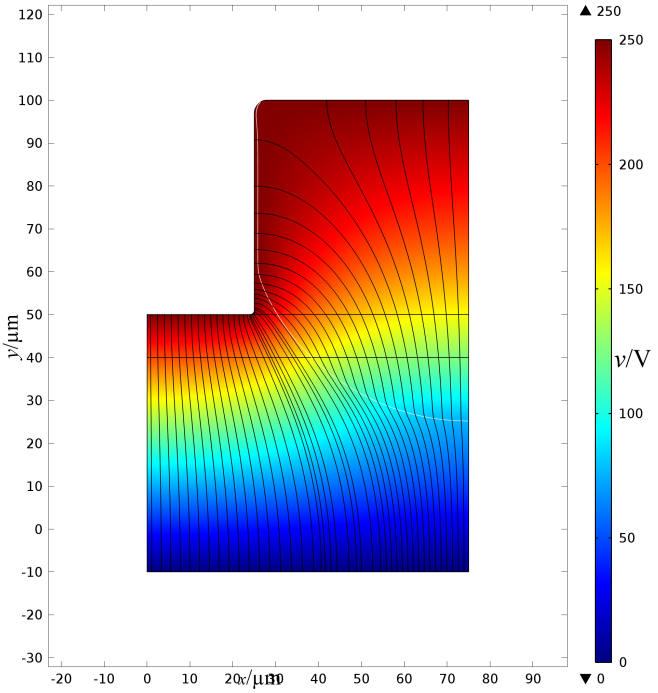

(a) Corner radius = 3 µm

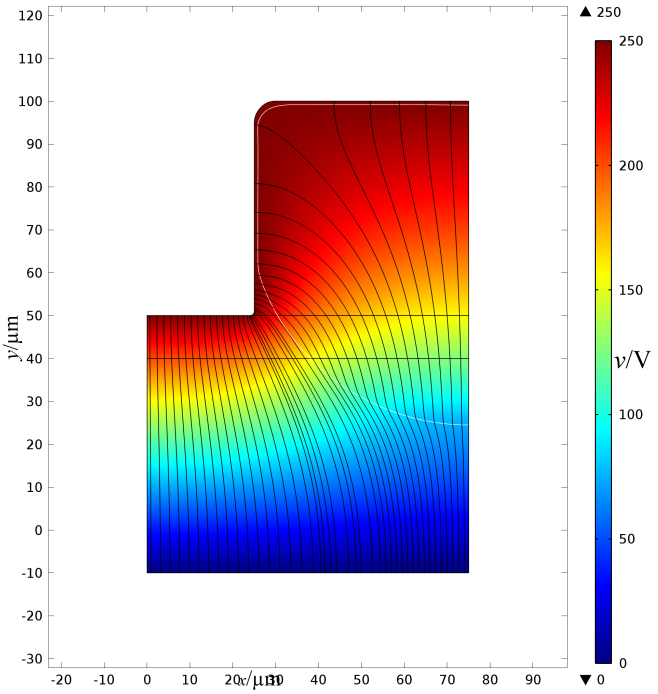

(b) Corner radius = 5 µm

Figure 6.20: Electric fields at the end of the simulation for different corner radii.

6.7 Voltage

Another controllable variable was the voltage of the top electrode mask. Increasing the voltage increases the electric field in the same proportion. This has the effect of changing the dielectric forces. As the dielectric forces are proportional to the electric field squared a small increase in the voltage results in a large change in the dielectric forces. For larger voltages there is a much larger dielectric force at the interface of the polymer and the air.

The results from changing the voltage can be seen in figures (6.21),(6.22), (6.23) and (6.23). The first set of results show the polymer as it first touches the top mask, with the exception of the 100V case, which does not have enough dielectric force to overcome the surface tension and so it only moves by a small amount. The times for the 250V, 500V and 1000V cases here are 0.031s 0.00325s and 0.0008s respectively. This large increase in speed is due to the increase in the dielectric forces caused by the increase in the electric field.

A combined figure showing the surface at the end of the simulation for all 4 voltages is shown in figure (6.25). The figure shows the increased voltage has an effect on the final shape. Most notable is the small bubble in the left corner which appears on the 500V and 1000V cases but not on the 250V case. This is due to the difference of the polymer growing at the start of the simulation so that when it meets the top mask it leaves a bubble in that corner.

The voltage and electric field distributions for these cases can be seen in figures (6.26), (6.27), (6.28) and (6.29). The basic distribution of the electric field is the same, with the usual deflections to the field at the polymer-air interface. However the increased electric field causes the polymer to form a different pattern.

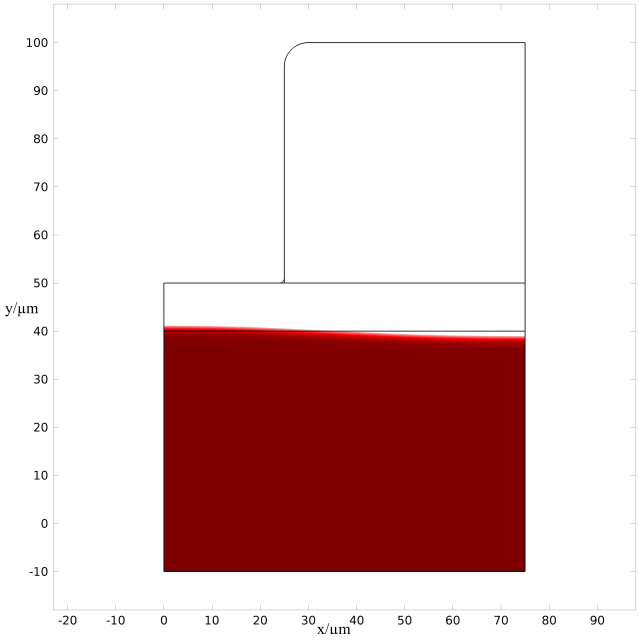

(a) Voltage = 100V

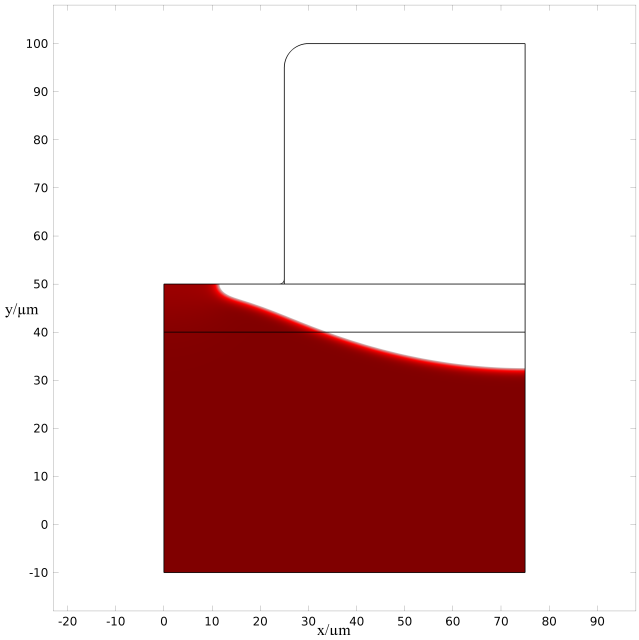

(b) Voltage = 250V

Figure 6.21: Free surface at the point where the polymer touches the mask for different voltages.

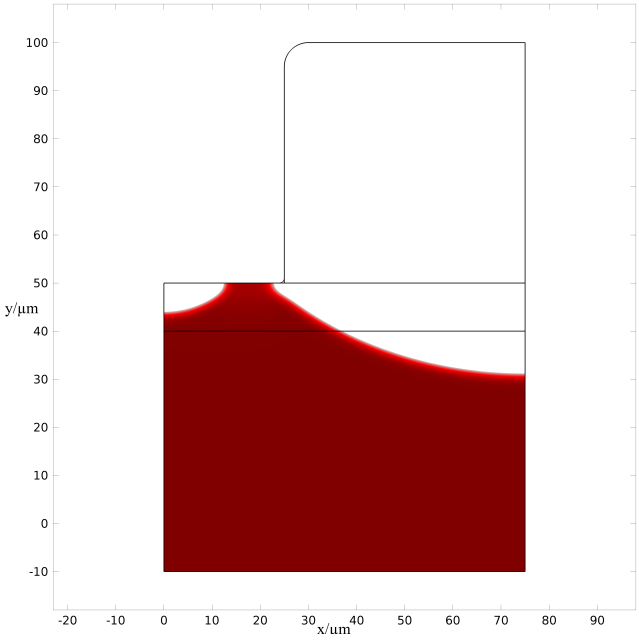

(a) Voltage = 500V

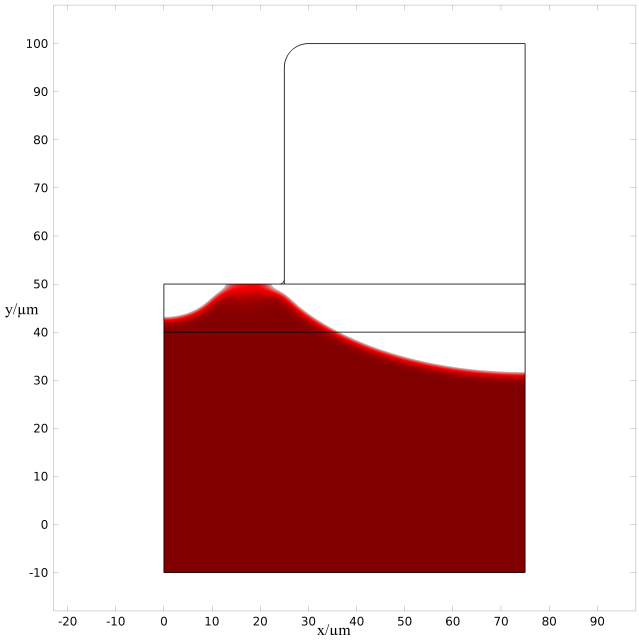

(b) Voltage = 1000V

Figure 6.22: Free surface at the point where the polymer touches the mask for different voltages.

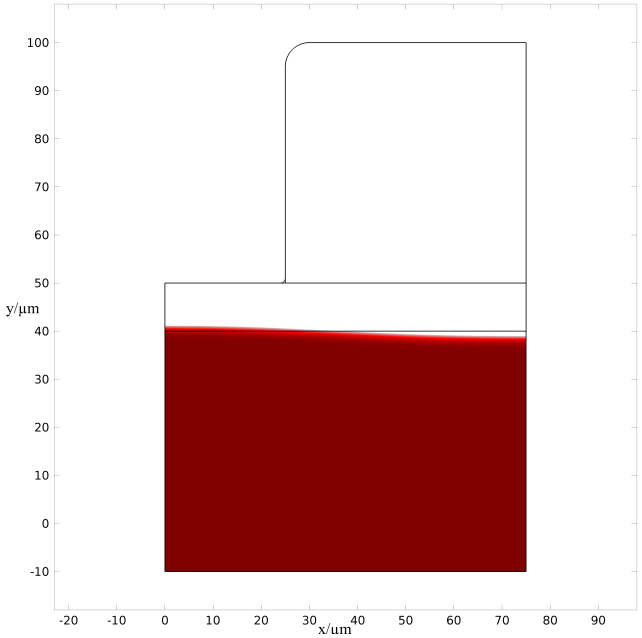

(a) Voltage = 100V

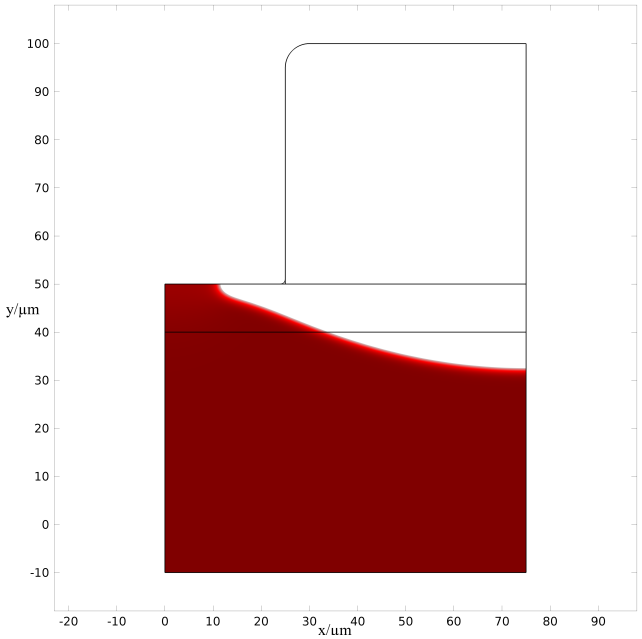

(b) Voltage = 250V

Figure 6.23: Free surface at the end of the simulation for different voltages.

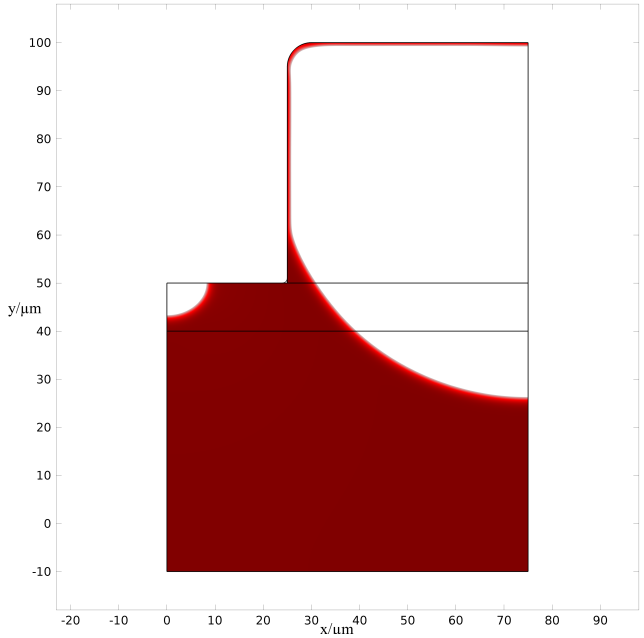

(a) Voltage = 500V

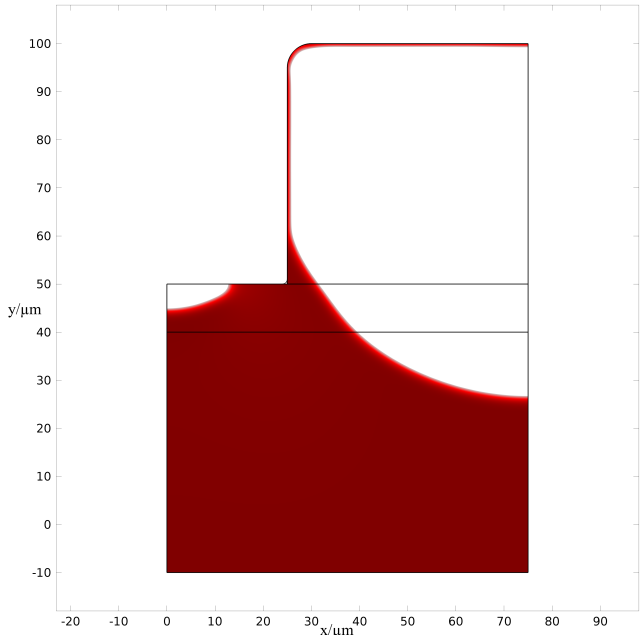

(b) Voltage = 1000V

Figure 6.24: Free surface at the end of the simulation for different voltages.

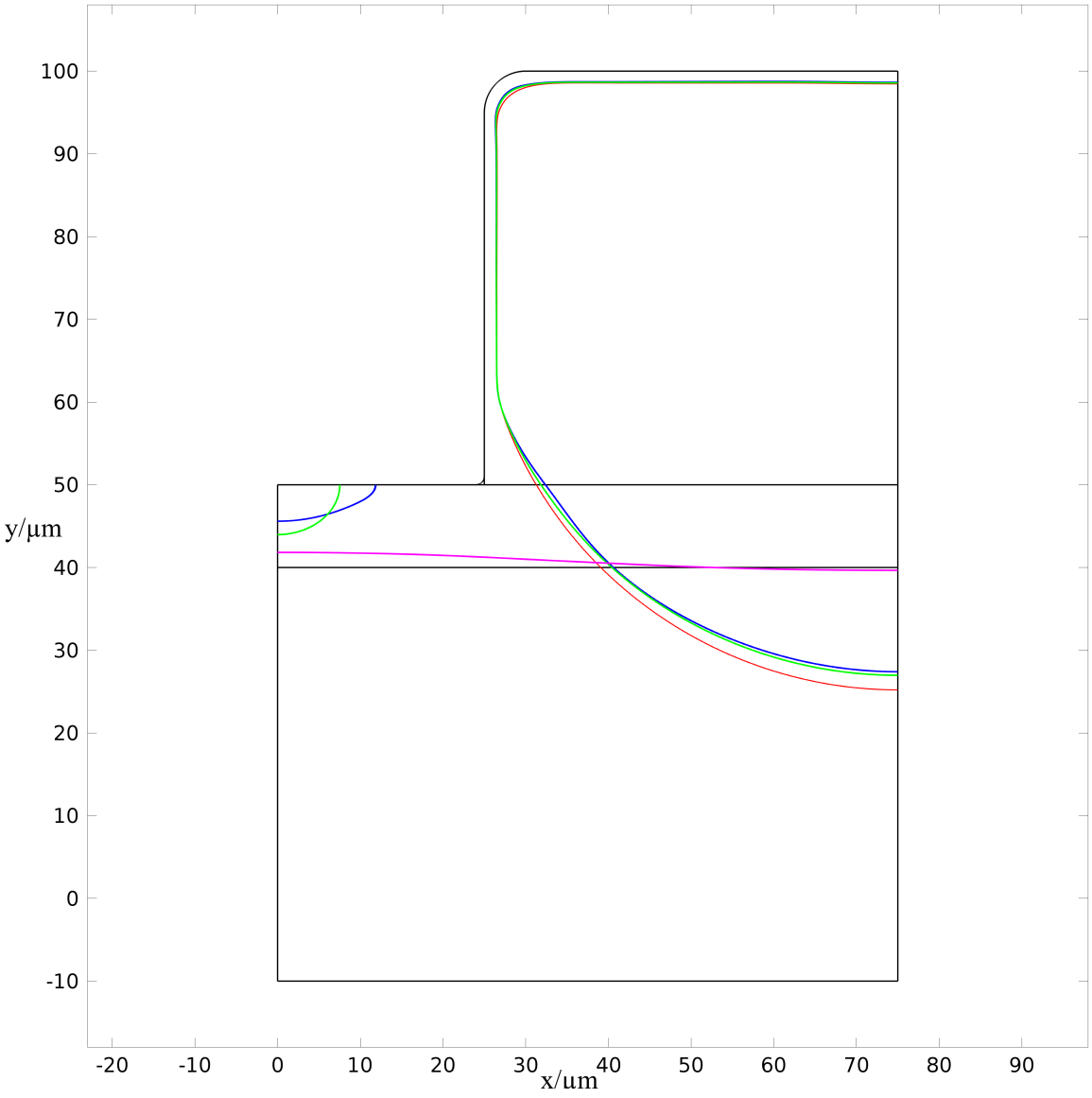

Figure 6.25: Free surfaces at the end of the simulation for voltages of 100V (Magenta), 250V (Red), 500V(Green) and 1000VBlue.

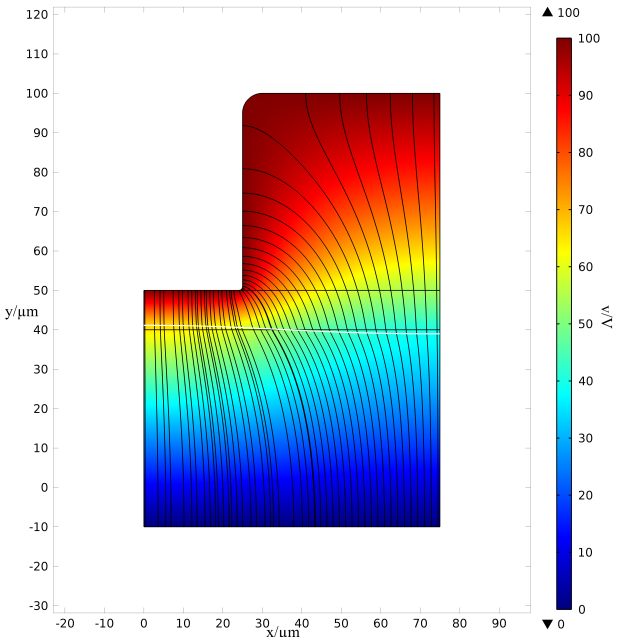

(a) Voltage = 100V

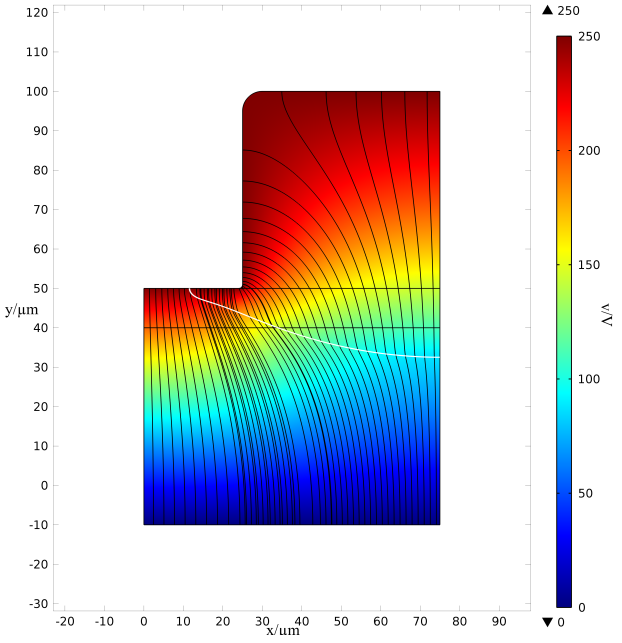

(b) Voltage = 250V

Figure 6.26: Electric field at the point where the polymer touches the mask for different voltages.

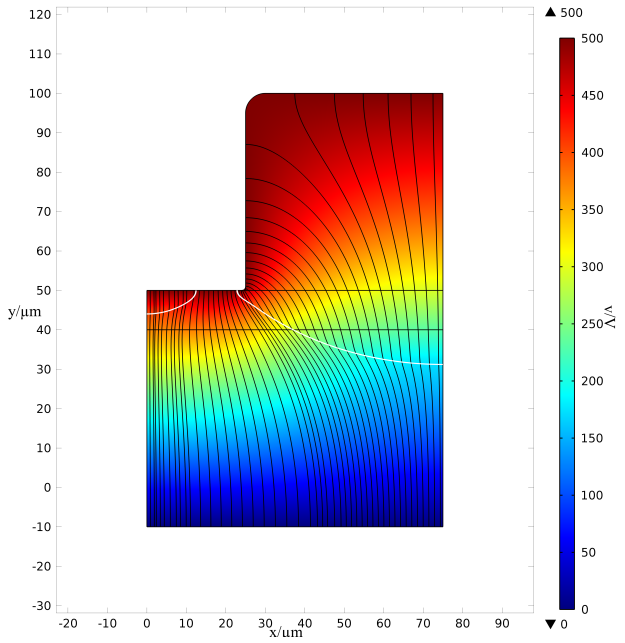

(a) Voltage = 500V

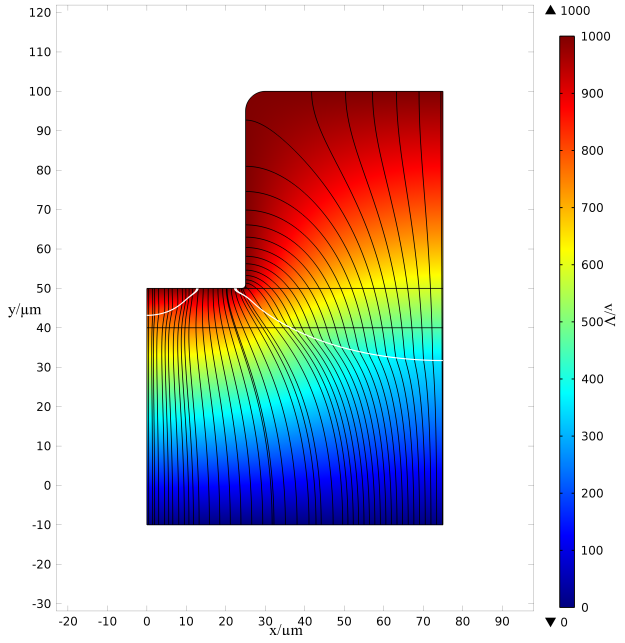

(b) Voltage = 1000V

Figure 6.27: Electric field at the point where the polymer touches the mask for different voltages.

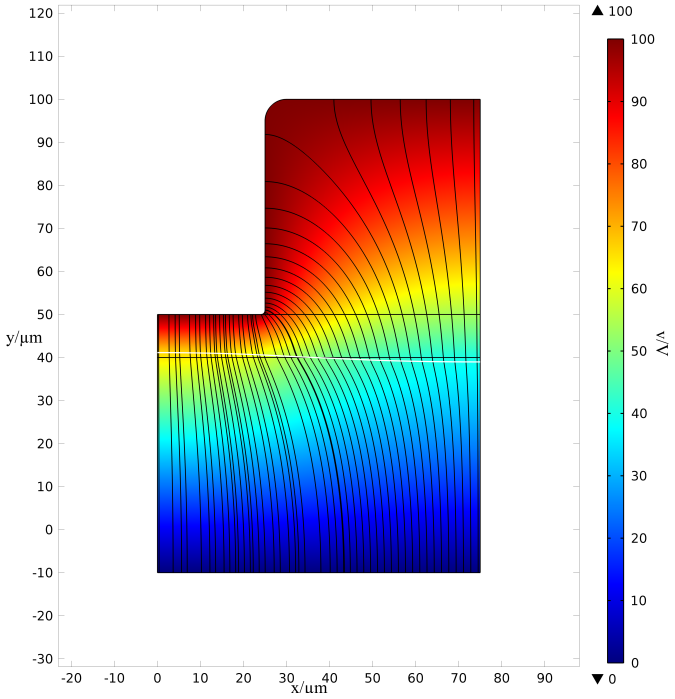

(a) Voltage = 100V

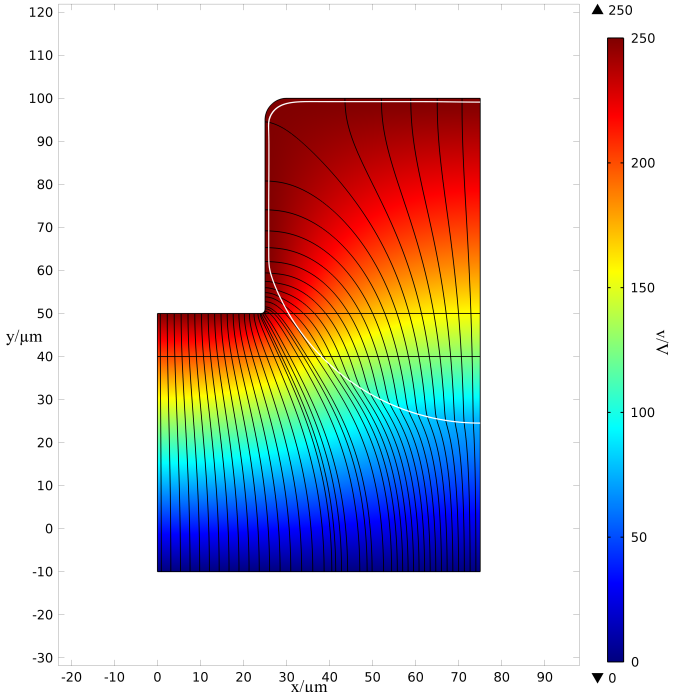

(b) Voltage = 250V

Figure 6.28: Electric field at the end of the simulation for different voltages.

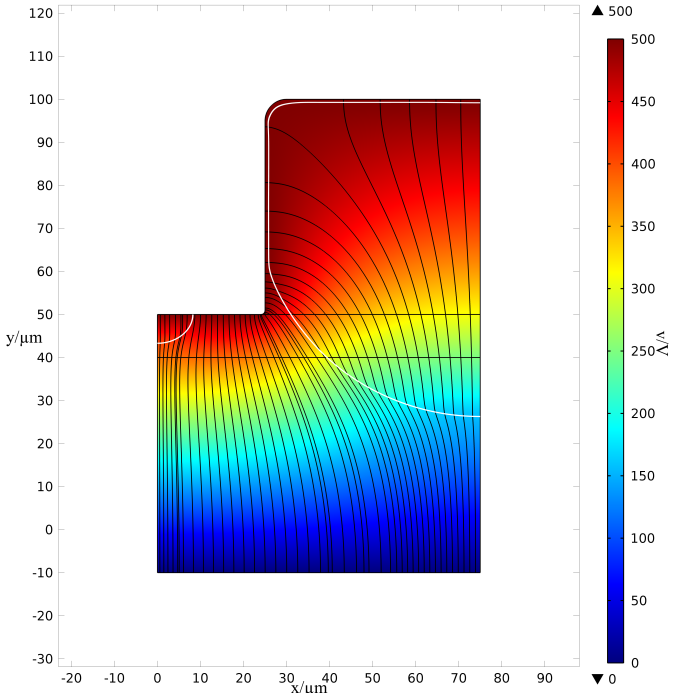

(a) Voltage = 500V

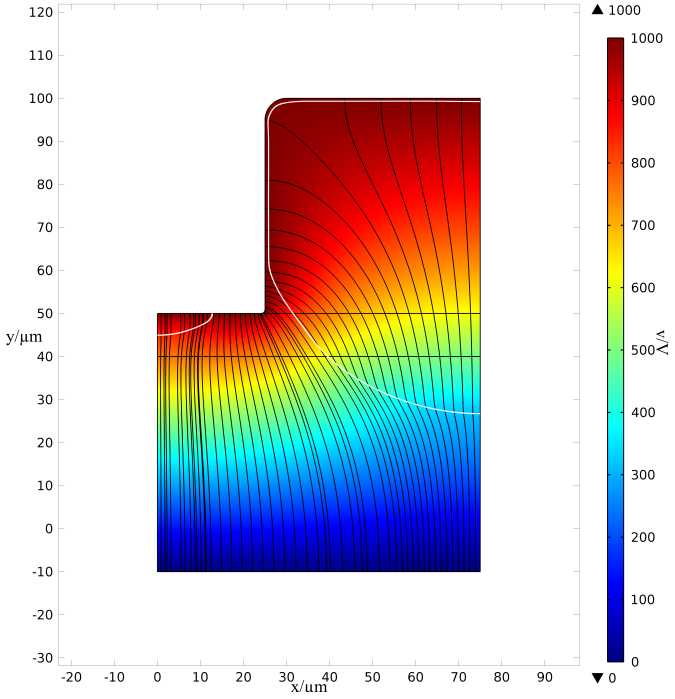

(b) Voltage = 1000V

Figure 6.29: Electric field at the end of the simulation for different voltages.

6.8 Summary

This chapter has demonstrated the effect of changing various material properties of the polymer along with the geometries of the problem and also the voltage. All these quantities have effected the final shape, however changing the original problem geometry either by changing the mask shape, changing the separation of the top mask and the polymer or changing the initial polymer thickness seem to have the greatest effect on the final shape obtained. Altering the permittivity of the polymer and the potential difference applied across the polymers appears to have the greatest effect on the speed of the process, though this would need to be studied in greater detail as changing these properties also has an effect on the final shape of the polymer.

Chapter 7

CONCLUSIONS AND FUTURE WORK

7.1 Conclusions

The work presented here meets the aim and objectives as set out in the introduction to this thesis. The aim of the project being to develop models for the EHDIP and EFAC techniques to assist in the usage of these techniques in the fabrication of polymer microstructures. To achieve this aim 4 objectives were defined:

1. Perform a thorough literature review of the two processes and from this literature review gain an understanding of the state of the art and to develop the theory behind the processes.

2. Develop computational models of the EHDIP process based on the theory developed in the first objective and to validate this model where possible.

3. Develop further computational models of the EFAC process incorporating the

contact angles on the top surface and to validate this model where possible.

4. Use the computational models to perform sensitivity analysis on the EFAC process to observe how altering different variables effect the process.

To achieve objective one an initial literature review was carried out and it was found most work on the topic had been performed on polymers and a nano-scale and not as this work considers on a micro-scale. The theory of how the process works on a micro-scale had to be so further developed, to this end the work of Landau and Lifshitz [94] was used. The equation derived in their book was then re-derived for SI units and used to describe the dielectric forces at the interface between the air and the polymer. The effects of the surface tension and capillary forces were also considered and discussed. The viscoelastic nature of polymer melts was discussed, and it was decided that these would have little effect on the final shape of the polymer. Consequently they were discounted in the models developed. However scope was left for them to be incorporated later.

For objectives two and three computational models of both processes were developed. Early work in developing the model focused on the use and further development of PHYSICA version 3g, a multiphysics simulation package originally developed at the University of Greenwich. However the level set free surface technique in the package proved to be unstable at small scales due to the calculation of the curvature. Consequently a commercial package, COMSOL Multiphysics, was used to perform the simulation work. This was because it includes a diffuse interface phase field freesurface technique that was specifically developed to be stable at small scales. This package was used for the remainder of the project. These models give a good agreement with the limited experimental data available, however no quantitative analysis was able to

be performed due to the limited nature of the experimental data available.

For objective four simulation work was done investigating the effects of changing the shape of the mask used to produce the polymer microstructures. This was because the mask shape was considered to be the simplest way of changing the shape of the polymer obtained. However in addition further cases were considered looking at the effect of changing material properties and other controllable parameters. These results show that the greatest effect on the final shapes obtained from the EFAC process is from changing the masks shape. This was to be expected as the top shell produced from the EFAC process always follows the top mask. The lower shape can be altered by changing the initial polymer thickness and the initial air gap. In addition altering the voltage of the top mask and the permittivity of the polymer has been shown to have an effect on the final shape obtained.

The key outputs of the work presented is the results of the simulations. It was shown that a varied array of shapes can be produced by altering the initial masks and that this mask shape has the greatest effect on the polymer microstructures formed. An extension of the process where both the top and bottom electrodes are shaped has been shown to work in the numerical model. Changing the permittivity has also been shown to have an effect on the shapes formed, though the effect is minimal, however the permittivity does have an effect on the speed of the process. It was demonstrated that the contact angle of the top mask has an effect on the thickness of the polymer at the top of the structures. The size of the air gap and the initial polymer thickness both have an effect on the final shapes of the structures formed. Also using a wetted surface on the bottom mask allows for the production of structures with a flat bottom. It was indicated that for angled masks for the EFAC process sharp corners are not suitable and instead rounded corners must be used. Finally it was shown that the

voltage would need to be controlled in order to ensure that there are no bubbles left at the top of the polymer as with a too high voltage this is the case.

7.2 Further Work

7.2.1 Model Development

The model presented here is an accurate model of both these processes, it currently considers two aspects of the physics of the situation the fluid dynamics and the electrostatics. However though these are considered to be the dominant forces involved the process in reality involves more complex physics. Further work confirming that these have little effect on the process would be beneficial.

The complex rheologies due to the viscoelastic nature of the polymer melt have not been considered in the model presented here. As discussed previously this should not have much of an effect on the final shapes obtained. However it will have an effect on the time taken to form the microstructures. This explains the reason for the disparity between the time-scales of this model and the time-scales of the experiments. The time-scales have not currently been observed experimentally but they are thought to be longer than the models suggest. They are not known as there are currently no experiments which observe the process *in situ*. This is because the curing has to be complete before the structures can be observed. The reason for this is that if the polymer is still molten before this the removal of the mask the polymer would not stay in its new form. This would cause the new structures to be destroyed.

The curing of the polymer also likely plays an important part in the time-scales. It will possibly also affect the reliability of the process. In order for the structures

to be permanent the polymer needs to solidify. For the majority of the experimental work temperature curable polymers have been used. This would mean that variations in temperature may start to cure the polymers in certain regions thus changing the rheology of the polymer. This would have an affect on both the reliability and the speed of the process.

The expansion of the model into three-dimensions would also be a worthwhile endeavour. However this would probably need to be done using a different multiphysics solver than COMSOL. Alternatively HPC systems could be used to massively parallelise the problem. The reason that a 3D model was not attempted during the work presented here was simulation time. The current model takes approximately 1 Day to run for the 2D model on a 16 core workstation. Expanding into three-dimensions would involve at least 50 times the number of cells which would increase the CPU time by a similar amount. So the current model in three-dimensions would take at least 50 days to solve on an equivalent PC. With sufficient CPU power the model would be expandable into three dimensions without much additional work as all the formulations have been derived for three dimensional cases.

7.2.2 Experimental Investigations

In addition to these recommended further developments to the model it would be advantageous for further experimental work to be undertaken. Most relevant to the work presented here would be experimental data that could be used to validate the model fully. This could be achieved by performing some experiments for the same geometry as presented here and measuring accurately the microchannels produced.

If these processes are to be used as a fabrication technique further experimental

work is required looking at process sensitivity. The initial model results presented here suggest some avenues for experimental investigations. The model results suggest that the most important of these is the mask shape. Also of interest is the contact angle of the top mask, as well as the voltage applied.

Additional experimental studies looking at using shaped top and bottom masks would also be advantageous as these have only been shown to work theoretically. Experimental work could show whether or not they will work physically.

7.2.3 Process Applications

Providing the processes are developed to the stage that they can be used for a fabrication technique a wide range of applications for the processes are possible. The EHDIP process has the potential to be used for fabricating microchannels for microfluidic devices. As it is a non-contact process the channels produced are generally smoother than etching techniques which would be advantageous. With further investigation using two shaped masks with EHDIP process could prove to be a useful new method for producing micro-lenses for LED arrays for use in lighting.

The EFAC process would potentially have a wider range of applications. Like EHDIP the process could be used to fabricate microchannels for microfluidic devices. Any channels produced could also be used as wave-guides for communication system fibre-optics. Micro-capsules would be producible using EFAC. Microcapsules have a wide range of uses, their primary uses would be for drug delivery. Microcapsules fabricated from partially permeable polymers can be implanted into the body. Insulin producing cells placed in such microcapsules could be used to produce a bio-artificial pancreas. The partially permeable plastic could keep out white blood cells while letting

the insulin and sugar molecules through thus avoiding rejection.

REFERENCES

[1] H.Kim and S.Bankoff. **The Effect of an Electrostatic field on film flow down and inclined plane**. *Phys. Fluids A*, **4**:2117–2130, 1992.

[2] S. Y.Chou and L.Zhuang. **Lithographically induced self-assembly of periodic polymer micropillar arrays**. *Papers from the 43rd international conference on electron, ion, and photon beam technology and nanofabrication*, **17**(6):3197–3202, 1999.

[3] S. Y.Chou, L.Zhuang, and L.Guo. **Lithographically induced self-construction of polymer microstructures for resistless patterning**. *Applied Physics Letters*, **75**(7):1004–1006, 1999.

[4] E.Schäffer, T.Thurn-Albrect, T. P.Russell, and U.Steiner. **Electrically induced structure formation and pattern transfer**. *Nature*, **403**:874–877, 2000.

[5] P.Deshpande, X.Sun, and S. Y.Chou. **Observation of dynamic behavior of lithographically induced self-assembly of supramolecular periodic pillar arrays in a homopolymer film**. *Applied Physics Letters*, **79**(11):1688–1690, 2001.

[6] P.Deshpande and S. Y.Chou. **Lithographically induced self-assembly of microstructures with a liquid-filled gap between the mask and polymer surface**. In *The 45th international conference on electron, ion, and photon beam technology and nanofabrication*, **19**, pages 2741–2744. AVS, 2001.

[7] P.Deshpande, L. F.Pease, III, L.Chen, S. Y.Chou, and W. B.Russel. **Cylindrically symmetric electrohydrodynamic patterning**. *Phys. Rev. E*, **70**(4):041601, Oct 2004.

[8] Z.Lin, T.Kerle, S. M.Baker, D. A.Hoagland, E.Schäffer, U.Steiner, and T. P.Russell. **Electric field induced instabilities at liquid/liquid interfaces**. *Journal of Chemical Physics*, **114**(5):2377–2381, 2001.

[9] Z.Lin, T.Kerle, T. P.Russell, E.Schäffer, and U.Steiner. **Structure Formation at the Interface of Liquid/Liquid Bilayer in Electric Field**. *Macromolecules*, **35**:3971–3976, 2002.

[10] Z.Lin, T.Kerle, T. P.Russell, E.Schäffer, and U.Steiner. **Electric Field Induced Dewetting at Polymer/Polymer Interfaces**. *Macromolecules*, **35**:6255–6262, 2002.

[11] D.Selac, W.Lu, C.Wang, and A.Sastry. **Pattern Formation in a polymer thin film induced by an in-plane electric field**. *Applied Physics Letters*, **85**:1161–1163, 2004.

[12] M.Yang, C. S.Ozkan, and H.Gao. **Electric Field Induced Self Assembly of Polymer Structures**. *Nanotech*, **3**, 2003.

[13] T. Y.Hin, C.Liu, P. P.Conway, W.Yu, S.Cargill, and M. P.Desmulliez. **A Polymeric Optical Waveguide-on-flex Fabrication Using Electrostatic-induced Lithography**. *Photonics Technology Letters*, **22**:957–959, 2010.

[14] P.Pattader, I.Banerjee, A.Sharma, and D.Bandyopadhyay. **Multiscale pattern generation in viscoelastic polymer fiulms by spatiotemporal modulation of electric field and control of rheology**. *Adv. Funct. Matter.*, **21**:324–335, 2011.

[15] E.Tiand, T.Svobodny, and J.Philips. **Thin liquid film morphology driven by electro-static field**. *Appl. Math. Mech.*, **32**:1039–1046, 2011.

[16] M.El-Sayed, M.Moussa, A.Hassan, and N.Hafez. **Electrohydrodynamic instability of two thin viscous leaky dielectric fluid films in a porous medium**. *Appl. Math.*, **2011**:498718, 2011.

[17] M.Trau, S.Sankaran, D. A.Saville, and I. A.Aksay. **Electric-field-induced pattern formation inc olloidal dispersions**. *Nature*, **374**:437–439, 1995.

[18] L.Chen, L.Zhuang, P.Deshpande, and S.Chou. **Novel Polymer Patterns Formed by Lithographically Induced Self-Assembly (LISA)**. *Langmuir*, **21**(3):818–821, 2005.

[19] N. E.Voicu, S.Harema, and U.Steiner. **Electric-Field-Induced Pattern Morphologies in Thin Liquid Films**. *Advanced Functional Materials*, **16**:926–934, 2006.

[20] M. D.Dickey, E.Collister, A.Raines, P.Tsiartas, T.Holcombe, S. V.Sreenivasan, R. T.Bonnecaze, and C. G.Willson. **Photocurable Pillar Arrays Formed via Electrohydrodynamic Instabilities**. *Chemistry of Materials*, **18**(8):2043–2049, 2006.

[21] G. I.Taylor and A. D.McEwan. **The stability of a horizontal fluid interface in a vertical electric field**. *Journal of Fluid Mechanics*, **22**:1–15, 1965.

[22] B.Uma and R.Usha. **A thin conducting viscous film on an inclinerd plane in the presence of a uniform normal electric field: bifurcation scenarios**. *Phys. Fluids*, **20**:032102, 2008.

[23] D.Tseluiko, M. B. adn D.T Papageorgiou, and J.-M.Vanden-Broeck. **Electrified viscous thin film over topography**. *Phys. Fluids*, **20**:042103, 2008.

[24] D.Tseluiko, M. B. adn D.T Papageorgiou, and J.-M.Vanden-Broeck. **Electrified viscous thin film over topography**. *J. Fluid Mech*, **597**:449–475, 2008.

[25] J.Peng, Y.Han, Y.Yang, and B.Li. **Pattern formation in polymer films under the mask**. *Polymer*, **44**:2379–2384, 2003.

[26] M. D.Morariu, N. E.Voicu, E.Schäffer, Z.Lin, T. P.Russell, and U.Steiner. **Hierarchical structure formation and pattern replication induced by an electric field**. *Nature Materials*, **2**:48–52, 2003.

[27] P.Goldberg-Oppenheimer and U.Steiner. **Rapid Electrohydrodynamic Lithography Using Low Viscosity Polymers**. *Small*, **6**:1248–1254, 2010.

[28] K. A.Leach, S.Gupta, M. D.Dickey, C. G.Willson, and T. P.Russell. **Electric field and dewetting induced hierarchical structure formation in polymer/polymer/air trilayers**. *Chaos*, **15**:047506, 2005.

[29] K. A.Leach, Z.Lin, and T. P.Russell. **Early Stages in the Growth of Electric Field-Induced Surface Fluctuations**. *Macromolecules*, **38**:4868–4873, 2005.

[30] S. Y.Chou. **Theme Article - Nanoimprint Lithography and Lithographically Induced Self-Assembly**. *MRS Bulletin*, **26**:514–517, 2001.

[31] S.Srivastava, R.Sankar, C.Wang, and D.Bandyopadhyay. **Electric Field induced microstructres in thin films of physiochemcially heterogeneous and patterned substrates**. *J. Chem Phys.*, **132**:174703, 2010.

[32] H.Li, W.Yu, L.Zhang, Z.Liu, K. E.Brown, E.Abraham, S.Cargill, C.Tonry, M. K.Patel, C.Bailey, and M. P. Y.Desmulliez. **Simulation and modelling of sub-30 nm polymeric channels fabricated by electrostatic induced lithography**. *RSC Adv.*, **3**:11839–11845, 2013.

[33] C.Liu and J.Shen. **A phase field model for the mixture of two incompressible fluids and its approximation by a Fourier-specrtral method**. *Physica D.*, **179**:211–228, 2003.

[34] V.Gill, P.Guduru, and B.Sheldon. **Electric field induced surface diffusion and micro/nano-scale island growth**. *International Journal of Solids and Structures*, **45**:943–958, 2008.

[35] C.Brown, G.Wells, M.Newton, and G.McHale. **Voltage-programable liquid optical interface**. *Nature Photonics*, **3**:403–405, 2009.

[36] S. F.Lyuksyutov, R. A.Vaia, P. B.Paramov, S.Juhl, L.Waterhouse, R. M.Ralich, G.Sigalov, and E.Sancaktar. **Electrostatic nanolithography in polymers using atomic force microscopy**. *Nature Materials*, **2**:468–472, 2003.

[37] X. N.Xie, H. J.Chung, D.Bandyopadhay, A.Sharma, C. H.Sow, A. A.Bettiol, and A. T. S.Wee. **Two Coexisting Modes in Field-Assisted AFM Nano-patterning of Thin Polymer Films**. *Macromoleclular Chemistry and Physics*, **209**:1358–1366, 2008.

[38] C. M.Bruinink, M.Péter, P. A.Maury, M.De Boer, L.Kuipers, J.Huskens, and D. N.Reinhoudt. **Capillary force lithography: fabrication of functional polymer templates as versatile tools for nanolithography**. *Advanced Functional Materials*, **16**(12):1555–1565, 2006.

[39] J.Choi, K.-H.Lee, and S.Yang. **Fabrication of PDMS through-holes using the MIMIC method and the surface treatment by atmospheric-pressure CH4/He RF plasma**. *Journal of Micromechanics and Microengineering*, **21**(9):097001, 2011.

[40] K. Y.Suh, Y. S.Kim, and H. H.Lee. **Capillary force lithography**. *Advanced Materials*, **13**(18):1386, 2001.

[41] K. Y.Suh and H. H.Lee. **Capillary force lithography: large-area patterning, self-organization, and anisotropic dewetting**. *Advanced Functional Materials*, **12**(6-7):405–413, 2002.

[42] H.Chen, W.Yu, S.Cargill, M.Patel, C.Bailey, C.Tonry, and M.Desmulliez. **Self-encapsulated hollow microstructures formed by electric field-assisted capillarity**. *Microfluidics and Nanofluidics*, **13**(1):75–82, 2012.

[43] C.Tonry, M.K Patel, C.Bailey, M.PY Desmuliez, S.Cargill, and W.Yu. **A Method for the Micro-encapsulation of Dielectric Fluids in Joined Polymer Shells**. *Current Organic Chemistry*, **17**(1):65–71, 2013.

[44] Z.Sou and J.Liang. **Theory of lithographically-induced self-assembly**. *Applied Physics Letters*, **78**(25):3971–3973, 2001.

[45] G.Tomar, V.Shankar, A.Sharma, and G.Biswas. **Electrohydrodynamic instability of a confined viscoelastic liquid film**. *Journal of Non-Newtonian Fluid Mechanics*, **143**:120–130, 2007.

[46] V.Shankar and A.Sharma. **Instability of the interface between thin fluid films subjected to electric fields**. *Journal of Colloid and Interface Science*, **274**:294–308, 2004.

[47] L. F.Pease, III and W. B.Russel. **Linear stability analysis of thin leaky dielectric films subjected to electric fields**. *Journal of Non-Newtonian Fluid Mechanics*, **102**:233–250, 2002.

[48] L. F.Pease, III and W.Russel. **Electrostatically induced submicron patterning of thin perfect and leaky dielectric films: a generalised linear stability analysis**. *J. Chem. Phys*, **118**:3790–3803, 2003.

[49] L. F.Pease, III and W.Russel. **Limitations on length scales for electrostatically induced micrometer pillars and holes**. *Langmuir*, **20**:795–804, 2004.

[50] D.Koulova-Nenova. **EHD instability of two liquid layer system with deformable interface**. *Journal of Electrostatics*, **40-41**:185 – 190, 1997. Proceedings of the 8th International Conference on Electrostatics.

[51] T. P.Russell, Z.Lin, E.Schäffer, and U.Steiner. **Aspects of Electrohydrodynamic Instabilities at Polymer Interfaces**. *Fibers and Polymers*, **4**(1):1–7, 2003.

[52] L.Wu and S. Y.Chou. **Electrohydrodynamic instability of a thin film of viscoelastic polymer underneath a lithographically manufactured mask**. *Journal of Non-Newtonian Fluid Mechanics*, **125**:91–99, 2005.

[53] M.Han, J.Lee, S.Park, and Y.Choi. **Molecular dynamics study of thin film instability and nanostructure formation**. *International Journal of Heat and Mass Transfer*, **49**(5-6):879 – 888, 2006.

[54] E.Schäffer, T.Thurn-Albrecht, T. P.Russell, and U.Steiner. **Electrohydrodynamic instabilities in polymer films**. *Europhysics Letters*, **53**(4):518–524, 2001.

[55] E.Schäffer, S.Walheim, and U.Steiner. **Controlling Film Instabilities**. In J.-M.Buchlin and J.Anthoine, editors, *Proceedings of the 4th European Coating Symposium 2001*, pages 33–43, 2002.

[56] A.Onuki. **Interface instability induced by an electric field in fluids**. *Physica A: Statistical and Theoretical Physics*, **217**(1-2):38 – 52, 1995.

[57] N.Wu and W.Russel. **Electrohydrodyanmic instability of dielectric bilayers: kinetics and thermodynamics**. *Ind. Eng. Chem*, **45**:5455–5465, 2006.

[58] L. F.N. Wu andPease, III and W.Russel. **Electric-field-induced patterns in thin polymer films: weakly nonliner and fully nonlinear evolution**. *Langmuir*, **21**:12290–12302, 2005.

[59] N.Wu, L. F.Pease, III, and W. B.Russel. **Toward Large-Scale Alignment of Electrohydrodynamic Patterning of Thin Polymer Films**. *Advanced Functional Materials*, **16**:1992–1999, 2006.

[60] A.Esmaeeli and M.Reddy. **The electrohydrodyunamics of superimposed fluiods subjected to a nonuniform transverse electric field**. *International J. Multiphase Flow*, **37**:1331–1347, 2011.

[61] D.Kim and W.Lu. **Interface instability and nanostructure patterning**. *Computational Materials Science*, **38**:418–425, 2006.

[62] R.Verma, A.Sharma, K.Kargupta, and J.Bhaumik. **Electric Field Induced Instability and Pattern Formation in Thin Liquid Films**. *Langmuir*, **21**:3710–3712, 2005.

[63] R.Verma, A.Sharma, I.Banerjee, and K.Kargupta. **Spinodal instability and pattern formation in thin liquid films confined between two plates**. *Journal of Colloid and Interface Science*, **296**:220–232, 2006.

[64] R.Craster and O.Matar. **Electrically induced pattern formation in thin leaky dielectric films**. *Phys. Fluids*, **17**:032104, 2005.

[65] N.Wu and W. B.Russel. **Micro- and nano-patterns created via electrohydrodynamic instabilities**. *Nano Today*, **4**:180–192, 2009.

[66] B.Bhushan. **Nanotribology and nanomechanics of MEMS/NEMS and BioMEMS/BioNEMS materials and devices**. *Microelectronic Engineering*, **84**:387–412, 2007.

[67] C.Rivet, H.Lee, A.Hirsch, S.Hamilton, and H.Lu. **Microfluidics for medical diagnostics and biosensors**. *Chemical Engineering Science*, **In press**, 2010.

[68] Y.Lim, A.Kouzani, and W.Duan. **Lab-on-a-chip: a component view**. *Microsystem Technology*, **16**:1995–2015, 2010.

[69] R.Bashir. **BioMEMS: state-of-the-art in detection, opportunities and prospects**. *Advanced Drug Delivery Reviews*, **56**:1565–1586, 2004.

[70] J.Melin and S. R.Quake. **Microfluidic large-scale integration: the evolution of design rules for biological automation**. *Annu. Rev. Biophys. Biomol. Struct.*, **36**:213–231, 2007.

[71] T.Thorsen, S. J.Maerkl, and S. R.Quake. **Microfluidic large-scale integration**. *Science*, **298**(5593):580–584, 2002.

[72] M. A.Unger, H.-P.Chou, T.Thorsen, A.Scherer, and S. R.Quake. **Monolithic microfabricated valves and pumps by multilayer soft lithography**. *Science*, **288**(5463):113–116, 2000.

[73] J.Barber, D.Conkey, J.Lee, N.Hubbard, L.Howell, H.Schmidt, and A.Hawkins. **Fabrication of hollow waveguides with sacrificial aluminium cores**. *IEEE Photonics Technology Letters*, **17**:186–190, 2005.

[74] B. A.Peeni, M. L.Lee, A. R.Hawkins, and A. T.Woolley. **Sacrificial layer microfluidic device fabrication methods**. *Electrophoresis*, **27**(24):4888–4895, 2006.

[75] E.Bonaccurso, H.-J.Butt, and K.Graf. **Microarrays by structured substrate swelling**. *European Polymer Journal*, **40**:975–980, 2004.

[76] C.-R.Lin, R.-H.Chen, and C.Hung. **The Characterisation and Finite-Element Analysis of a Polymer under Hot Pressing**. *The International Journal of Advanced Manufacturing Technology*, **20**:230–235, 2002.

[77] C. N.LaFratta, L.Li, and J. T.Fourkas. **Soft-lithographic replication of 3D microstructures with closed loops**. *Proceedings of the National Academy of Sciences*, **103**(23):8589–8594, 2006.

[78] J.Xia, D.Qu, J.Chen, and W.Zhu. **Self assembly of polymer microlens array for integral imaging**. *Displays*, **31**(4-5):186–190, 2010.

[79] S.Jinxia, L.Heng, and H.Pingsheng. **Micro- and nano-patterning of polymers**. *Chinese Science Bulletin*, **49**:1431–1436, 2004.

[80] B.Ziaie, A.Baldi, M.Lei, Y.Gu, and R. A.Siegel. **Hard and soft micromachining for BioMEMS: review of technique and examples of applications in microfluidics and drug delivery**. *Advanced Drug Delivery Reviews*, **56**:145–172, 2004.

[81] X.-M.Zhao, Y.Xia, O. J.Schueller, D.Qin, and G. M.Whitesides. **Fabrication of microstructures using shrinkable polystyrene films**. *Sensors and Actuators A*, **65**:209–217, 1998.

[82] C.Martin, A.Llobera, T. L.chlé, G.Villanueva, A.Voigt, V.Fakhfouri, J.Kim, N.Berthet, J.Bausells, G.Greutzner, L.Nicu, J.Brugger, and F. P.Murano. **Novel methods to pattern polymers for microfluidics**. *Microelectronic Engineering*, **85**:972–975, 2008.

[83] C.Mills, E.Martinez, F.Bessueille, G.Villanueva, J.Baussells, J.Samitier, and A.Errachid. **Production of structures for microfluidics using polymer imprint techniques**. *Microelectronic Engineering*, **78-79**:695–700, 2005.

[84] R.Guijt, E.Baltussen, G. vand der Steen, R. S. andS. Schlautmann, H.Billiet, J.Frank, G. van Dedem, and A. van den Berg. **New approaches for fabrication of microfluidic capillary electrophoresis devices with on-chip conductivity detection**. *Electrophoresis*, **22**:235–241, 2001.

[85] X. W. D.Lou, L. A.Archer, and Z.Yang. **Hollow Micro-/Nanostructures: Synthesis and Applications**. *Advanced Materials*, **20**(21):3987–4019, 2008.

[86] T. M. S.Chang and S.Prakash. **Procedures for microencapsulation of enzymes, cells and genetically engineered microorganisms**. *Molecular Biotechnoilogy*, **17**:249–260, 2001.

[87] R.Hernández, G.Orive, A.Aurua, and J.Pedraz. **Microcapsules and microcarriers for in situ cell delivery**. *Advanced Drug Delivery Reviews*, **62**:711–730, 2010.

[88] K.Sata, K.Yoshida, S.Takahashi, and J.Anzai. **pH. and sugar-sensitive layer-bylayer films and microcapsules for drug delivery**. *Advanced Drug Delivery Reviews*, **63**:809–821, 2011.

[89] Y.Zhu, J.Shi, W.Shen, X.Dong, J.Feng, M.Ruan, and Y.Li. **Stimuli-Responsive Controlled Drug Release from a Hollow Mesoporous Silica Sphere/Polyelectrolyte Multilayer Core–Shell Structure**. *Angewandte Chemie*, **117**(32):5213–5217, 2005.

[90] Y.Cai, H.Pan, X.Xu, Q.Hu, L.Li, and R.Tang. **Ultrasonic controlled morphology transformation of hollow calcium phosphate nanospheres: a smart and biocompatible drug release system**. *Chemistry of materials*, **19**(13):3081–3083, 2007.

[91] V. V.Sokolova, I.Radtke, R.Heumann, and M.Epple. **Effective transfection of cells with multi-shell calcium phosphate-DNA nanoparticles**. *Biomaterials*, **27**(16):3147–3153, 2006.

[92] B.Whol and J.Engbersen. **Responsive layer-by-layer materials for drug delivery**. *Journal of Controlled Release*, **158**:2–14, 2012.

[93] Y.Teramura and H.Iwata. **Bioartificial pancreas microencapsulation and conformal coating of islets opf Langerhans**. *Advanced Drug Delviery Reviews*, **62**:827–840, 2010.

[94] L.Landau and E.Lifshitz. *Electrodynamics of Continuous Media*. Pergamon Press, second edition, 1984.

[95] F. P.Baaijens. **Mixed finite element methods for viscoelastic flow analysis: a review**. *Journal of Non-Newtonian Fluid Mechanics*, **79**(2-3):361 – 385, 1998.

[96] H.Mohamed and B.Reddy. **Some properties of models for generalized Oldroyd-B fluids**. *International Journal of Engineering Science*, **In press**, 2010.

[97] M.Tomé, A.Castelo, V.Ferreira, and S.Mckee. **A finite difference technique for solving Oldroyd-B model for unsteady free surface flows**. *Journal of Non-Newtonian Fluid Mechanics*, **154**:179–206, 2008.

[98] Multi-Physics Software Ltd. *PHYSICA Reference manual*, 2010.

[99] COMSOL Ltd. *COMSOL Multiphysics Manual*, 2011.

[100] S.Osher and R. P.Fedkiw. **Level Set Methods: An Overview and Some Recent Results**. *Journal of Computational Physics*, **169**(2):463 – 502, 2001.

[101] S.Patankar. *Numerical Heat Transfer and Fluid Flow*. CRC Press, 1980.

[102] M.Fagan. *Finite Element Analysis: Theory and Practice*. Prentice Hall, 1992.